2019

Chemistry and Dissipation at Mineral Surfaces in the Space Environment

William Tucker
University of Central Florida

CHEMISTRY AND DISSIPATION AT MINERAL SURFACES IN THE SPACE ENVIRONMENT

by

WILLIAM C. TUCKER
B.S. University of Central Florida, 2002

A dissertation submitted in partial fulfilment of the requirements
for the degree of Doctor of Philosophy
in the Department of Physics
in the College of Sciences
at the University of Central Florida
Orlando, Florida

Spring Term
2019

Major Professor: Patrick K. Schelling

ABSTRACT

The composition and morphology of mineral surfaces is known to play an important role in various phenomena relevant to planetary science. For example, the synthesis and processing of complex organics likely occurs at mineral surfaces strongly affected by the space environment. Furthermore, the dissipative and adhesive properties of dust grains may depend strongly on the chemical state of the surface including the presence of dangling bonds, adsorbates, and radicals. In this dissertation, experimental results are first presented which demonstrate that mineral grains subjected to high temperatures in a reducing environment lead to iron nanoparticles which are strongly catalytic for the formation of complex organic species. Next, results obtained using molecular-dynamics simulations demonstrate that uncoordinated surface atoms in metallic nanoparticles result in plastic deformation, strong dissipation and adhesion during collisions. This can be contrasted with previous simulations which demonstrate significantly weaker dissipation when surface atoms are passivated. Calculations of critical sticking velocities demonstrate that simple coarse- grain models are insufficient for predicting the adhesive behavior of sub-micron sized grains. Next, results are presented describing a computational study illuminating the role of surface chemistry on adhesion and dissipation for iron nanoparticle collisions, which in the case of free radical adsorbates may also contribute to the creation of more complex species. Lastly, to further elucidate dissipation, the direct coupling of harmonic vibrational modes in the dissipation process is established. The results demonstrate broad participation of low and high-frequency modes during a collision during a timescale less than time required for particles to rebound. Hence, our results demonstrate extremely strong likelihood of adhesion during collisions. This approach provides a way to use density-functional theory calculations to directly compute dissipative couplings at mineral interfaces.

I dedicate this dissertation to my beloved wife Emily Tucker for her constant support and encouragement.

ACKNOWLEDGMENTS

First, I would like to thank my advisor and committee chairperson Dr. Patrick K. Schelling for his advice and support all through my career in graduate school. I would also like to thank Dr. Daniel T. Britt, another member of my committee, for his support and lab space to conduct the experiment which comprises one chapter of this dissertation. Finally, I would also like to thank Dr. Adbelkader Kara and Dr. Kevin R. Coffey for their service on my committee.

TABLE OF CONTENTS

LIST OF FIGURES

LIST OF TABLES

CHAPTER 1: INTRODUCTION

Reduced and high energy mineral surfaces are present on airless bodies throughout the solar system. The hard vacuum, cosmic rays, and solar wind endemic to the space environment ensure a variety of mineral surface states, from freshly-cleaved rocky bodies to regolith that has been weathered for several billion years. The chemical state of these mineral surfaces is known to strongly affect the behavior of these surfaces when exposed to various chemicals, from simple volatiles to amino acids and nucleobases. These systems, whose surfaces are frozen in disequilibrium, can remain unpassivated for long periods of time. The cold temperatures common in space prevent certain thermally-activated processes such as surface reconstruction and healing, and the lack of atmosphere prevents passivation. Additionally, bombardment by electrons and protons from the solar wind can induce other high-energy flaws such as Schottky defects, where cation-anion pairs are knocked from a lattice which generally leads to a lower density material, or Frenkel defects, where an ion displaces into an interstitial site and does not lower density. All of these factors contribute to an environment wherein mineral surfaces are specially suited to drive many chemical and dissipative processes.

There is extensive scientific literature on the catalytic properties of minerals in general. Even on Earth, minerals such as clays and silicates are thought to have played a role in concentrating prebiotic chemicals via selective mineral surface interactions,[2] or in catalyzing the formation of complex prebiotic species.[3] Additionally, the Fischer-Tropsch reaction is a well-known process for forming hydrocarbons from simple feed-stocks (carbon monoxide and hydrogen) by leveraging the catalytic effects of metal surfaces.[4] Though this is typically thought of as an industrial process,[5] similar mechanisms have been proposed to form hydrocarbons in the space environment on mineral surfaces.[6]

The largest rocky bodies in our solar system—Earth, Venus, and Mars—have atmospheres of appreciable densities, but the three largest moons of Jupiter all have negligible atmospheres. Indeed, there is a wide variety of rocky, airless bodies in the solar system, from moons and planets to asteroids and meteorites, all of which are subject to the vagaries of the space environment. Many of these bodies are simply collections of smaller bodies, as with the regolith coating the surface of an asteroid which can be thought of as loosely cohesive dust with the consequent wide variety of surfaces and extremely large surface areas.

Organic molecules have been observed in several contexts in our solar system—in molecular cloud form[7] in our galaxy, and even in the center of other galaxies.[8] Organic matter has been theorized to play a role in enhancing adhesion during asteroid aggregation.[9] Over 50 organic molecules have been observed on comets alone.[10,11] These feed-stocks, present in molecular cloud form, can adsorb onto any rocky surface which happens to pass through them. Evidence for complex extraterrestrial organic chemistry has been observed in meteorites, such as the Murchison meteorite, which was found to contain nucleobase-related chemicals produced in space.[12] Additional analyses of meteorites point to a wide range of chemistry occurring in space[13] on mineral surfaces. Observations made on multiple airless rocky bodies such as Ceres,[14] Mercury,[15] and Iapetus[16] all show evidence of complex carbon chemistry. Additionally, there has been some reporting done on the spatial correlation of specific minerals and complex organics on various mineral surfaces in the space environment.[17] Altogether, mineral surfaces in the solar system exhibit a rich variety of complex carbon chemistry.

Dust Grains as Mineral Surfaces

In 1930, Trumpler[18] was the first to recognize that the space environment contained a substantial amount of dust. We now know that dust is widespread throughout space, although its density varies

greatly depending on its location. In planet and star forming regions, micron-scale dust accounts for one percent of the mass of those regions. In general, the size of this dust varies from clusters of a few atoms to above micron scale. The composition of this dust is varied and includes a diverse collection of silicates, carbonaceous grains, and even metals and metal oxides.[19] The very first dust came from the first generations of stars. This dust was then dispersed throughout the universe, eventually collecting into protoplanetary discs (PPDs) which then turned into stars and their attendant planets, including our own solar system. In the typical PPD environment, turbulence within gas flows herd dust together into aggregates which then further collide and coalesce. Figure 1.1a depicts a PPD around the star HL Tauri, observed by ALMA. Figure 1.1b shows an interplanetary dust aggregate imaged via scanning electron microscopy.

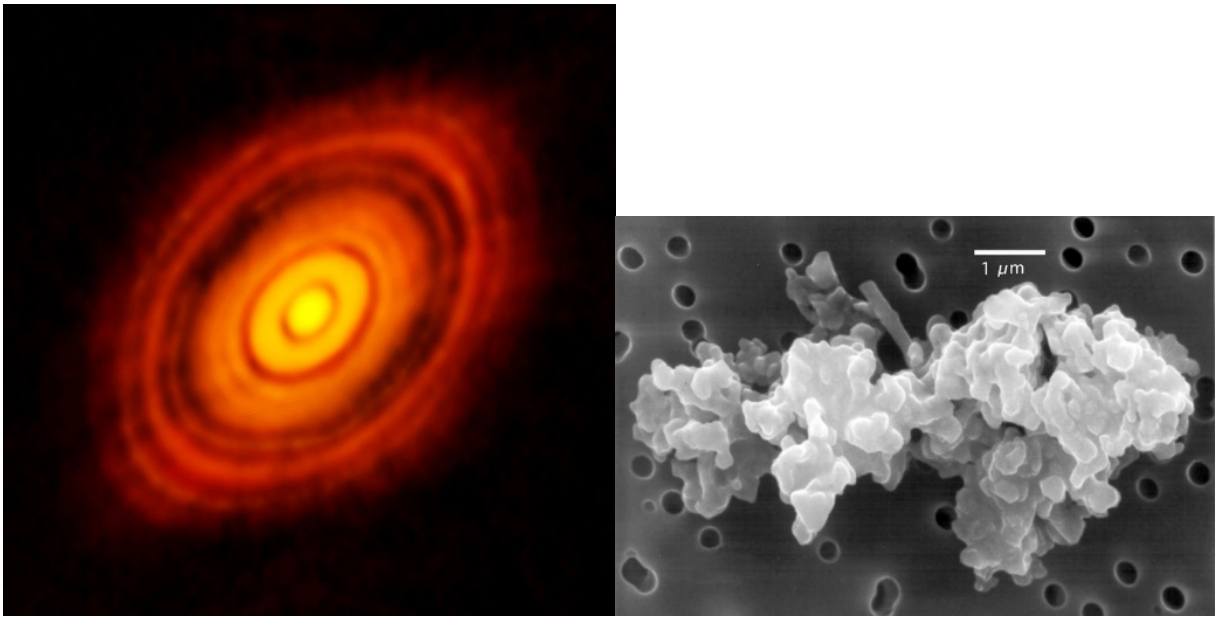

Figure 1.1: LEFT: (a) The star HL Tauri and its PPD. Image credit: ALMA (ESO/NAOJ/NRAO), CC 4.0. RIGHT: (b) SEM microscope image of an interplanetary dust particle. Image credit: Donald E. Brownlee, University of Washington, Seattle, and Elmar Jessberger, Institut für Planetologie, Münster, Germany, CC 2.5

These microscopic dust grains eventually coalesce and aggregate to become planetesimals with

diameters >1 km, at which point they are large enough for self-gravity to hold them together rather than adhesive effects.[20] The largest rocky planets can get far bigger—tens of thousands of km in radius. Even in a mature solar system such as ours, there is still a substantial amount of dust present. There are bands of dust which accompany each of the inner planets even at Mercury's orbit,[21] and at the asteroid belt and around Jupiter's orbit, the supply of dust which produces the zodiacal light is continually renewed.[22] Planetary formation simulations of these collisions are handled very well by Smooth Particle Hydrodynamics or coarse-grained (CG) codes,[23–27] which typically effect accretion by using Hamaker constants, thus making incomplete assumptions about dissipation. These codes have been used to model the adhesive behavior of micron-scale dust grains and their subsequent accretion, but when the dust grains reach roughly millimeter scale, a problem emerges: the mm bouncing barrier.[28] Two ways to obviate this problem are to either introduce a few larger grains, which allows growth to start again, or to take a Maxwellian velocity distribution of grains into account. Another possibility to enhance adhesion is additional dissipation, which is not accounted for by these models and which will be the focus of some of this work.

Non-atomic but nonetheless nano- and micron-scale collision simulations of sub-kilometer aggregate formation are carried out using van der Waals force-type models, sometimes with the addition of rolling friction.[29] These theories seem to partially explain aggregates, but there are some experiments that suggest van der Waals forces are not sufficient to hold certain aggregates together. For example, Scheeres et al. in 2010 performed an analysis of the likely forces present on an asteroid surface and hypothesized that van der Waals attraction could dominate the behavior of certain aggregates.[23] A few years later, Sanchez et al. confirmed this hypothesis via simulation, finding that van der Waals forces are indeed sufficient to hold aggregates together, and that the strength of cohesion is size dependent and decreases as asteroid diameter increases.[24] However, these same forces have been found insufficient to hold aggregates together under certain dynamic conditions, such as when a dust grain strikes a loose rubble pile aggregate.[25] In these coarse-grained sim-

ulations inter-grain interactions are typically characterized by the material's Hamaker constant, though these Hamaker constants are only found to vary weakly from material to material.[30] Thus, there must be additional forces acting on a shorter range which enhance adhesion.

Dust Grains as Catalytic Sites

Interplanetary and interstellar dust was thought to be inert until the 1960s, but in recent years it has become clearer that chemistry at the surfaces of dust grains in space is an important factor in planetary science. For example, it has been realized that gas-phase chemistry is insufficient to account for the population of H_2 detected in space,[31] whereas a proposed mechanism of adsorption and reaction of individual H atoms on surfaces has been moderately successful at explaining the prevalence of molecular hydrogen in interstellar space.[32] It is now accepted that dust grain surfaces are required to explain the abundance of H_2 that has been observed in space in much higher abundance than can be accounted for with gas-phase chemistry.

Dust grains surface chemistry is also thought to be especially responsible for the generation of larger molecules. That being said, the relatively high abundance of H_2 observed in molecular clouds serves as a good example of the effects of dust-grain catalysis. Molecular hydrogen is generally dissociated by UV radiation. When two bare hydrogen atoms meet and attempt to form H_2 by simple radiative association, the energy required to be radiated (over 4 eV) ensures that this does not happen due to quantum selection rules. A third hydrogen atom taking part in the collision could help dissipate this energy, but these three-atom collisions are very rare. Therefore, an alternative mechanism is needed. Dust grain surfaces both provide a heat sink to absorb the excess energy produced during bond formation and also present a substrate on which hydrogen atoms can diffuse and meet each other.[33] While the origin of the variety of organic and prebiotic molecules seen in the space environment is not completely understood, their formation may occur

in a fashion similar to H_2 formation: on the surfaces of dust grains. Dust grains, as a type of mineral surface, could conceivably produce everything from molecular hydrogen to amino acids and nucleobases. Specific mechanisms and processes responsible for the production of these chemicals will be investigated in detail by this thesis.

The Need for Dissipation and the Effect of Chemistry

In PPDs, dissipation is required to ensure that dust grains adhere. If one simply considers conservation of energy, the kinetic energy of relative translational motion must be dissipated somehow in order to ensure adhesion. Though rocky planets can be tens of thousands of kilometers in radius, their initial planetesimal growth still required dust grains to adhere on the micron scale to build up their components. This problem in particular is interesting because it is essentially an atomic-scale investigation of the initial formation of even the largest rocky bodies.

An important aspect of dust grain chemistry is related to dissipation and adhesion in the early stages of planet formation.[34] Dust grain collisions are typically studied by experiments[35,36] and modeled primarily using JKR (Johnson-Kendall-Roberts[37]) models. One characteristic of these previous efforts is that little attention has been paid to how surface chemistry affects adhesion and dissipation. Mentioned previously, one particular unresolved issue with past work is that observed dissipation (either from theory or experiment) appears to be inadequate to allow dust aggregates to grow beyond millimeter sizes,[28] let alone to the greater than $\sim$100m to 1 km size necessary for self-gravity to dominate cohesion.[20] In addition to generating new molecules, surface chemistry should play a role in atomic-scale adhesion and dissipation mechanisms.

Recent work in the field of tribology has begun to explore the role played by vapor-phase adsorption on adhesion, friction, and wear, demonstrating that adsorbates play a significant role in modifying the interactions between surfaces.[38,39] In fact, when simulating nanoscale collisions,

there is a certain similarity to the field of tribology, and specifically nanotribology. Here, the common picture of sliding friction is a series of nanoasperities serially vacuum welding, stretching, breaking, and rewelding. As these nanoasperities undergo plastic deformation, wear accumulates and macroscopic friction is seen to increase.[40] Likewise, when two micron-scale (or larger) dust grains collide, their surfaces are not perfectly smooth. There is nanoscale surface roughness, and thus, these surface features are of a scale readily modeled by molecular dynamics and even DFT.

Much of the understanding of grain-grain interactions, which play an important role in the accretion of planetesimals and planets, comes from Earth-based experiments with regolith simulants, where the interactions between sub-micron-sized particles may significantly affect product outcomes. The space environment, however, differs from the Earth-based environment where most experiments are conducted. Dangling bonds and defects are created on the surfaces of dust grains in space by high-energy events such as cosmic ray impacts, solar wind, or fragmentation during collision. When these dangling bonds or defects are generated at surfaces, or when free radicals are present, surface energy will increase. It is hypothesized that these surface characteristics in the space environment may contribute to stronger interactions and dissipative forces, allowing dust grains to aggregate more readily than predicted by extrapolation of existing experiments and theory. An essential idea of this work is that the chemistry in space is typically quite different than what is considered in experiments. In contrast to what happens at standard temperature and pressure on Earth, in the hard vacuum of space low temperatures and the lack of substantial atmosphere prevent the passivation and reaction of dangling bonds or free radicals. The author's research group have shown in a preliminary study using computational molecular dynamics that surface passivation plays a critical role in dissipation during grain collisions. These simulations are described in the following section.

Previous Coauthored/Relevant Work

NOTE :This section contains work done partially by this dissertation's author. It was published in full form and this dissertation's author was a co-author on this publication.

Abrar H Quadery, Baochi D Doan, William C Tucker, Adrienne R Dove, and Patrick K Schelling. Role of surface chemistry in grain adhesion and dissipation during collisions of silica nanograins. *The Astrophysical Journal*, 844(2):105, 2017

https://doi.org/10.3847/1538-4357/aa7890

To elucidate some of the effects of chemistry in nanometer scale grain collisions, atomic-scale simulations were performed using classical molecular dynamics (MD). Silicate grains, both amorphous and crystalline, have been used in the majority of collision experiments[42,43] and computational simulations,[44] both because silicates have been commonly observed in molecular clouds and protoplanetary disks and for ease of use. Thus, our simulations focused on elucidating chemical effects in collisional dissipation and adhesion for amorphous silica, a-SiO_2.

A ReaxFF potential and methodology was used to model a-SiO_2 nanoparticles. ReaxFF's many-body, bond order potentials are able to describe chemical reactions and bonding in different chemical environments. In addition, ReaxFF is able to capture the physics of charge transfer and transitions between metallic, covalent, and ionic bonding depending on how the chemical environment changes. A review of ReaxFF and similar methods can be found in Senftle's review article.[45] Specifically, the ReaxFF potential utilized[46] was developed to describe interactions between oxygen and a silica surface. This potential was based on previously published potentials that described materials involving silicon and silicon oxides, their interfaces, hydrolysis,[47] and interactions be-

tween a-SiO_2 and water.[48]

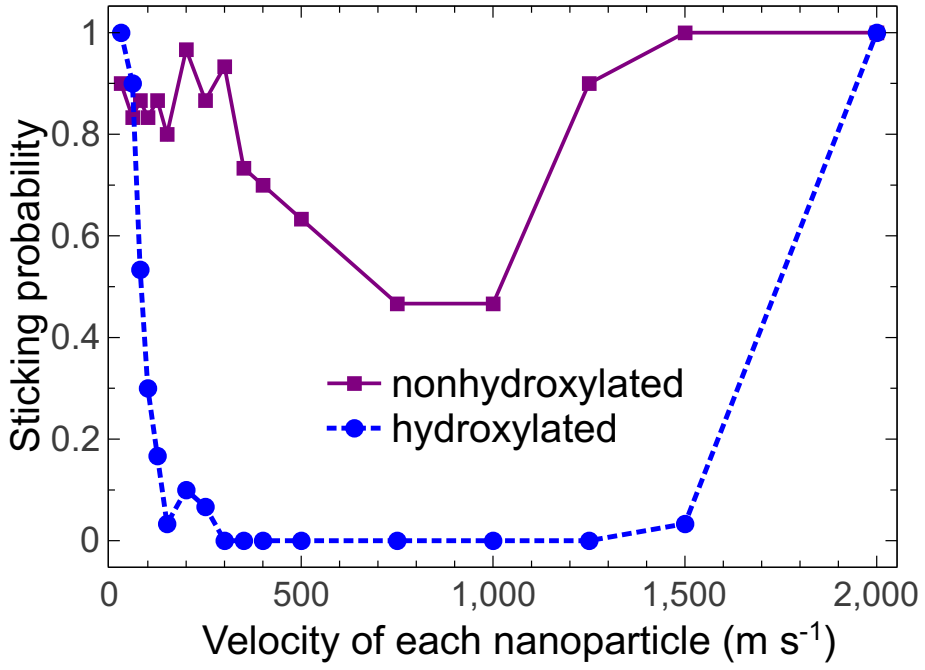

Figure 1.2: Outcomes of collisions of silica nanoparticles, for both the nonhydroxylated and hydroxylated cases, shown in terms of sticking probability for all collision velocities simulated.

To simulate collisions, the nanoparticles were initially placed such that the distance between their centers of mass was 100 Å. The nonhydroxylated nanoparticle was made of 894 SiO_2 units, and the hydroxylated nanoparticle was created by adding 88 H_2O units to the surface. After initial placement, both particles were imparted equal but opposite velocities in order to simulate a head-on collision. The directions of the velocity vectors were chosen to lie exactly along the vector that connected the center-of-masses of the two particles, and as a result the total angular momentum of the system was zero. Collisions were simulated for different relative velocities. Because the surfaces and shapes of the nanoparticles were not entirely uniform, it was expected that the outcome of collisions should be described by a statistical distribution. To sample the distribution, the nanoparticles were randomly rotated before each collision, such that many different randomly chosen orientations were simulated per velocity. A plot exhibiting the probability that a sticking

event will occur for a given velocity is presented in Figure 1.2.

The irreversible work of adhesion W_{adh} is defined by the ground-state energy difference,

$$W_{adh} = U_i^{(0)} - U_f^{(0)}, \tag{1.1}$$

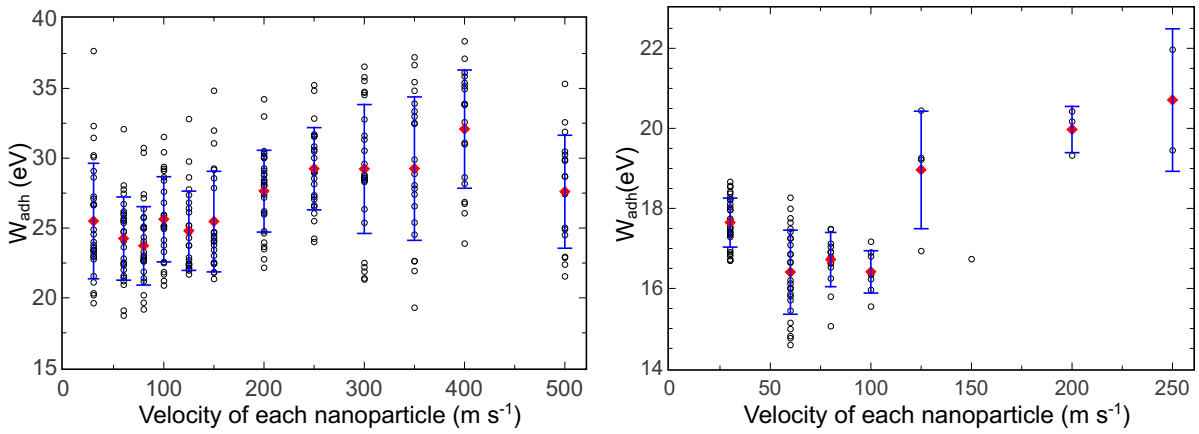

Figure 1.3: The work of adhesion calculated for a (left) nonhydroxylated and (right) hydroxylated silica nanoparticle involved in the collisions where the outcomes were sticking of the particles.

Applying the equipartition theorem to the kinetic and potential contributions to the internal thermal energy, and using conservation of energy, the work of adhesion becomes,

$$W_{adh} = 3Nk_B(T_f - T_i) - K_{trans}, \tag{1.2}$$

Where the initial and final temperatures of the grains are given by T_i and T_f, and K_{trans} is the translational kinetic energy of the grains before the collision in the center of mass frame. This derivation makes it clear that W_{adh} represents the change in ground state potential energy associated with formation of chemical bonds at the interface between the colliding particles. For all the collisions discussed here, T_i was less than 20 K. Works of adhesion are plotted in Figure 1.3 for all

collisions where the outcome was a sticking event.

In the case of partial dissipation, the particles do not adhere but instead bounce with diminished translational kinetic energy. For these cases, the coefficient of restitution (COR) was computed using the following formula:

$$COR = \frac{v_f}{v_i}. \tag{1.3}$$

Here, v_i and v_f are the relative speeds of the nanoparticles before and after the collision. For bouncing events as for sticking events, most of the kinetic energy was dissipated as vibrational thermal energy, although some rotational kinetic energy was observed as well. In the limit where the COR approaches unity, the collision becomes nearly perfectly elastic and reversible. By contrast, very small COR values indicate that a sticking event nearly occurred. In a sticking event, the COR is exactly zero. Coefficients of restitution are plotted in Figure 1.4 for all collisions where the outcome was a bouncing event.

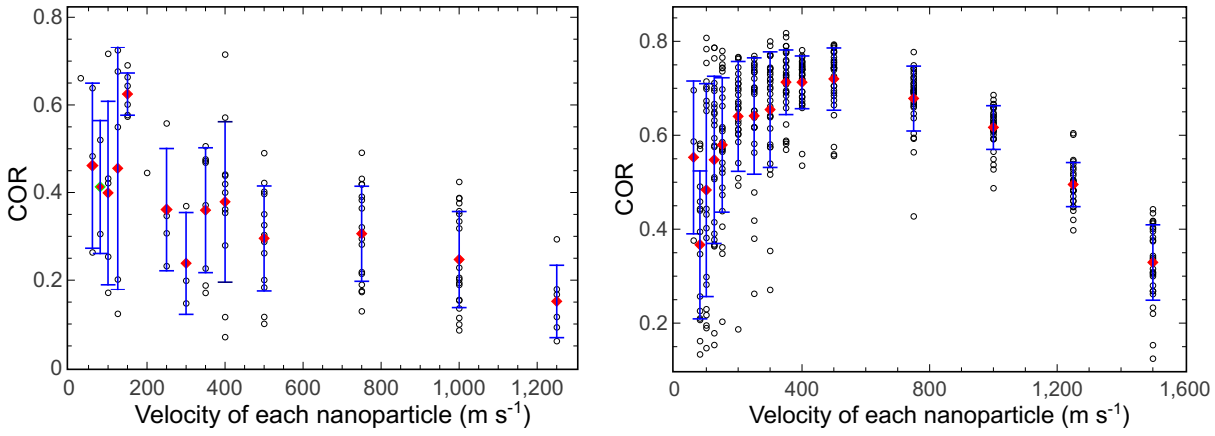

Figure 1.4: Coefficients of restitution (CORs) calculated for collisions of (left) silica nonhydroxylated nanoparticles and (right) silica hydroxylated nanoparticles that resulted in bouncing events.

The velocity at which a particle will begin bouncing (typically in more than 50% of collisions) is called the critical velocity. A discussion of the calculation of critical velocities can be found in an

article by Kimura et al.[49] Using Eqn. 1 from the Kimura paper, which is derived using JKR theory, the critical velocity for these nanoparticles would be, in the center of mass frame, 143 m s^{-1} for our nonhydroxylated nanoparticle, and 177 m s^{-1} for the hydroxylated nanoparticle. Irreversible dissipative behavior is a plausible explanation for the discrepancy in observed critical velocities in Fig. 1.2 compared to the critical velocities predicted by the equation given by Kimura et al., which is based on the assumption that the work of adhesion is related to the effective contact area A_{eff}, grain surface energies γ_1 and γ_2, and the interfacial energy γ_{12}, in the following way:

$$\frac{W_{adh}}{A_{eff}} = \gamma_1 + \gamma_2 - \gamma_{12} \tag{1.4}$$

In a collision between two identical spheres which have no substructure, such as in the JKR model, $\gamma_1 = \gamma_2$, and $\gamma_{12} = 0$. However, in a realistic collision simulated at the atomic scale, this is not a reversible process. One cannot simply create and destroy two surfaces by peeling apart two halves of an object and then joining them perfectly together again. Therefore, γ_{12} will not vanish, and the work of adhesion is not simply a stand-in for the surface energy. Additionally, this means that JKR theory alone cannot explain the change in adhesion when hydroxylating a surface. When adsorbates (in our case, dissociated water molecules) were present on the surface of two colliding objects which stuck, they became embedded within the interface between the two objects. This demonstrates another way in which the interfacial energy $\gamma_{12} \neq 0$.

To emphasize the point that strong chemical bonds, rather than weak van der Waals interactions, are responsible for dissipation and adhesion, using a pair potential[50] the dependence of the attractive force component was determined along the direction of motion of the colliding particles, denoted by F_y, on the particle separation r. For separations where van der Waals interactions dominate, F_y should scale as $F_y \propto r^{-7}$. When the particle separation becomes small, higher-order multi-polar interactions become dominant, as can be seen in Figure 1.5. Van der Waals interactions alone

cannot account for this behavior. Because the attractive interactions in this pair potential model are entirely Coulombic interactions characteristic of ionic bonding between point charges, without covalent bonding terms, the results demonstrate that strong ionic bonds form during collisions.

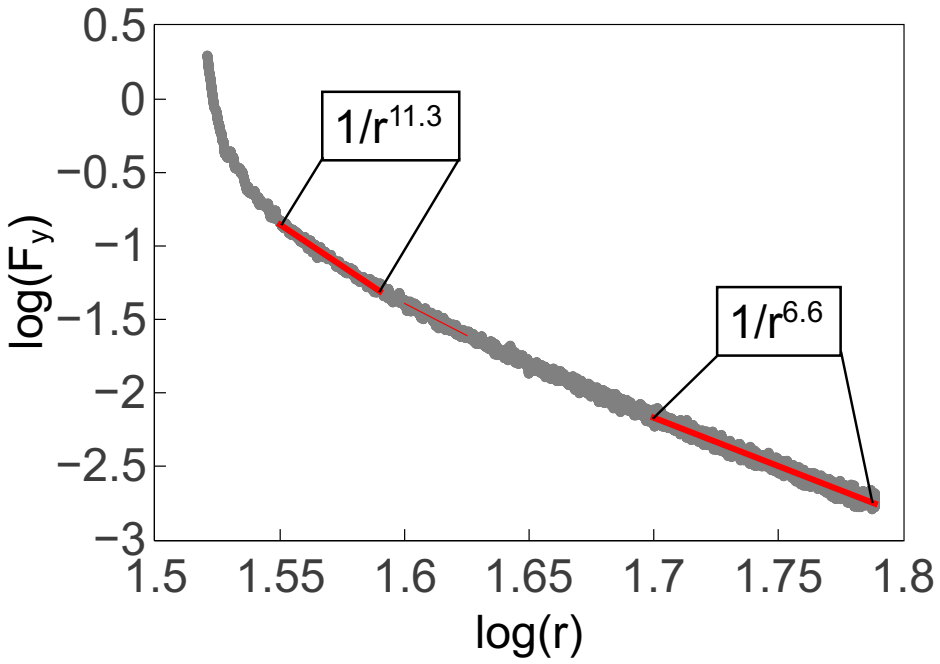

Figure 1.5: Pair-potential force component in the direction of motion of colliding (relative speed of 20 m s^{-1}) nonhydroxylated nanoparticles (F_y), plotted in a log-log scale as a function of inter-particle separation. The change in slope indicates the predominance of van der Waals interactions only at longer distances and a much stronger force at closer distances.

The results presented here show that during grain collisions, strong chemical forces, rather than simply weak van der Waals interactions, come into play and can lead to bond formation. Through bond formation, kinetic energy is dissipated effectively, a requisite for particle adhesion or sticking. Consequently, whether two particles will stick following a collision will depend on the likelihood of chemical bond formation at the grain interface, which is highly dependent on the chemical state of the grain surfaces. In fact, the work of adhesion was comparable to surface energies calculated in ancillary simulations. In the context of the space environment, in which high energy surfaces

are produced by high energy events, it is important to stress the correlation of surface energy to the work of adhesion. Our initial simulations demonstrate that adhesion was more pronounced during collision events in which the colliding particles were nonhydroxylated. This outcome was due to the presence of dangling bonds on the surfaces, which helped form strong chemical bonds between the colliding particles. When the dangling bonds were passivated through surface hydroxylation, the probability of adhesion and also the energy of adhesion were significantly reduced.

A Note on the Choice of Iron and other Simulation Details

All chapters in this work refer to iron nanoparticles in some fashion. In an experimental context, olivine is a common mineral in space, and it has been directly observed that nanophase iron is present on space-weathered olivine surfaces in the space environment on the S-type asteroid 25143 Itokawa.[51] Gaffey et al. have also shown that the optical properties of S-type asteroids can be explained by the presence of nanophase iron.[52]

In addition to the above evidence that iron nanoparticles are present on mineral surfaces in the space environment, iron is an ideal material for the modeling and analysis of dissipation during collisions. It is a single element mineral that affords the use of efficient computational algorithms. In addition, it shows strong dissipative effects and possesses a high melting point. As a model material, iron represents an extreme in unpassivated mineral surfaces. Many radical and organic species readily adsorb on iron surfaces. Therefore, for all collision studies, amorphous iron nanoparticles were chosen. The properties of these simulated nanoparticles are first described in chapter 3, but are also explored in chapters 4 and 5.

In some simulations, relative velocities can extend beyond those typically expected to be encountered in the context of a protoplanetary dust cloud. However, simulating collisions at these high

velocities allows us to observe a variety of dissipative mechanisms up to and including bulk melting and phase changes. Additionally, as we will show in the chapters to come, at the nanoscale higher velocity collisions which result in plastic deformation may be inevitable.

In the Chapters to Come...

Our initial study showed more attention should be focused on the chemical state of mineral surfaces in experiments, including how representative the surface chemistry is in comparison to minerals in the space environment. These observations opened up new directions for future computational studies of protoplanetary grain-grain interactions which elucidated other roles played by dissipative and chemical interactions in grain-grain collisions, and how those interactions affect the growth of planetesimals.

The remainder of this work is organized in the following manner: First, chapter 2 investigates the catalytic potential of iron nanoparticles on the surface of olivine dust and demonstrates a pathway for the chemical evolution of volatiles and organics in the space environment. Next, dissipative interactions are studied in a physical fashion in chapters 3 and 5, and the role of adsorbate chemistry on dissipation is studied in chapter 4. Finally, chapter 6 concludes this work.

CHAPTER 2: STRONG CATALYTIC ACTIVITY OF IRON NANOPARTICLES ON THE SURFACES OF REDUCED OLIVINE

Preamble

In this previously published article, the role of surface chemical states typical of the space environment is examined. Here, using olivine dust, a material widely found throughout the solar system, we use a previously established procedure to prepare and reduce this dust in a simulated space weathering procedure which results in a large amount of nanophase iron being present upon the grain surfaces. In this chapter, it is established that these mineral surfaces are very catalytically reactive for decomposing NH_3 and for generating large, complex carbon deposits when exposed to CO and H_2.

NOTE : This chapter contains previously published content, which is used in accordance with the journal's copyright policy for usage in dissertations.

William C. Tucker, Abrar H. Quadery, Alfons Schulte, Richard G. Blair, William E. Kaden, Patrick K. Schelling, and Daniel T. Britt. Strong catalytic activity of iron nanoparticles on the surfaces of reduced olivine. *Icarus*, 299:502–512, 2018

https://doi.org/10.1016/j.icarus.2017.08.027

Abstract

It is demonstrated that olivine powders heated to sub-solidus temperatures in reducing conditions can develop significant concentrations of 10-50 nm diameter Fe nanoparticles on grain surfaces

and that these display strong catalytic activity not observed in powders without Fe nanoparticles. Reduced surfaces were exposed to NH_3, CO, and H_2, volatiles that may be present on the surfaces of comet and volatile-rich asteroids. In the case of NH_3 exposure, rapid decomposition was observed. When exposed to a mixture of CO and H_2, significant coking of the mineral surfaces occurred. Analysis of the mineral grains after reaction indicated primarily the presence of graphene or graphitic carbon. The results demonstrate that strong chemical activity can be expected at powders that contain nanophase Fe particles. This suggests space-weathered mineral surfaces may play an important role in the synthesis and processing of organic species. This processing may be part of the weathering processes of volatile-rich but atmosphereless solar-system bodies.

Introduction

Research into space weathering has largely been focused towards strengthening the connection between spectral reflectivity measurements and the composition and morphology of mineral grain surfaces. In addition, there have been many efforts to better understand the mechanistic aspects of space weathering. One of the most characteristic and widely-studied aspects of space-weathering is the production of nanophase Fe ($npFe^0$), which is linked to darkening and reddening of the reflectance spectra, typically seen in lunar materials,[54] but also noted in returned samples from asteroids[51] and in simulated space weathering experiments on Fe- and Mg-rich minerals.[55] Yamada et al. showed that olivine will become significantly darker and redder when subjected to laser irradiation,[56] and in 2009 Vernazza et al. argued that darkening and reddening can happen on relatively short timescales (10^4 to 10^6 years) due to solar wind.[57] In Ref.,[52] Gaffey supplied a comprehensive overview of the optical properties of asteroids and the moon and provided evidence that $npFe^0$ is common throughout the Solar System. More direct evidence of $npFe^0$ has recently been obtained from samples of 25143 Itokawa S-type asteroid.[51] In short, several lines of evidence

point towards npFe^0 as a common feature of space-weathered mineral surfaces.

While there is widespread acceptance of the presence of npFe^0 on space-weathered surfaces and their optical activity, the chemical activity of exposed npFe^0 within a planetary science context has not been systematically investigated. The likelihood that mineral grains are involved in chemical reactions in the coma of comets has been hypothesized previously[58],[59] but very little is known about how this might occur. The recent Rosetta mission undertaken by the European Space Agency has yielded direct observations of organic matter on the comet 67P/Churyumov-Gerasimenko[6061].[62] Gillis-Davis et al. have shown that non-lunar-like spectral changes associated with nanophase and microphase Fe can be induced in asteroidal samples subjected to weathering,[63] while Kaluna et al. have presented evidence that the growth of micron scale carbon rich particles follows the production of npFe^0 in simulated space weathering experiments on Fe-rich minerals.[55] In this context, it is important to determine the conditions and rates for chemical reactions that can be catalyzed by npFe^0 on mineral grain surfaces, and also how these might vary with the specific composition and morphology of these mineral grain surfaces. There exists an extensive literature devoted towards understanding npFe^0 catalysis at mineral surfaces that can be brought to bear on this issue[58].[64] It is well known that metallic nanoparticles are strongly catalytic for many reactions. For example, npFe^0 supported on carbon nanotubes has been shown to be strongly active for Fischer-Tropsch reactions[56566].[67] Biomass steam gasification also been shown to be catalyzed by an impregnated iron/olivine mixture created by mixing iron nitrate and olivine in solution and utilizing the dried mixture as a catalyst.[68] Based on these previous studies, it seems entirely plausible that space-weathered mineral grain surfaces containing npFe^0 from reduced olivine might demonstrate very strong catalytic activity.

In this paper, we present experimental results demonstrating that olivine samples containing npFe^0 are strongly catalytic for chemical reactions involving NH_3, CO, and H_2, all volatiles known to be present in comets and at the surfaces of some volatile-rich asteroids[5969].[70] Our experimental

results show that npFe^0 present on the surfaces of space-weathered minerals can induce dynamical chemical evolution on mineral grain surfaces. At the most fundamental level, npFe^0 acts to catalyze the breaking and formation of chemical bonds. It is hypothesized that npFe^0 could be important for the growth of larger organic molecules from smaller volatiles (e.g. PAHs, NH_3, CO, and H_2) that are probably found on or near the surfaces of volatile-rich small bodies such as asteroids and comets. Our primary focus is on chemical changes that may occur post-accretion as part of regolith processes of atmsophereless bodies. For this chemistry to occur, reaction feedstocks in the form of volatiles need to be present. In addition to facilitating the growth of larger species, under the right conditions npFe^0 might also act to decompose complex carbon materials known to exist in carbonaceous chondrites.[13] This work demonstrates that the characteristic morphology and composition of space-weathered asteroidal regolith results in distinct chemical properties, and provides a new perspective on the importance of space-weathering phenomena.

Experimental Methods

A schematic of the experimental apparatus is shown in Figure 2.1. The manifold was milled from a single block of aluminum, and threads were cut into the manifold to accommodate 1/4" NPT fittings. All tubing connecting the pieces of the apparatus was made of 1/4" 316L stainless steel. Standard Swagelok fittings were used throughout the apparatus. Temperature in the tube furnace was controlled with an Omega CN7853 temperature process controller. SSI Technologies P51 series pressure transducers (model number P51-100-A-A-I36-20MA), which measure pressure against an internal vacuum reference, allowed pressures to be recorded on a computer. The total volume of the system was measured to be 23.8 cm^3.

For our study, we chose Fo_{90} San Carlos olivine, which has been studied and characterized extensively. San Carlos olivine is approximately 90% forsterite (Mg_2SiO_4) and 10% fayalite (Fe_2SiO_4).[71]

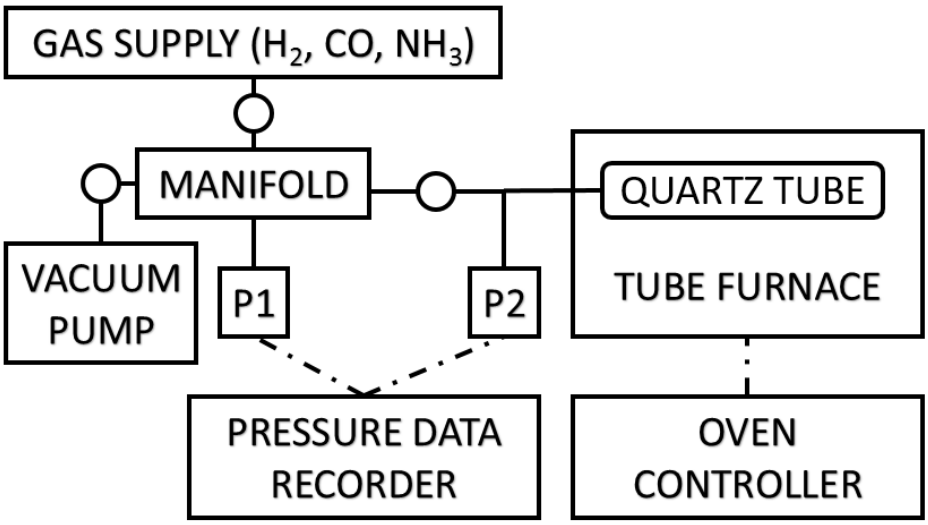

Figure 2.1: Schematic of the constructed apparatus used in the experiments. In this schematic, the solid lines between components indicate steel tubing, P1 and P2 indicate pressure transducers for automated pressure recording, and the dashed lines indicate data wiring. The circles indicate the position of valves allowing control of gas flow, permitting isolation of certain parts of the system.

To generate surfaces with npFe^0, the approach in Ref.[72] was followed in general, but with some variations in the specific details. At each stage of the process, powders used in the reaction were reserved for analysis. A summary of these samples can be found in Table 2.1. First, approximately 35 grams of olivine were ground via high-energy ball-milling in an 8000M SPEX CertiPrep mixer/mill. The milling vial was constructed of tungsten carbide with an approximate volume of 65 ml. Viton flat o-rings were used to maintain a seal during milling. Kinetic energy was supplied for 30 minutes with three 12.7 mm tungsten carbide balls weighing approximately 16.7 g each. The powders were then sieved through a #325 mesh to produce a fine-grained white powder with a grain size of 44 microns or smaller; a portion of this power was set aside as sample A1. Milled powder was loaded into the quartz tube with one end open to the ambient air. The system was then heated to T = 750° C for one hour, and subsequently allowed to cool in air, yielding sample A2. The result of this heating step is the decomposition of the surface material of the olivine grains and

the production of nanoscale iron oxide particles. The increase in temperature simulates the energy input from energetic particles such as micrometeorite bombardment. Reaction temperatures were chosen to be substantially under the solidus of olivine but high enough to produce decomposition, reduction, and catalytic reactions in modest time scales. Specifically, this initial temperature T = 750° C was chosen as it is high enough that the iron within the olivine lattice will become mobile, but it is low enough such that the magnesium or silicon will not become mobile[73].[74]

Table 2.1: Descriptions of samples

Sample ID	**Preparation method**
A1	250mg ball milled olivine, sieved
A2	250mg ball milled olivine, sieved and annealed in air for 1 hour at T = 750° C
A3	250mg ball milled olivine, sieved and annealed in air for 1 hour at T = 750° C, then reduced in 10 cycles of H_2 at T = 500° C for 10 minutes per cycle, then used to decompose NH_3 at T = 650° C for 30 minutes
A4	250mg ball milled olivine, sieved and annealed in air for 1 hour at T = 750° C, then reduced in 10 cycles of H_2 at T = 500° C for 10 minutes per cycle, then used to react CO and H_2 at T = 400° C for 138 hours
A5	250mg ball milled olivine, sieved and annealed in air for 1 hour at T = 750° C, then reduced in 10 cycles of H_2 at T = 500° C for 10 minutes per cycle, then used to react CO and H_2 at T = 450° C for 6.33 hours
A6	250mg ball milled olivine, sieved and annealed in air for 1 hour at T = 750° C, then reduced in 10 cycles of H_2 at T = 500° C for 10 minutes per cycle

To produce $npFe^0$, the next step was to reduce the olivine in H_2. Before introduction of H_2, the pressure in the quartz tube was reduced to ~ 0.004 PSIA or lower using a vacuum pump. In contrast to the approach reported in Ref.[72] which used a flow reactor, in these experiments reduction was achieved by 10 cycles of reduction with H_2 at a pressure of $\sim$ 20 PSIA H_2 and at a temperature of T = 500° C for 10 minutes per cycle. One of these reduction runs was set aside as sample A6 as a control to compare with powders used in reactions. The reduced powders were then used for reaction with NH_3 (yielding sample A3) and reaction with CO+H_2 (yielding samples A4 and A5). It was demonstrated repeatedly during these experiments that vaporization-producing temperatures

and highly energetic impacts, which are typically thought to be the mechanisms which create $npFe^0$ on regolith, are not required to generate $npFe^0$ on the surfaces of olivine grains in the laboratory setting.

While the pressure of the system was monitored during the reduction cycles, changes in pressure are not a reliable indicator of the progress of reduction, as an equimolar reaction takes place in which H_2 combines with oxygen on the olivine and then desorbs as water. Nevertheless, a rate constant was calculated for the H_2 reduction step by fitting to the pressure data of the first cycle and is reported below in Table 2.3, though this rate constant likely only represents the condensation of water on the tubing outside of the tube furnace. Subsequent reduction cycles produced no detectable pressure change.

To determine the catalytic activity, each batch of 250 mg of reduced olivine powder was kept under vacuum conditions after the reduction step. For reaction of NH_3 on the reduced powder, NH_3 was introduced to the quartz tube at a pressure of 17.0 ± 0.3 PSIA, and allowed to react at temperatures in the range between T = 500° C and T = 650° C; the T = 650° C run yielded sample A3. For reactions with an equimolar mixture of CO and H_2 (yielding samples A4 and A5), the reactant gases were introduced at a total pressure of 17.0 ± 0.3 PSIA. In the case of sample A4, the gases were allowed to react at T = 400° C over the course of 138 hours. For sample A5, the gases were introduced at the higher temperature T = 450° C and only allowed to react for 6.33 hours. The progress of all reactions was monitored by recording the pressure within the quartz tube over time using a pressure transducer.

The powders were analyzed using reflectance spectra, X-ray photoemission spectroscopy (XPS), transmission electron microscopy (TEM), scanning transmission electron microscopy (STEM), electron energy loss spectroscopy (EELS), and Raman spectroscopy. The TEM and STEM imaging and EELS analyses were obtained using an FEI Tecnai F30. The XPS analysis was performed with

a Physical Electronics 5400 ESCA spectrometer, and charge correction was done by correcting 1s carbon to 284.6 eV. Raman spectra were measured in a back scattering geometry with a micro-Raman setup (Horiba Jobin Yvon LabRam HR) at a spatial resolution of 2 microns. Raman spectra were excited at a wavelength of 532 nm with light from a frequency-doubled Nd:YAG laser. The power at the sample was less than 4 mW. The spectral resolution was better than 2 cm^{-1}, and the instrument was calibrated using a naphthalene standard. Reflectance spectra were taken with an ASD FieldSpec Pro with an ASD A122300 contact probe. For TEM imaging and analysis, first a small amount of powder was shaken in a clean beaker filled with distilled water. Droplets of this water were then placed on a very fine-meshed copper screen and allowed to dry, thus depositing olivine grains on the screen. These screens were then loaded into the TEM.

The results described below support the observation that $npFe^0$ was produced on the surfaces of the olivine grains, and that strong catalytic effects exist due to the presence of $npFe^0$. In particular, when NH_3 was introduced to reduced olivine powder, the results were consistent with rapid decomposition. When CO and H_2 were introduced to the reduced olivine powder, the reactions were observed to produce primarily graphene and/or graphitic carbon, carbon onions, and possibly carbon nanotubes and nanohorns. TEM and EELS analysis showed that carbon species were spatially correlated with $npFe^0$. Finally, control experiments with either an empty quartz tube or unreduced powders did not exhibit significant chemical activity, further corroborating the strong catalytic effects of powders with $npFe^0$ on their surfaces.

Results

Changes in the olivine powders were analyzed by reflectance spectra. In Figure 2.2, the reflectance spectra for samples A1, A2, A6, and A4 are shown. The olivine powders obtained from ball-milling, labeled as A1, show the characteristic olivine absorption band minimum at 1 micron.

Table 2.2: Properties of reflectance spectra for samples A1 and A6.

Sample	Slope (μm^{-1})	Reflectance @ 550 nm	1μm band center (nm)	1μm band depth
A1	0.038	0.75	1050	0.13
A6	0.42	0.15	n/a	n/a

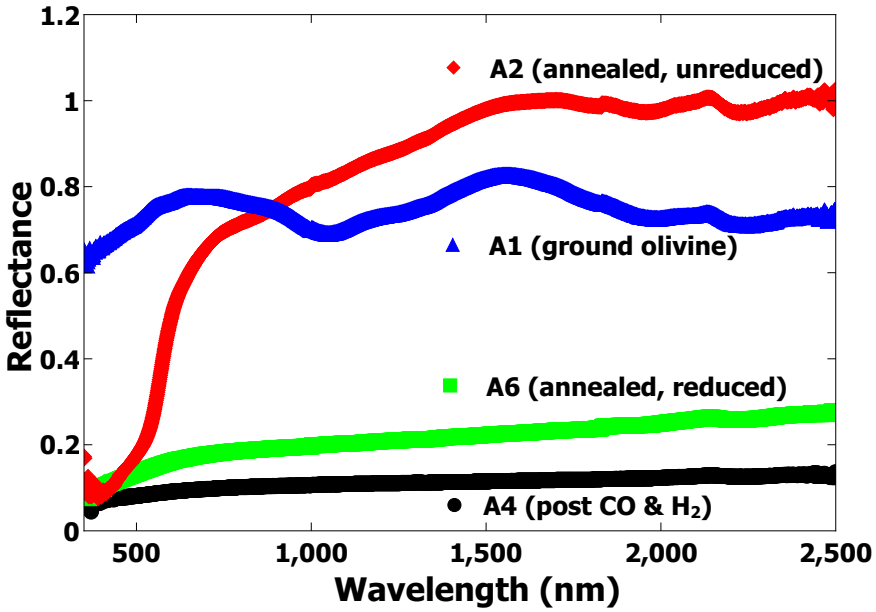

Figure 2.2: Reflectance of samples A1, A2, A6, and A4. The dip at 1 micron for sample A1 is a typical marker for olivine and is caused by iron cations in the olivine lattice. The feature around 2.15 microns is an artifact of the white reference. Sample A2 is significantly redder than sample A1 due to iron oxides that were created by the annealing process. Sample A6, which appears dark gray, has been reduced with hydrogen. Sample A4 is darkened further due to coking.

This feature at 1 micron is due to the presence of three overlapping bands caused by iron cations in the crystal structure of the fayalite fraction of the olivine sample[75]. After the first heating step in air, A2 showed a strongly reddened spectra consistent with the decomposition of olivine and the production of nanoscale iron oxides on the grain surfaces[76], with a similar slope to the spectra of hematite/magnetite mixtures but without exactly matching the spectra of these iron oxide mixtures[77]. The next heating step in H_2 reducing conditions converted the iron oxide to npFe^0 in

sample A6 which exhibited a substantially diminished reflectance.

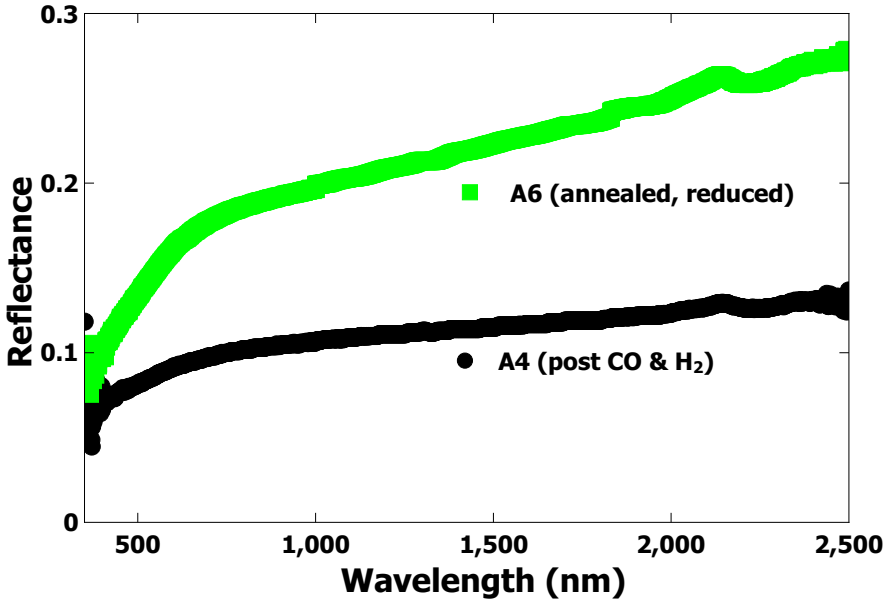

Figure 2.3: Detailed view of reflectance spectra of samples A6 and A4. The feature around 2.15 microns is an artifact of the white reference. Sample A6, which appears dark gray, has been reduced with hydrogen, and does not exhibit an absorption band at 1 micron. Sample A4 is darkened further due to coking.

Details of the spectra for samples A1 and A6 are summarized in Table 2.2 and were calculated in the same manner as the spectra parameters in Kohout et al.[72] A 1 micron absorption band was not observed in the spectra for sample A6. This change in reflectance for sample A6 is consistent with the conversion of iron oxides to $npFe^0$ as reported by Kohout et al.[72] and is characteristic of the reflectance spectra of space-weathering and the presence of $npFe^0$, though the degree of flattening visible in Figure 2.3 is far greater than the flattening observed in asteroid spectra,[78] indicating that the amount of $npFe^0$ present in A6 was likely greater than that found in naturally occurring regolith in the space environment. By utilizing the linear fits to data in Kohout et al.,[72] we calculated that sample A6 was approximately 0.027% $npFe^0$ by weight when using Kohout's fit to spectral slope, and was 0.059% $npFe^0$ by weight when using Kohout's fit to albedo at 550 nm. Averaging these

two values yields a $npFe^0$ weight percentage of 0.043%. The iron from the fayalite fraction of sample A1 accounts for approximately 8% of the sample weight. Therefore, about 0.5% of the iron available within sample A1 has been converted to $npFe^0$ in sample A6. The reduced powders reacted with CO and H_2 at T = 400° C, labeled A4, showed a very strong decrease in reflectance. Note that all samples show a spectral dip at approximately 2.1 microns. This is an artifact caused by the Spectralon Diffuse Reflectance Standard white reference.[79]

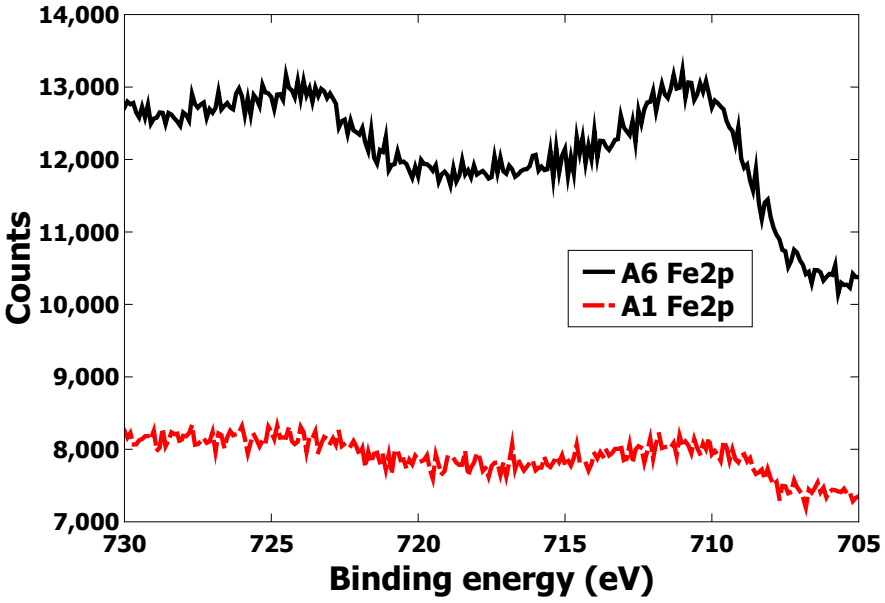

Figure 2.4: XPS analysis of samples A1 and A6. In sample A1 (lower dashed red line), the slight peaks are likely due to iron-oxygen interactions within the crystal structure of the olivine. Sample A6 (upper solid black line) exhibits much more prominent Fe2p peaks, showing that there is much more iron at the surface of the sample after annealing.

Figure 2.4 shows the XPS data collected for samples A1 and A6. Both the unreduced (A1) and reduced (A6) samples show peaks at 712 eV and 726 eV, attributed to $Fe2p_{3/2}$ and $Fe2p_{1/2}$ respectively in an oxidized state.[80] Even unreduced olivine can exhibit a signal at these energies from the iron in the olivine crystal structure,[81] but the observation of stronger peaks in A6 is consistent with Fe segregation at the surface. However, there was no evidence of peaks at 707 eV and 720

eV which would be characteristic of elemental Fe.[80] This is not surprising as XPS typically has a detection limit of 0.1% to 1% in terms of number of atoms.[82] From the estimate in the previous paragraph, only 0.5% of the iron present within sample A6 had been converted to $npFe^0$. Thus, the amount of iron present in sample A6 as Fe^0 was possibly below the detection threshold. Additionally, it is very likely that oxidation of the $npFe^0$ occurred, since the powders were removed from the quartz tube and exposed to air before XPS analysis. In Figure 2.5, which presents the Raman spectra of samples A1, A2, A3, and A6, we observe the characteristic vibrational bands for olivine. In all four samples depicted in the figure, namely samples A1, A2, A3 and A6, the olivine characteristic peaks caused by SiO_4 stretching modes[83] are visible at 820 cm^{-1} and 850 cm^{-1}.

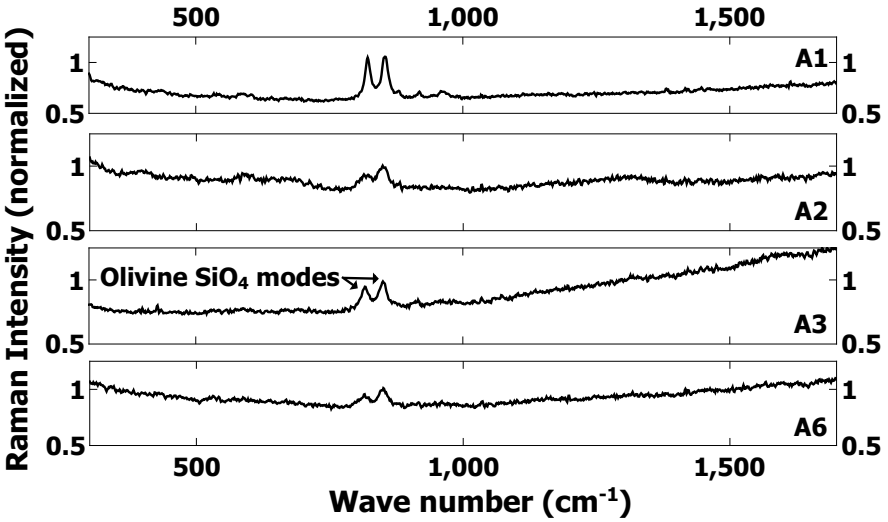

Figure 2.5: Micro-Raman spectroscopy analysis for samples A1 (ground olivine), A2 (annealed and unreduced), A3 (annealed and reduced, then used to decompose ammonia), and A6 (annealed and reduced). Raman intensities have been normalized to 850 cm^{-1}.

STEM analysis of the reduced sample A6 indicated the presence of significant concentrations of $npFe^0$. A representative image is presented in Figure 2.6 which shows clear evidence of the presence of $npFe^0$ on the olivine grain surfaces. In the left panel of Figure 2.6, the yellow box delimits an area for detailed high-angle annular dark-field imaging (HAADF) to determine composition.

The center panel of Figure 2.6 shows this analyzed area in HAADF mode. In the right panel of Figure 2.6, the detailed composition maps generated from EELS spectra show the location of oxygen ions and the npFe^0. The npFe^0 particles appear to be approximately 15 nm in diameter and are evenly spaced on the olivine grain surface. The regions with high oxygen composition tend to correlate with a weak Fe composition, and hence appear to be regions of the olivine grain surface without npFe^0.

Figure 2.6: STEM analysis of sample A6 (reduced and unreacted sample). The leftmost panel shows the olivine grain with multiple bright spots. A scale bar is provided. The inset square indicates the area which was analyzed by EELS, and measures 60 nm $\times$ 60 nm. The middle panel shows the analyzed area in HAADF mode, with each pixel being a 2 nm $\times$ 2 nm square. EELS data were extracted from this area and used to create the elemental maps shown in the rightmost panel of images. The image on the top right shows the distribution of 1s O, and the image on the bottom right shows the distribution of 2p Fe. In these element maps, the brighter areas indicate the areas where more of these signals were detected.

The reduced powders with surface concentrations of npFe^0 were very reactive for the decomposition of NH_3. After introducing NH_3, the pressure in the quartz tube increased immediately. It is likely that the NH_3, catalyzed by the npFe^0, decomposed primarily to H_2 and N_2 in a reaction typically referred to as reverse Haber-Bosch,

$$2NH_3 \rightarrow 3H_2 + N_2. \tag{2.1}$$

If we assume the above reaction, then the fraction of NH_3 decomposed as a function of time $f_{conv}(t)$ can be determined by the initial pressure p_0 and the pressure $p(t)$ measured at time t,

$$f_{conv}(t) = \frac{p(t)}{p_0} - 1. \tag{2.2}$$

The fraction of NH_3 remaining at time t is then,

$$f_{rem}(t) = 1 - f_{conv}(t) = 2 - \frac{p(t)}{p_0}. \tag{2.3}$$

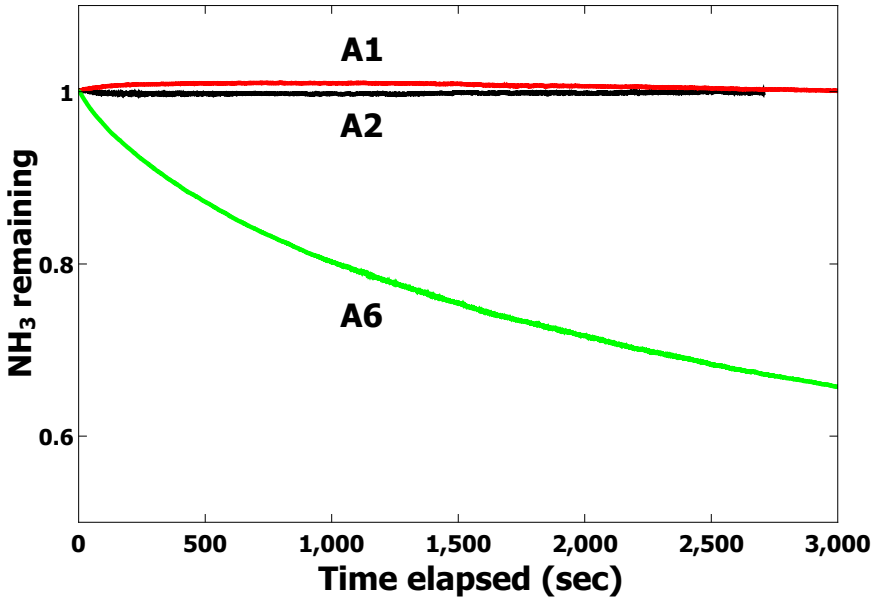

Figure 2.7: Fraction of ammonia remaining as a function of time elapsed for ammonia decomposition experiments at T = 500° C, calculated with equation 2.3, for three starting catalysts: A1 (ground olivine), A2 (annealed, unreduced olivine), and A6 (reduced olivine).

In Figure 2.7, $f_{rem}(t)$ is plotted as a function of time for an ammonia decomposition reaction at T = 500° C. It was observed that the rapid reaction rate only occurred on surfaces with $npFe^0$.

Supporting this, in Figure 2.7 $f_{rem}(t)$ is plotted for a quartz tube loaded with ground, unreduced olivine (A1) and olivine which had been annealed in air but not reduced (A2). In those two cases, a much slower rate of NH_3 decomposition was measured. Ancillary exploratory reactions showed that olivine prepared in the manner of A6 could decompose ammonia repeatedly with no loss of subsequent performance, indicating that the ammonia decomposition process did not poison the catalyst.

The results in Figure 2.7 are consistent with a first-order reaction, which is governed by the differential equation,

$$\frac{df_{rem}}{dt} = -kf_{rem}, \tag{2.4}$$

Where $f_{rem}(t)$ is the fraction of NH_3 remaining and k is the rate constant. The solution is then,

$$f_{rem}(t) = f_0 e^{-kt}. \tag{2.5}$$

In Table 2.3, the calculated rate constants k are presented for different reaction temperatures. To check that the catalytic activity was mainly due to the presence of the reduced olivine powder, reactions were also studied at higher temperatures with an empty quartz tube. These rate constants are also shown in Table 2.3. With an empty quartz tube, significantly higher temperatures were required for the decomposition reaction to proceed. This contrast between the reduced olivine powder and both the empty quartz tube and the unreduced powder demonstrates the catalytic properties of the reduced powder with surface $npFe^0$.

The natural logarithm of the rate constants for both the reduced powder and the empty quartz tube are plotted as a function of inverse temperature in Figure 2.8 Assuming thermally activated

behavior, linear fits to the points in Figure 2.8 result in the activation energies E_a for the two systems. The pre-exponential coefficients determined from the Arrhenius fits are significant in that the presence of the reduced olivine catalyst leads to a much smaller attempt frequency of 0.063 s^{-1} for reaction. In the empty tube reactions, there was a much larger attempt frequency of 4.8 s^{-1}. In spite of the significantly enhanced likelihood for collisions at the interface of the reduced olivine powders, the mechanism for reaction at those sites appears to be constrained to a far more limited range of incoming active-site/reactant configurations, such that the overall frequency of collisions taking place in reaction-possible orientations is actually much smaller than that at the surfaces of the tube. Because of this, significantly enhanced reaction rates correlating to the presence of the reduced olivine samples necessarily indicate greatly reduced activation barriers at the catalytic sites within the powders.

Table 2.3: Reaction rates for various experiments.

Experiment	Temperature (° C)	k (10^{-4} s^{-1})
Reduction with hydrogen (A2 $\rightarrow$ A6)	500	31.25
Ammonia decomposition, reduced olivine	500	4.49
Ammonia decomposition, reduced olivine	550	5.70
Ammonia decomposition, reduced olivine	600	8.12
Ammonia decomposition, reduced olivine	650	9.78
Ammonia decomposition, empty quartz tube	650	0.98
Ammonia decomposition, empty quartz tube	670	1.83
Ammonia decomposition, empty quartz tube	690	2.10
Ammonia decomposition, empty quartz tube	710	2.07
Ammonia decomposition, empty quartz tube	730	3.01
Ammonia decomposition, empty quartz tube	750	2.04
Ammonia decomposition, empty quartz tube	800	6.69
Ammonia decomposition, empty quartz tube	820	5.11
Ammonia decomposition, empty quartz tube	840	8.67
Ammonia decomposition, empty quartz tube	860	9.71
Ammonia decomposition, empty quartz tube	880	7.94
CO & H_2, reduced olivine (first 2×10^4 secs)	400	0.68
CO & H_2, reduced olivine (first 2×10^4 secs)	450	1.92

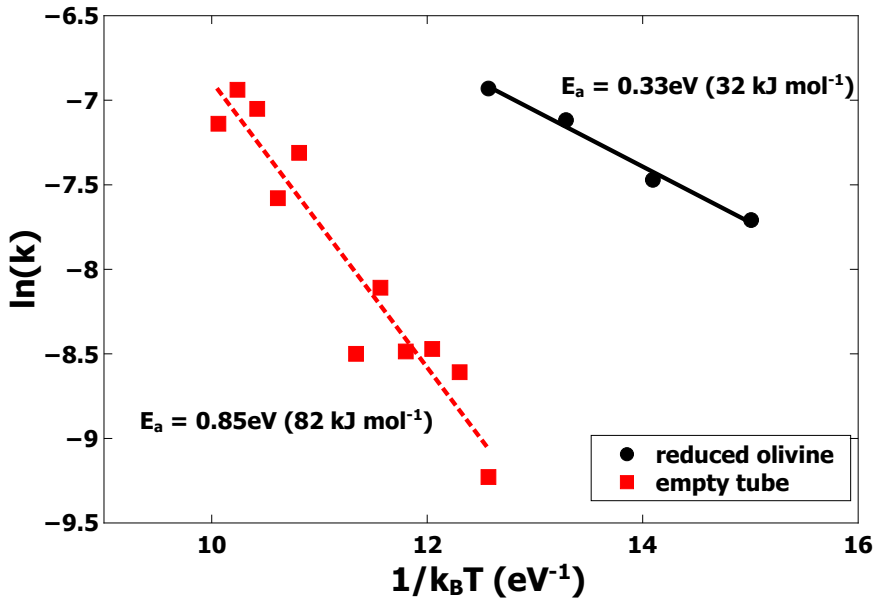

Figure 2.8: Arrhenius plots of the rate constants k for various temperatures for ammonia decomposition with no catalyst present (empty tube), shown as red squares, and with a catalyst present, shown as black circles. An activation energy of 0.85 eV $\pm$ 0.09 eV (82 kJ mol^{-1} $\pm$ 9 kJ mol^{-1}) was calculated for the reaction without a catalyst (red dashed line). For the reactions with a catalyst present, an activation energy of 0.33 eV $\pm$ 0.03 eV (32 kJ mol^{-1} $\pm$ 2 kJ mol^{-1}) was calculated (black solid line).

The activation energy E_a = 0.33 eV for the reduced olivine powder is substantially lower than E_a = 0.85 eV found for the empty quartz tube. This result shows that it is the reduced olivine powder which catalyzes NH_3 decomposition. This activation energy E_a = 0.33 eV is comparable to catalysts developed and studied specifically to decompose NH_3[84858687].[88] A comparison to NH_3 thermal decomposition activation energies from other experiments is given in Table 2.4. Sample A3 (which was used to decompose ammonia at T = 650° C for 30 minutes) showed no significant difference from A6 (reduced olivine with catalytically active npFe^0) in XPS, reflectance, and micro-Raman analysis.

Table 2.4: Ammonia decomposition activation energies E_a are given in both eV and kJ/mol.

Material	E_a (eV)	E_a (kJ/mol)	Notes	Ref.
Reduced olivine (this work)	0.33	32	npFe^0 present	This work
Fused iron (promoted)	0.99	96	Promoted with potassium	[84]
Fused iron (non-promoted)	0.90	87		[84]
Bulk iron (single crystal)	0.22 - 1.95	21 - 188	Various conditions and concentrations	[85]
Bulk iron	0.65	63		[86]
npFeN$_x$ on CNTs	0.90	87	With nitridation	[87]
npFe^0 on CNTs	1.66	160	Without nitridation	[87]
Quartz tubing (this work)	0.85	82		This work
Quartz sand	1.52	147	840° C to 960° C	[88]

The reduced olivine powders were also used to catalyze reactions with equimolar mixtures of CO and H_2, as described previously. In these experiments, the initial pressure was found to rapidly drop consistent with the formation of more complex and less volatile organic species. In Figure 8, the measured pressure inside the quartz tube is presented as a function of reaction time at T = 400° C. Since the dominant reaction pathways may change as temperature changes, pressure data by itself is a poor indicator of the progress of specific reactions. Nevertheless, one can still obtain rate constants by fitting to pressure data to show how the system overall evolves over time. Fitting the initial 2×10^4 seconds of the data in Figure 8 with the assumption of a first-order reaction yields a rate constant $k_{400^\circ C} = 0.68\ 10^{-4}\ s^{-1}$. Post-reaction powder was retained as sample A4 for further analysis. Another experiment at T = 450° C yielded similar results, but with significantly faster kinetics. A rate constant $k_{450^\circ C} = 1.92\ 10^{-4}\ s^{-1}$ was obtained in a similar manner via first-order fitting. The rate constants determined are given in Table 2.3. Finally, the powder obtained from reaction with CO and H_2 at T = 450° C for 6.33 hours was retained as sample A5 for further analysis.

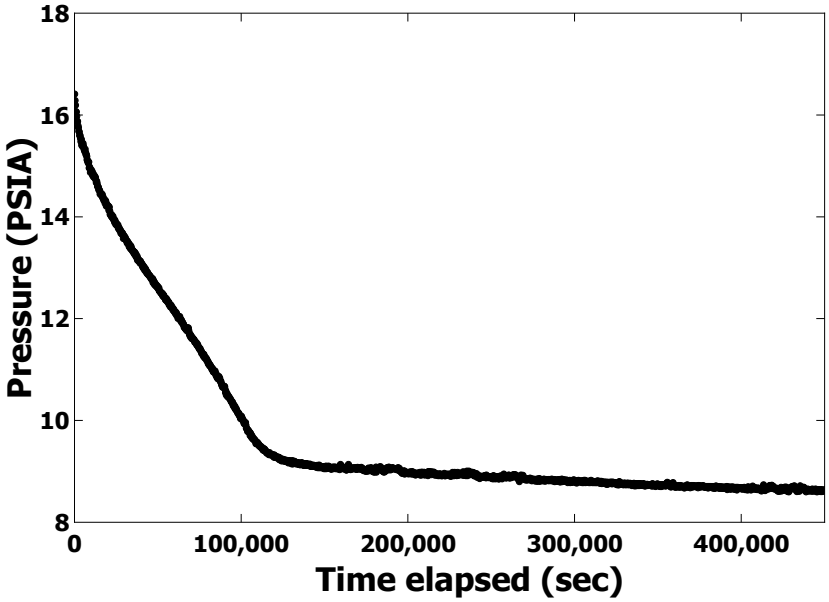

Figure 2.9: Pressure as a function of time elapsed for an equimolar carbon monoxide and hydrogen gas mixture reacted over reduced olivine at T = 400° C for 138 hours. The resulting coked powder was labeled as sample A4.

Empty tube reactions and reactions over A1-type powders were also studied for this gas mixture, but no significant pressure change was observed after several hours for either temperature. A very small pressure drop (less than 0.5 PSIA) was observed during the first ten minutes for the empty tube reaction, presumably due to gases adsorbing onto the inner surface of the quartz tubing. When this gas mixture was introduced to unannealed and unreduced olivine at T = 450° C, a very small pressure rise of 0.25 PSIA occurred during the first 3000 seconds, presumably caused by water formation and desorption. This rise in pressure was followed by a drop of around 0.06 PSIA over the next 500 seconds. After this initial phase no pressure change was detected in reactions over an unannealed and unreduced powder or in an empty quartz tube. In the absence of the $npFe^0$ catalyst the experimental temperatures were apparently well below any activation threshold. No experiments were done with annealed, unreduced olivine, but CO and H_2 in the gas mixture should act to reduce the iron oxides produced during the annealing process, thus activating the catalytic

effect of $npFe^0$.

Figure 2.10 presents the measured pressure over elapsed time for an empty tube reaction at T = 450° C and a reaction over milled and sieved but unannealed powder at T = 450° C, along with the first 6×10^3 seconds of pressure data for the reaction over reduced powder at T = 400° C. Even at a temperature fifty degrees Celsius lower, reactions with the $npFe^0$-rich reduced powder yielded more significant changes in pressure.

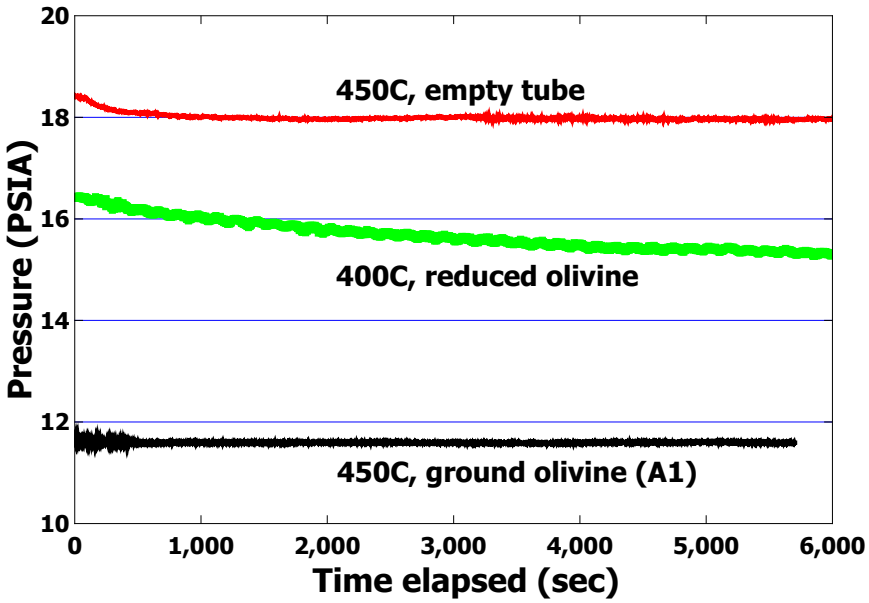

Figure 2.10: Pressure data for an equimolar mixture of carbon monoxide and hydrogen reacted in an empty tube (upper red line) and over an unannealed and non-reduced catalyst A1 (lower black line) at T = 450° C. Over this time period, the pressure was reduced by 1% to 3% for these two reactions, as compared to the reaction with the reduced catalyst (middle green line) in which the pressure was reduced by 7% over the same time period at a temperature fifty degrees lower (T = 400° C).

Both samples A4 and A5 appeared blackened after the reaction had completed. The overall reflectance change, presented earlier in Figure 2.2, suggests significant coking of the catalyst, which was further characterized with micro-Raman spectroscopy in Figures 2.11 and 2.12, and with

STEM and EELS in Figure 2.13.

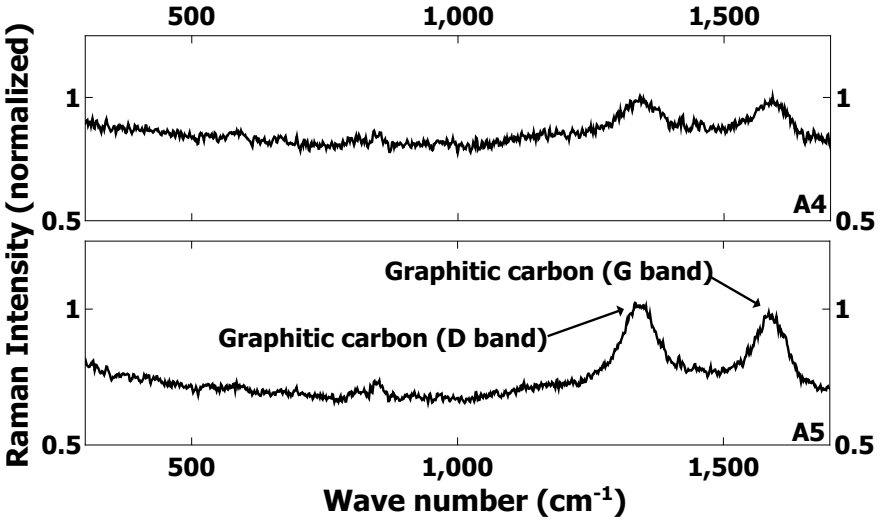

Figure 2.11: Micro-Raman spectroscopy analysis for coked post-carbon monoxide and hydrogen reacted samples A4 (T = 400° C for 138 hours), A5 (T = 450° C for 6.33 hours). Raman intensities have been normalized to 1350 cm^{-1}.

Figures 2.11 and 2.12 present Raman spectroscopic measurements of samples A4 and A5. In Figure 2.11, in both samples A4 and A5 we observe bands characteristic of disordered graphitic carbon at 1350 cm^{-1}, a disordered graphene band, and 1580 cm^{-1}, the graphene G band[89].[90] In Figure 2.12, in A4 and A5 a band characteristic of graphitic carbon is visible at 2690 cm^{-1} and is known as the graphene G' band[89].[90] Another somewhat prominent band is present at around 2900 cm^{-1} which is typically indicative of C-H bonds, but this band can also be a feature of damaged graphene[91].[90] When compared to the work of Dresselhaus,[90] the Raman spectra for samples A4 and A5 most closely resemble that of single-walled carbon nanohorns and defective graphene. However, given the presence of H_2 in our reactant gases, this damaged graphene is almost certainly terminated by hydrogen. Therefore the peak at 2900 cm^{-1} is in all likelihood a convolution of signals from both damaged graphene and C-H bonds.

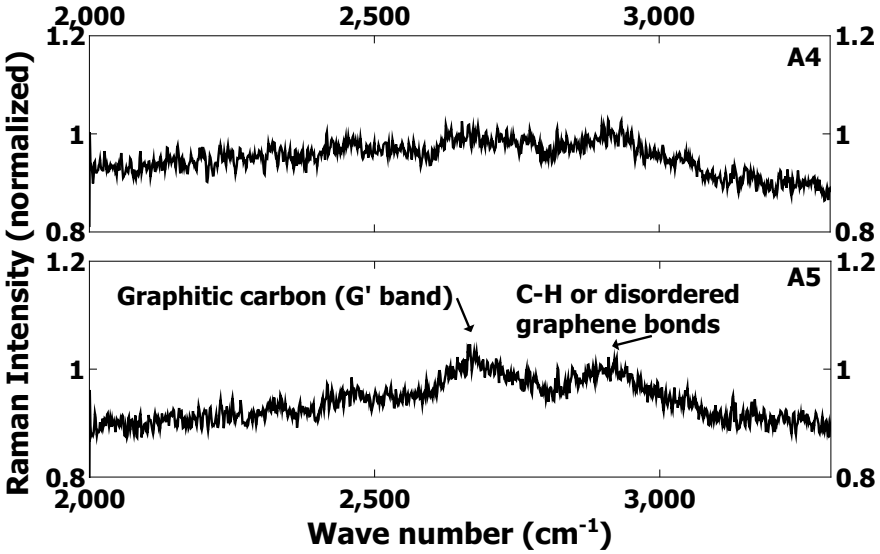

Figure 2.12: Micro-Raman spectroscopy analysis for coked post-carbon monoxide and hydrogen reacted samples A4 (T = 400° C for 138 hours) and A5 (T = 450° C for 6.33 hours). Raman intensities have been normalized to 2690 cm^{-1}.

The leftmost panel of Figure 2.13 shows a STEM image of an olivine grain with multiple bright spots and extended carbon structures jutting from the olivine. The inset square in the leftmost panel indicates the area which was analyzed with EELS, and measures 60 nm $\times$ 60 nm. The middle panel shows the analyzed area in HAADF mode, with each pixel measuring 2 nm $\times$ 2 nm. EELS data were extracted from this and used to create the elemental maps shown in the rightmost column of panels. In this furthest column of panels, EELS analysis of sample A4 is shown, using the energies of the 2p Fe and 1s C electronic states to map the spatial relationship of $npFe^0$ and C deposits. From this image, it is clear that significant C is deposited on the surface in the vicinity of $npFe^0$.

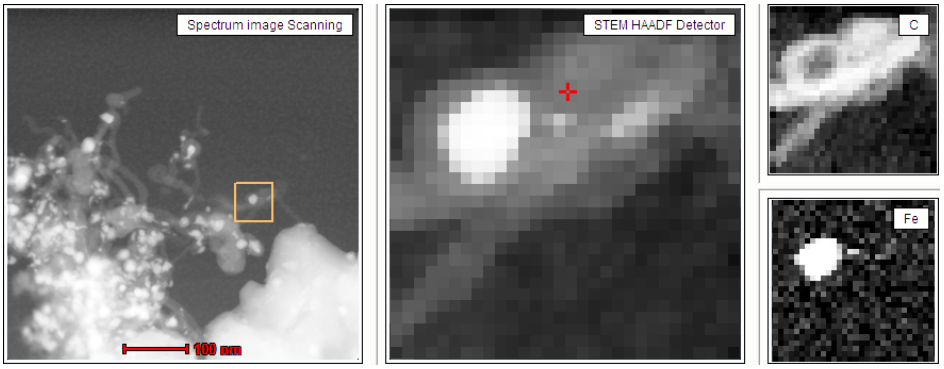

Figure 2.13: STEM analysis of sample A4 (reduced and reacted with equimolar carbon monoxide and hydrogen). The leftmost image shows the olivine grain with multiple bright spots and extended carbon structures jutting from the olivine. A scale bar is provided. The square indicates the area which was analyzed by EELS, and is 60 nm $\times$ 60 nm. The middle panel shows the analyzed area in HAADF mode, with each pixel being a 2 nm $\times$ 2 nm square. EELS data were extracted from this area and used to create the elemental maps shown in the rightmost column of images. The picture on the top right shows the distribution of 1s C, and the picture on the bottom right shows the distribution of 2p Fe. In this image, the brighter areas indicate the areas where more of these signals were detected.

The bright field TEM image presented as Figure 2.14 provides further insight into the role of $npFe^0$ and the nature of the carbon coking. In this figure, the dark areas correspond to $npFe^0$. Here, there is clear evidence that carbon "onions" (essentially graphitic carbon) had formed in the vicinity of the $npFe^0$. The space between fringes was measured to be $\sim$ 0.35 nm using fast Fourier transform (FFT) analysis. This distance is consistent with the spacing between individual graphene planes in graphite.[1]

In Figure 2.15, bright field TEM imaging of sample A4 was used to determine the lattice spacing of a nanoparticle and to verify that the dark areas were indeed metallic elemental Fe. A FFT was used to analyze the data in Figure 2.15, and it was found that the structure corresponds to a face-centered cubic (FCC) lattice. The observed spacing between lattice fringes of 0.6 nm corresponds to the [111] distance in FCC Fe [92]. It should be noted that due to destructive interference and the nature of refraction, only the spacing between identical layers produces an image.

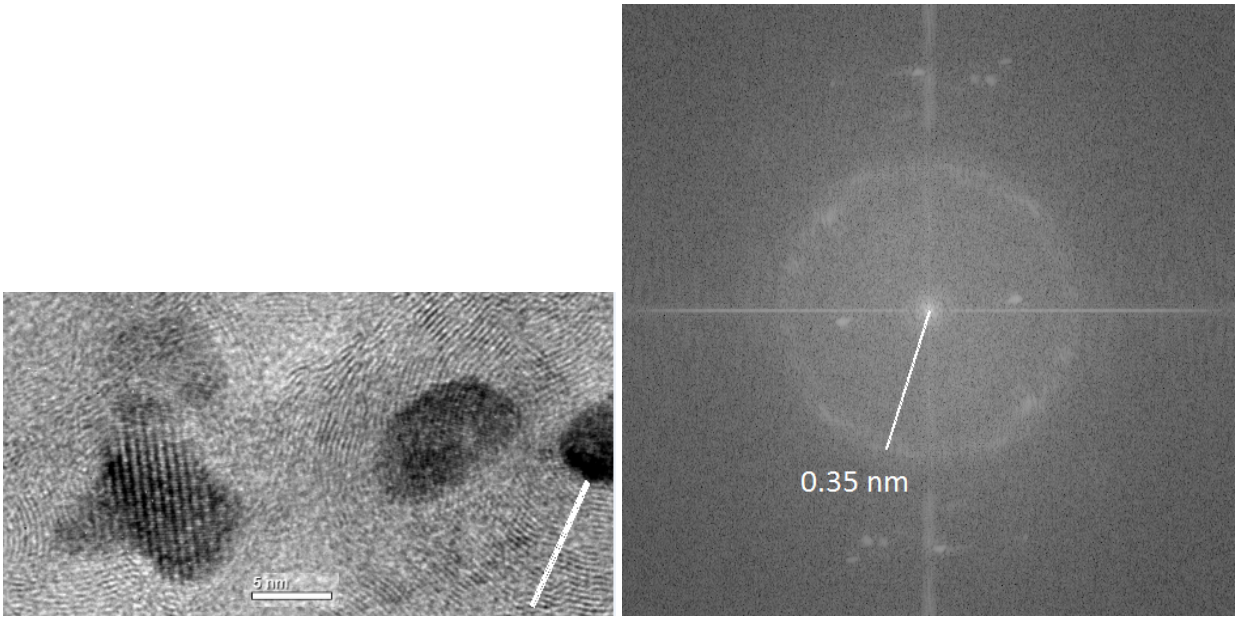

Figure 2.14: Bright field image of carbon onions from sample A4. In this image, the iron nanoparticles appear as dark spots. FFT analysis of the concentric circle structure around the rightmost iron nanoparticle (denoted by the white line) gives a spacing between layers of 0.35 nanometers, which agrees well with the spacing between graphene layers in graphite.[1]

At temperatures below approximately 1000 K the lowest energy state of metallic Fe is generally a body-centered cubic (BCC) lattice, however the FCC structure can become favorable at lower temperatures for very small nanoparticles with diameters less than approximately 11 nm.[92] This estimate is fairly rough, but the number is comparable to the diameter of the nanoparticle in Figure 2.15 which is about 18 nm in diameter. Carbon is known to be highly soluble in bulk FCC Fe, which is known as austenite or γ-Fe.[93]

Interestingly, TEM bright field images of sample A4 also show complex carbon structures growing on and around the iron nanoparticles, and indeed Feng et al. have observed the growth of carbon nanotubes catalyzed by the presence of npFe^0 when given a source of carbon-containing gas.[94] Some of these nanotubes can be seen in Figure 2.16.

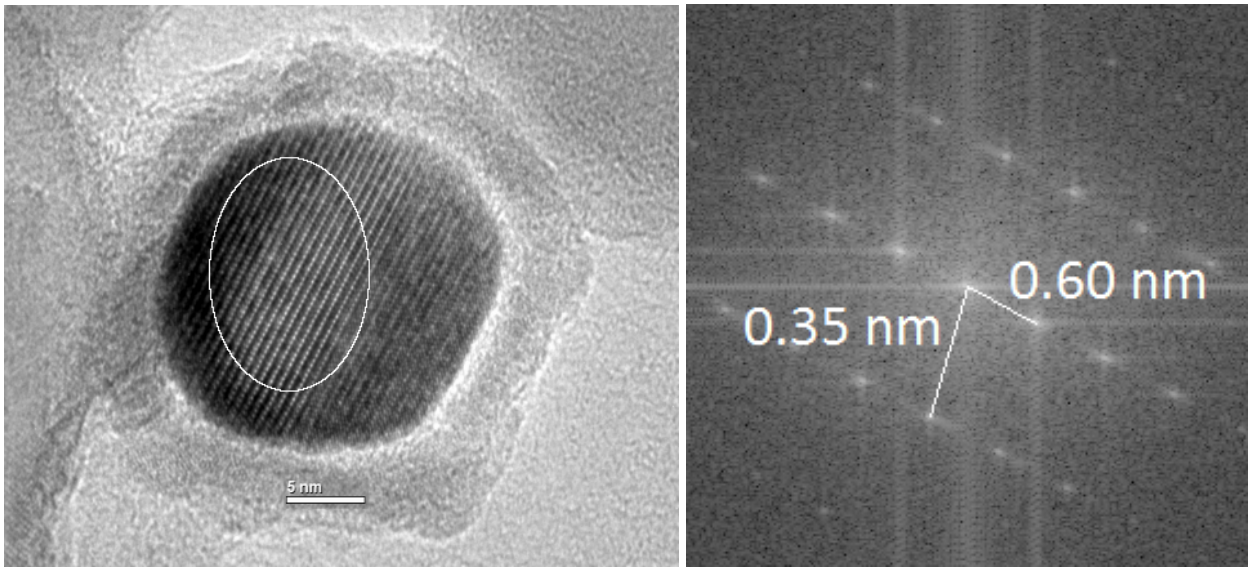

Figure 2.15: Bright field image of an iron nanoparticle from sample A4. In this image, the iron nanoparticle appears as a central dark spot. The area analyzed by FFT is denoted by a white oval. FFT analysis of the iron nanoparticle lattice structure indicates a layer spacing from the upper left to lower right of 0.60 nanometers, which corresponds to the distance between [111] A planes in FCC iron; spacing along one of these fringes (from the lower left to the upper right) is 0.35 nanometers, which corresponds to the distance between A planes in the [001] direction.

Discussion

Our analysis of the catalytic activity of reduced olivine is based on pressure changes recorded during our experiments. This analysis does not incorporate the possibility that the surface area of the reduced powders differed from the surface areas of the quartz tube or unannealed powders. If one assumes that all of the 20 mg of Fe in the fayalite fraction of the 250 mg of olivine formed spherical iron nanoparticles 15 nm in diameter, approximately 1.32×10^{15} iron nanoparticles were created with a total surface area of 0.93 m^2. However, in the previous section it was extrapolated that 0.043% of the sample is $npFe^0$ by weight. Using this more realistic estimate, only 0.11 mg of the available Fe has been converted to $npFe^0$. This would correspond to 7.1×10^{12} iron nanoparticles with a diameter of 15 nm, with a total surface area of 5.0×10^{-3} m^2.

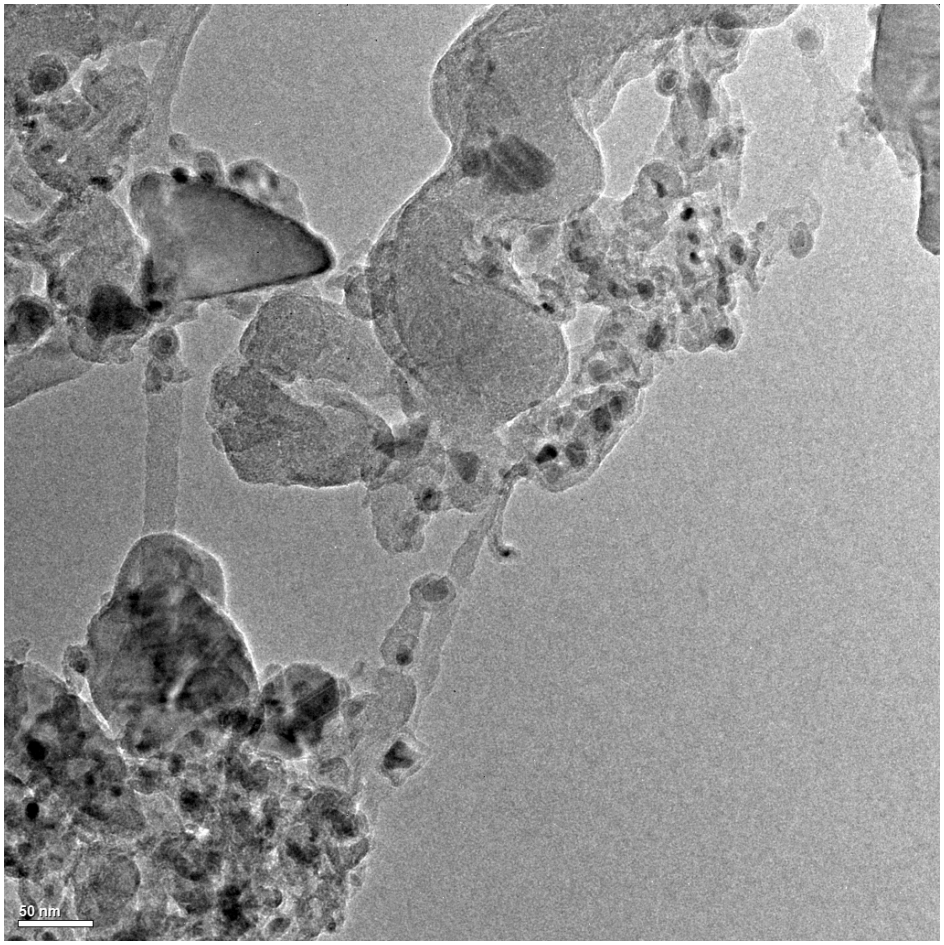

Figure 2.16: Bright field image of an iron nanoparticle from sample A4. In this image, the iron nanoparticle appears as a central dark spot. The area analyzed by FFT is denoted by a white oval. FFT analysis of the iron nanoparticle lattice structure indicates a layer spacing from the upper left to lower right of 0.60 nanometers, which corresponds to the distance between [111] A planes in FCC iron; spacing along one of these fringes (from the lower left to the upper right) is 0.35 nanometers, which corresponds to the distance between A planes in the [001] direction.

In comparison, 250 mg of unannealed olivine distributed among 40 μm diameter spheres has a surface area of around 11.3 $\times$ 10^{-3} m^2. If the empty quartz tube has a perfectly smooth surface, its inner surface area is approximately 8.47 $\times$ 10^{-3} m^2. The estimated surface area of the iron nanoparticles based on reflectance spectra is comparable to that of the tube or of the olivine grains. Additionally, these estimates require other assumptions that are somewhat questionable. Specifi-

cally, the assumption that the olivine grains are perfectly spherical is definitely not consistent with the TEM images, and hence the actual surface area might be much larger than the above estimate. Likewise, the inner wall of the quartz tube is most likely not perfectly atomically smooth. Overall, it is not clear which experiments had the largest surface area.

As mentioned previously, pressure changes alone are not a foolproof indicator of reaction progress, as reactions with equimolar products and reactants will produce no appreciable pressure change. In the case of reactions with NH_3, despite any issues with the Arrhenius fit prefactor which are related to the differing surface areas, we found lower activation energies which suggests an enhanced catalytic effect. In the case of reactions with CO and H_2, the analysis of the reacted powders exhibited the presence of solid carbonaceous species. There was also a visible difference in the powders after reaction with CO and H_2 depending on the initial state of the powder. Specifically, reduced powders were black after reaction, whereas the color of unannealed powders was unchanged by the reaction.

It should be noted that the method we have developed to generate npFe^0, namely via chemical means by processing olivine in a reducing H_2 gas, is not considered the principal way that npFe^0 is generated in the space environment. It is usually thought that npFe^0 is generated by ion sputtering or vaporization from a micrometeorite impact. When generated during a micrometeorite impact, npFe^0 may be encapsulated within a surface layer of amorphous materials, requiring breakage of this coating in order to expose the npFe^0 to potential reactants. Additionally, the spectrum for the npFe^0-containing reduced olivine sample in Figure 2.2 is quite dark, which indicates that the amount of npFe^0 produced in our experiments is possibly higher than concentrations typically found in the space environment, but this does not change the fact that samples containing npFe^0 exhibit increased catalytic activity when compared to samples without npFe^0. What we have shown is that npFe^0 can be generated by modest energy inputs and does not require the high temperatures necessary for silicate vaporization. The critical factor is the O_2 fugacity which is driven below the

iron-wustite buffer by the hard vacuum of space as well as the presence of solar wind implanted H. The presence of frozen volatiles on the surface represents a strong chemical non-equilibrium. Our increased volatile concentrations and temperatures allowed the process to be studied in a reasonable time frame. What drives chemical reactions at the surface are energy inputs from micrometeorite impacts or solar wind which is then facilitated by the presence of a catalyst. Furthermore, the catalytic activity of a surface should only depend on the morphology and composition of the space-weathered surface but not on the specific weathering mechanism which produced it. Therefore, it seems clear that npFe^0 produced by ion sputtering or micrometeorite impacts, or any other process, will lead to a strongly catalytically active surface as long as the catalysts are exposed on the surface. Additionally, the volatiles in our experiments were delivered as gases directly to exposed npFe^0. The ways in which this volatile delivery occurs naturally in the space environment is certainly far more complex and inconsistent. Volatiles which exist within a body in space must be delivered to the catalyst which processes them. Many mechanisms exist to deliver these volatiles. For example, out-gassing of CO or NH_3 could be caused locally by dust grain collisions or by other means, and rates of this out-gassing may vary wildly depending on the structure of the body in space and on the local thermal environment. Hydrogen may be delivered via solar wind or may evolve from the subsurface of a body.

The Fischer-Tropsch mechanism has been proposed previously by Anders[6] and by Hayatsu[95] as a path to generate complex organic species in the solar nebula. In his paper Anders describes the synthesis of many different organics, including amino acids and alkanes. One objection that has been raised towards FT mechanisms is that they are generally used in industry to produce linear and branched alkane molecules, but not polycyclic aromatic hydrocarbon species,[96] even in a planetary science context.[97] However, the results presented in this paper demonstrate that sp^2-bonded species can readily form at npFe^0 during surface mediated reactions; thus, one objection towards FT processes may be incorrect. In industrial FT reactions, while linear or branched alkanes are

often the desired products, coking is usually considered to be an undesirable but hard to avoid product that results in catalyst poisoning. The experience of the industrial applications is that the form of the reaction products depends on the pressure and temperature of the reaction. Industrial applications tightly control these parameters to achieve the desired products. On volatile-rich small bodies or in the solar nebula, the energy inputs are completely uncontrolled, resulting in a more diverse range of reaction products. In our experiments, while FT-type reactions possibly occurred, no direct evidence of hydrocarbon production was collected as we were unable to detect these products. We did, however, record evidence of surface mediated reactions producing large scale graphitic deposits. While industrial FT reactions might serve as a framework for understanding chemical processes on space-weathered mineral surfaces, this is certainly an incomplete picture for understanding what occurs in our experiments and also at the surface of real space-weathered minerals. For example, in our experiments, disproportionation Boudouard reactions of CO are also probably relevant. Moreover, in industrial FT processes, efforts are usually aimed at controlling reaction conditions to obtain desired reaction products, and coking reactions are always undesirable. By contrast, the chemical environments and mineral surfaces relevant for planetary science represent a much wider spectrum of surface-mediated reactions. Therefore, any reference to industrial reactions likely presents a somewhat limited view of the relevant reactions, and many key reactions on the surface of an asteroid or comet may in fact represent undesirable pathways in industry.

Conclusions

We have demonstrated that npFe^0 can be generated on the surfaces of olivine grains in a reducing environment with modest sub-solidus heating, and that olivine surfaces that include npFe^0 are strongly catalytically active. This indicates that space-weathered surfaces with characteristic npFe^0 can participate in chemical reactions when placed in a favorable environment, i.e., where

feed-stocks of reactants such as volatiles are available and there is an energy input to vaporize the volatiles and energize the reaction. The basic mechanism is that the $npFe^0$, and potentially other sites on the reduced surface, allow reaction intermediates to bind to the surface where they can readily break bonds and form new bonds. In the present study, starting with the simple molecules NH_3, H_2, and CO, $npFe^0$ facilitated the rearrangement of bonds. In the case of NH_3, a simple decomposition reaction occurred. By contrast, when CO and H_2 were allowed to react, an amorphous carbonaceous surface was observed to form, consistent with coking often seen in Fischer-Tropsch reactions.

It is important to recognize that although we have started with a mixture of simple molecules which can react to form complex products, it is also very likely that larger organic molecules and complex organic species might decompose more readily than at surfaces without $npFe^0$. These results suggest that the diversity and complexity of organic species may be a measure of the weathering maturity of space-weathered and volatile-rich surfaces.

Acknowledgements

This research was made possible by support from the the Center for Lunar and Asteroid Surface Science (CLASS), a NASA SSERVI node under NASA cooperative agreement NNA14AB05A, and the Florida Space Institute.

CHAPTER 3: DISSIPATION AND PLASTIC DEFORMATION IN COLLISIONS BETWEEN METALLIC NANOPARTICLES

Preamble

The following chapter will examine dissipation during collisions. Results are reported wherein the model material, the iron nanoparticle, is subjected to collisions and the end state analyzed to elucidate specific dissipative contributions and mechanisms. As a model material, iron represents an extreme in unpassivated mineral surfaces, and thus was chosen for the following study on dissipation. Here, it is demonstrated that at the nanoscale, high velocity collisions and thus plastic deformation may be inevitable.

NOTE : This chapter contains previously published content, which is used in accordance with the journal's copyright policy for usage in dissertations.

William C Tucker, Adrienne R Dove, and Patrick K Schelling. Dissipation and plastic deformation in collisions between metallic nanoparticles. *Computational Materials Science*, 161:215–222, 2019

https://doi.org/10.1016/j.commatsci.2019.02.004

Abstract

Collisions between amorphous Fe nanoparticles were studied using molecular-dynamics simulation. For head-on collisions of nanoparticles with radii $R = 1.4$ nm, $R = 5.2$ nm, and $R = 11$ nm, sticking was observed at all simulated velocities. The results were compared to the description

provided by the JKR model. It was found that strong disagreement exists between the predictions of JKR and the results of the molecular-dynamics simulation due to the presence of additional dissipative processes which strengthen sticking behavior. First, it is demonstrated that very strong dissipation into atomic vibrations occurs during the collision. The dissipation is strong enough to prevent significant rebound of the nanoparticles. Additionally, the morphology of the adhered nanoparticles includes a "neck" that increases in radius with increasing collision velocity which results in amplified irreversibility and adhesion. Approximate calculation of the stress during the collision indicates that stress levels are well above typical yield stress values even for low velocity collisions, consistent with the observation of plastic deformation. Furthermore, it is shown that for nanoparticles with $R \leq 11$ nm, the dominance of surface attraction results in large effective collision velocities and plastic deformation. By obtaining scaling relations for computed quantities, predictions are made for larger nanoparticles up to $R \sim 1$ μm. This work provides a new perspective on collisional dissipation and adhesion with an important connection to the modern understanding of tribology and friction.

Introduction

The collisional dynamics of nano- and micron-scale particles is often described theoretically using the continuum Johnson-Kendall-Roberts (JKR) theory, which describes adhesion between elastic spheres,[37] with the addition of dissipative processes. Various physical mechanisms have been proposed for dissipation, including elastic waves, viscoelastic dissipation, and dissipative mechanisms related to crack formation.[99–104] While JKR has typically been compared favorably with experimental results,[105–107] often the surface energy term is not well known and in some cases is fit to experimental results.[49,99] In addition, no experimental results have clearly demonstrated which dissipative mechanism provides the most suitable description.[49] Finally the JKR model is not able

to account for plastic deformation, which should become relevant especially at higher collision velocities.

Recently, atomic-scale simulation has been used to test some assumptions of the JKR model. In Nietiadi et al.,[108] molecular dynamics (MD) simulations of collisions between amorphous silica nanoparticles demonstrated strong deviations with the JKR model. Specifically, the critical bouncing velocity was established by simulations to be a factor 3.4 greater than predicted. Furthermore, only sticking was observed for nanoparticles with radii less than 15 nm. This enhanced sticking behavior appeared to be connected to the presence of a larger contact area due to strong plastic deformation, including the generation of filaments, between the nanoparticles. In agreement with these results, it was shown in Quadery et al.[41] that using MD collisions of silica nanoparticles, the lack of adsorbed OH groups results in strong covalent bonds, with no clear bouncing threshold. However, in Quadery et al.,[41] only small nanoparticles with radii 2 nm and below were simulated. Nevertheless, existing simulation results suggest strong deviations from JKR model predictions at least for very small nanoparticles.

The adhesive behavior of powders in turbulent flows is of industrial and theoretical interest as can be seen by the wide range of current research and review articles.[109–111] Most of these models utilize the JKR model of contact mechanics in some form. While Fe nanoparticles might not typically be a material considered for simulating collision dynamics, metallic nanoparticles, and specifically iron nanoparticles, are of interest due to their enhanced catalytic activity, which has been demonstrated for industrial processes[5,65–67] and in the context of promoting chemical reactions of astrophysical interest.[53] Iron nanoparticles can even be used to assist in environmental cleanup efforts.[112] Metallic Fe nanoparticles represent a simple system and are a kind of extreme case where due to dangling bonds at the surface one might expect particularly strong dissipation and adhesion, and thus it represents a sort of “limiting case” in collision dynamics which would be interesting to understand. Velocities were chosen to span a range of regimes but with a special

focus on lower velocity collisions from 10 to 500 m s^{-1} which are relevant in the astrophysical context of protoplanetary dust cloud dynamics. For example, in astrophysics, additional dissipative mechanisms and enhanced adhesion could be helpful in surmounting the so-called millimeter bouncing barrier,[25] whereas in a catalytic context the sintering of nanoparticles and consequent loss of surface area leads to a significant drop in effectiveness. Thus, we hope to offer suggestions towards the development of more physically relevant models of adhesion and dissipation for a range of interaction environments.

In the next section, the basic assumptions of the JKR model applied to nanoparticle collisions with various models of dissipation are briefly described. Next, the atomic-scale simulation methodology used in this paper is presented, followed by a section describing the results of extensive simulations. In the discussion section we attempt to determine scaling relations for relevant physical quantities that can potentially yield predictions for significantly larger length scales, including up to 1 μm particles. Finally, in the conclusion we tie these results back to potentially relevant applications, including planetary formation, other mineral systems, and previous findings in the field of tribology, including potential relationships to the modern understanding of Amonton's laws of friction.

JKR Theory and Treatment of Dissipation

In the JKR theory,[37] the energy associated with adhesion between two identical spheres of radius R with reduced radius $R^* = \frac{R}{2}$ depends on the interfacial energy and the elastic strain energy. The interfacial energy U_S depends on the surface energy γ and contact radius a,

$$U_S = -2\pi a^2 \gamma, \tag{3.1}$$

while the elastic strain energy U_E is given by

$$U_E = \frac{E^* a^3}{3R^*}\left[\delta\left(\frac{3\delta R^*}{a^2} - 1\right) - \frac{a^2}{5R^*}\left(\frac{5\delta R^*}{a^2} - 3\right)\right]. \tag{3.2}$$

For two identical spheres, the combined elastic modulus E^* is defined by

$$E^* = \frac{E}{2(1-\nu)^2}, \tag{3.3}$$

where E is the Young's modulus and ν is the Poisson ratio of the material in bulk. The quantity δ is the length associated with compression of the two spheres in contact. Specifically, for two identical spherical objects with radius R whose center-of-mass coordinates are separated by a distance d, the compression is given by

$$\delta = 2R - d. \tag{3.4}$$

For a particular compression δ, JKR theory predicts that the system will optimize the contact radius a to minimize the total energy $U_{JKR} = U_S + U_E$, resulting in a relationship between the compression δ and contact radius a,

$$\delta = \frac{a^2}{R^*} - 2\sqrt{\frac{\pi\gamma a}{E^*}}. \tag{3.5}$$

With this assumption, the JKR theory results in a force

$$F_{JKR} = \frac{4E^* a^3}{3R^*} - 4\sqrt{\pi\gamma E^* a^3}. \tag{3.6}$$

The point where F_{JKR} vanishes yields the equilibrium contact radius and length of compression,

$$a_{eq} = \left(\frac{9\pi\gamma R^{*2}}{E^*}\right)^{1/3}, \tag{3.7}$$

$$\delta_{eq} = \left(\frac{3\pi^2\gamma^2 R^*}{E^{*2}}\right)^{1/3}. \tag{3.8}$$

As can be seen in the above expressions, the JKR theory applied to collisions predicts that equilibrium is attained with a contact area and compression (and thus an adhesive energy) that are independent of the collision velocity. These assumptions are not valid if significant plastic deformation occurs.

In order for adhesion to occur, complete dissipation of the incident kinetic energy is required. Dissipation always involves generation of internal thermal energy, while for large enough collision velocities, plastic deformation, generation of coordination defects, and melting can occur. Several attempts have been made to add dissipation to existing JKR-based adhesion models. For example, in Krijt at al.,[99] models of viscoelastic growth of cracks, bulk viscoelastic dissipation, and plastic deformation were used to describe dissipation. The resulting model provides theoretical predictions for the coefficient of restitution and the sticking velocity. In Chokshi et al.,[104] dissipation into elastic waves was used to describe dissipation, with the critical sticking velocity predicted from the requirement that the energy dissipation in elastic deformations be greater than the energy required to separate the nanoparticles. However, while many models for dissipation exist, no results have been reported which validate any particular dissipation model.

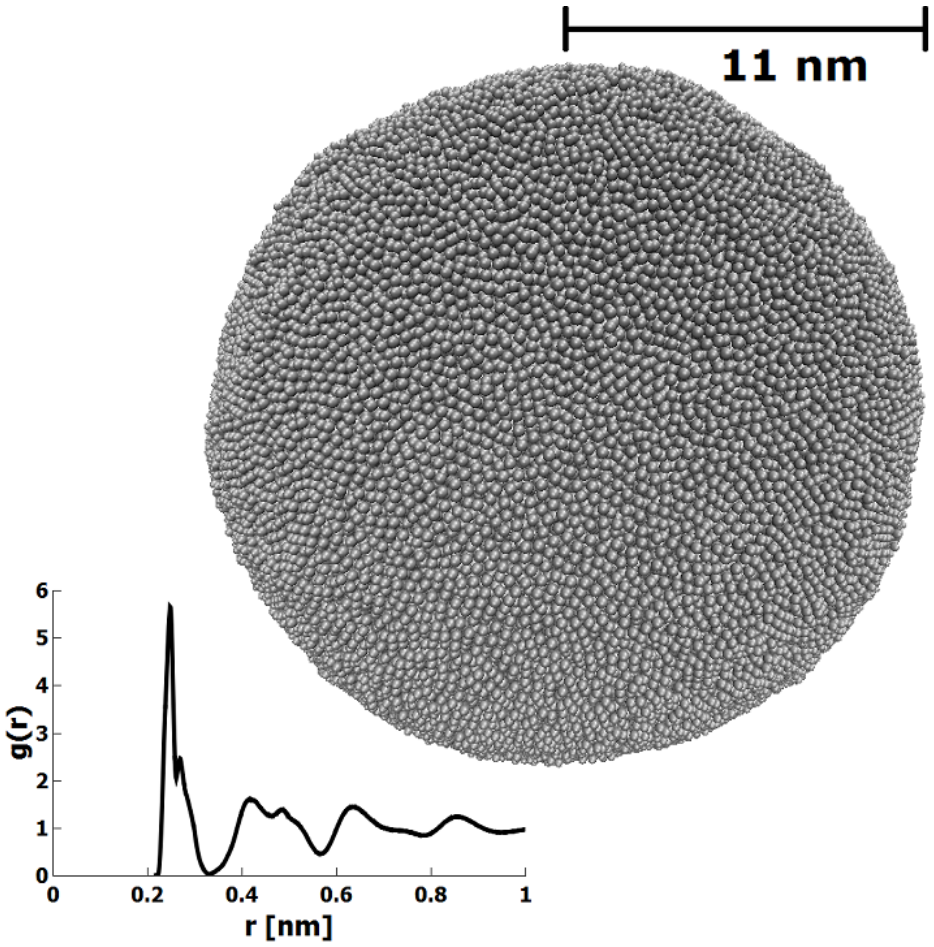

Figure 3.1: Top right: Atomic structure of the large amorphous Fe nanoparticle with approximate radius $R = 11$ nm and $N = 470561$ atoms. Bottom left: Radial distribution function of the depicted nanoparticle.

Molecular-Dynamics Simulation Approach

In the present article, the detailed atomic-scale mechanisms for dissipation are described using molecular dynamics (MD) simulation. This approach includes all length scales for dissipation, including vibrational modes with wavelengths comparable to the separation between the atoms. The advantage of this approach is that there is no requirement for a physical model with assumptions, but rather all atomic degrees of freedom are explicitly described.

The LAMMPS simulation code[113] with the embedded-atom method (EAM) potential for Fe from Mendelev et al. (potential 2)[114] was used. Visual renders of atomic structures were produced using the Visual Molecular Dynamics (VMD) software package.[115] The simulations were performed with an MD time step of 0.25 fs, small enough to ensure energy conservation, and much smaller than the timescale of the highest inter-atomic vibrational frequency in the system. Three sizes of amorphous nanoparticles were generated: a small nanoparticle with N = 1024 atoms and radius R = 1.4 nm, a medium nanoparticle with N = 50286 atoms and radius R = 5.2 nm, and a large nanoparticle with N = 470561 atoms and radius R = 11 nm. The Fe nanoparticles were melted in a constant temperature ensemble by increasing the temperature to T = 2200 K. This was followed by a slow anneal to T = 5 K. Melting was performed over 100 ps for the small nanoparticle, 120 ps for the medium nanoparticle, and 240 ps for the large nanoparticle. Annealing times were identical to melting times. In the top right of Figure 3.1, the atomic structure of the large amorphous Fe nanoparticle is depicted. After the annealing process was complete, the Fe-Fe radial distribution function (RDF) was calculated to ensure that the nanoparticles were amorphous. The RDF of the large nanoparticle is depicted in the bottom left of Figure 3.1. From the RDF data, the coordination number was determined by integration to the first minimum of the RDF at 0.33 nm. The calculated Fe-Fe coordination number of 13.2 is somewhat higher than for an FCC crystal due to the fact that the first minimum in the RDF is significantly greater than the Fe-Fe bond lengths $\sim$ 0.25 nm in either BCC or FCC iron.

The radii of the nanoparticles were determined first by computation of the $T = 0$ K density of bulk amorphous Fe, and then assuming a spherical shape for the nanoparticles. For a nanoparticle with mass m and mass density ρ, the radius is defined by

$$R = \left(\frac{3m}{4\pi\rho}\right)^{1/3}. \tag{3.9}$$

Using this expression, with the computed mass density $\rho = 7.82$ g cm^{-3} for amorphous Fe, the small nanoparticle with $N = 1024$ corresponds to a radius $R = 1.4$ nm. For the medium nanoparticle with $N = 50286$, the radius is $R = 5.2$ nm. Finally, for the large nanoparticle with $N = 470561$ we obtained the radius $R = 11$ nm. Given the radii of the nanoparticles, the surface energy γ was determined using the computed energy of the nanoparticles and that of the bulk amorphous Fe solid. In each case, the surface energy was computed to be nearly $\gamma = 0.09$ eV A^{-2}, indicating that there was no size-dependence to the surface energy.

Collisions between same-sized nanoparticles with relative velocities between 10 m s^{-1} and 3000 m s^{-1} were simulated. These velocities were chosen to span the entire range from moderately slow collisions up through collisions with enough kinetic energy to ensure a liquid final state. We cast a special focus on lower velocity collisions up to 500 m s^{-1}, as these velocities were found to result in minimal large-scale plastic deformation of the nanoparticle structure away from the inter-particle contact. For each relative velocity, multiple collisions were simulated for different random rotations of the two nanoparticles. For the small and medium nanoparticles, 30 simulations were performed at each velocity. For the large nanoparticle, 3 simulations were performed at each velocity. After relaxation, both nanoparticles were given a desired translational velocity which resulted in a head-on collision. Simulations were continued for at least 50 ps after the collision until equilibrium was achieved. The center-of-mass coordinates of the two nanoparticles were monitored to determine whether the nanoparticles adhered together. For each simulated nanoparticle size and incident velocity only sticking was observed, with no incidents of bouncing behavior.

To compute the work of adhesion W_{adh} from the results of the irreversible collision simulations, the approach first described in Quadery et al.[41] was used. The basic assumption is that nanoparticle collisions result in a change in potential energy and thermal excitation. If the system remains in a solid state, it is reasonable to assume that the thermal energy can be described using the equipartition theorem applied to a system of harmonic oscillators. The work of adhesion W_{adh} was

therefore computed according to,

$$W_{adh} = 3N_{tot}k_B(T_f - T_i) - K_{trans}, \tag{3.10}$$

where $N_{tot} = 2N$ is the total number of atoms in the simulation, T_f and T_i are the computed temperatures before and after the collision, and K_{trans} is the translational kinetic energy before the collision. In determining T_f and T_i, the kinetic energy in the center-of-mass reference frame of each nanoparticle was used. The physical meaning of W_{adh} is that it approximately corresponds to the work required at $T = 0$ K to adiabatically separate the nanoparticles by breaking bonds at the interface. While the interpretation of W_{adh} is clear when adhesion occurs with minimal disruption of the surfaces, in instances with large plastic deformation or melting of the nanoparticles, significant amounts of energy can be stored in disruption of the atomic structure, and the concept of adiabatically separating the nanoparticles after the collision is somewhat ill-defined. Nevertheless, W_{adh} is calculated using Eq. 3.10 for all collisions including those where the physical interpretation is more complicated.

Results

Each simulated head-on collision resulted in sticking. Fragmentation was not observed at any of the simulated velocities or radii. For very large velocities, full melting was observed: for v_{rel} = 2750 m s^{-1}, T_f was around 1900 K, and for v_{rel} = 3000 m s^{-1}, T_f was around 2200 K, comparable to the solid to fully liquid transition temperature $T_{liq} \sim 1900$ K of a single R = 1.4 nm nanoparticle melted in an ancillary MD simulation. Consequently, there is no velocity range where bouncing of solid nanoparticles occurs, although at very large velocities either vaporization or splashing will occur. It may be that bouncing events are not impossible, but that they are at least extremely

rare. This is in significant contrast to previous results for SiO_2 nanoparticles in Quadery et al.[41] where significant instances of bouncing were observed. Bouncing might also occur for very large nanoparticle sizes or when collisions are not exactly head-on.

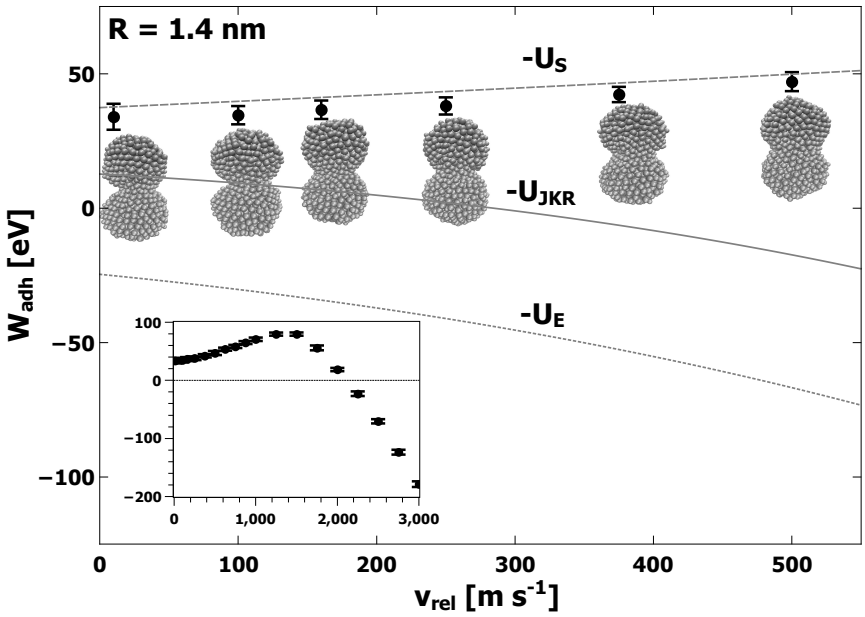

Figure 3.2: Computed values of W_{adh} for nanoparticles with R = 1.4 nm plotted as a function of relative collision velocity. For each simulated collision velocity, a visualization of a typical structure is also included. Lines indicate predictions for JKR elastic energy U_E (negative of Eq. 3.2, short dashed line), surface energy U_S (negative of Eq. 3.1, long dashed line), and total energy U_{JKR} (sum of the negative of surface and elastic contributions, solid line). The inset plots values of W_{adh} for higher velocities. Units of the inset are identical to units of the main plot, and the inset does not include JKR predictions to reduce visual clutter.

In Figures 3.2, 3.3, and 3.4, we show the computed average values of W_{adh} as a function of collision velocity v_{rel} for lower velocities, with an inset showing the data for all velocities. The error bars represent the standard deviations obtained from all simulations performed at each value of v_{rel}. Along with the computed values, an image of a typical atomic structure for the adhered nanoparticles is shown for each collision velocity. Each structure depicted represents the final structure attained after equilibration. Predictions made by JKR for elastic, surface, and total energies are

denoted by lines on Figures 3.2, 3.3, and 3.4,. Comparison to JKR theory will be presented in the next section.

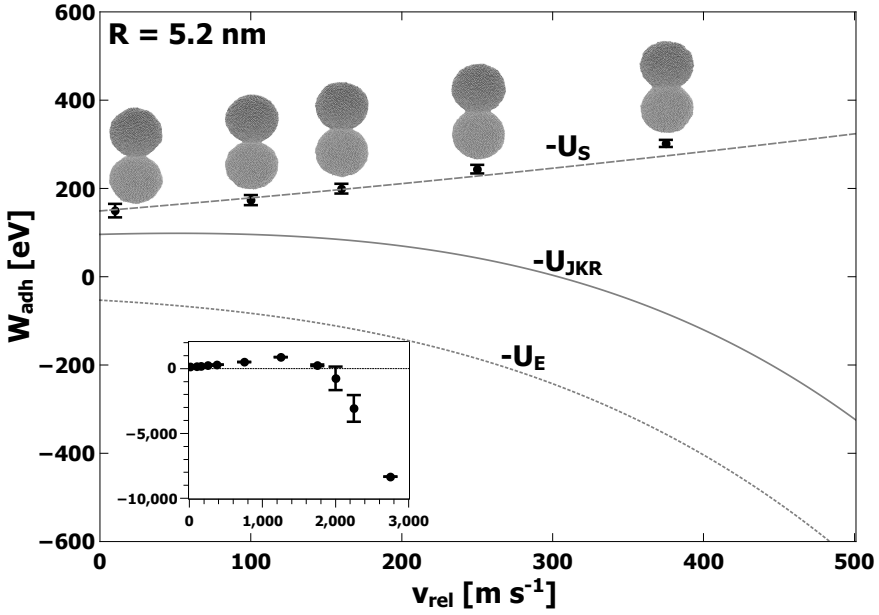

Figure 3.3: Computed values of W_{adh} for nanoparticles with R = 5.2 nm plotted as a function of relative collision velocity. For each simulated collision velocity, a visualization of a typical structure is also included. The lines and inset are described in the caption of Figure 3.2.

From the data plotted in Figures 3.2, 3.3, and 3.4, several consistent trends emerge which are independent of either the model or the size of the nanoparticle. First, the computed value of W_{adh} increases gradually with increasing collision velocity for values of v_{rel} up to at least 1000 m s^{-1}. Corresponding to these cases, the structures in Figures 3.2, 3.3, and 3.4, show an apparent contact area which increases with v_{rel}. For larger values of v_{rel} (i.e. significantly past 1000 m s^{-1}), the computed W_{adh} begins to decrease and eventually becomes negative. In this regime, the atomic structure appears less like two adhered nanoparticles and progressively more like a single deformed nanoparticle, generally elliptical in shape, eventually becoming spherical at the highest simulated values of v_{rel}. Based on calculations of the self-diffusion coefficient, values of v_{rel} above about

2000 m s^{-1} were in a liquid state when fused into a spherical shape. For the largest nanoparticles with radius $R = 11$ nm, only velocities $v_{rel} = 250$ m s^{-1} and below were simulated, and the increase in W_{adh} with v_{rel} is apparent but less dramatic. The simulations for the large nanoparticles with $R = 11$ nm did not extend into the regime where large deformation and melting occurs due to the extensive computational resources required.

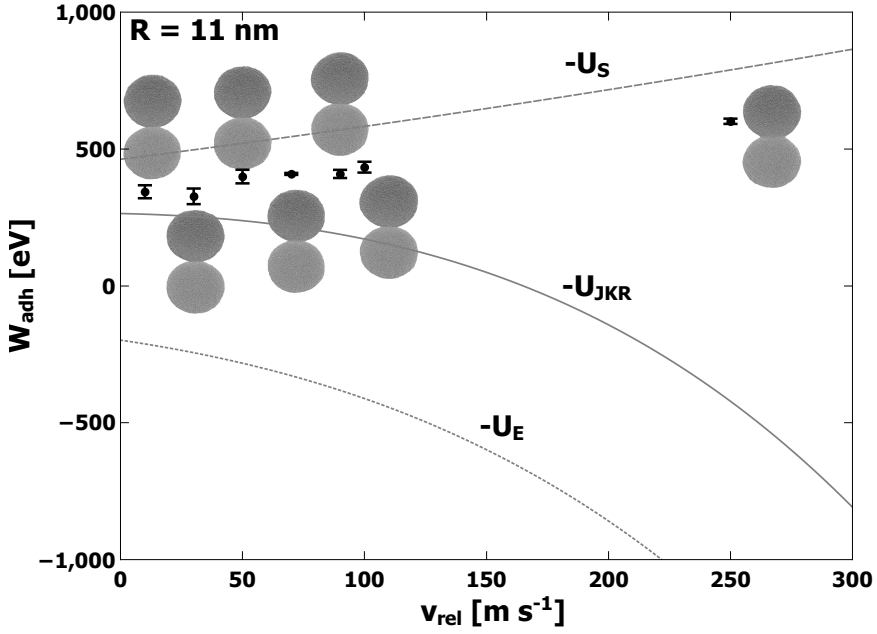

Figure 3.4: Computed values of W_{adh} for nanoparticles with R = 11 nm plotted as a function of relative collision velocity. For each simulated collision velocity, a visualization of a typical structure is also included. The lines are described in the caption of Figure 3.2. Simulations for this size nanoparticle did not extend into higher velocities due to the extensive computational resources required.

The general trends can be understood in a simple way. The changing nature of the contact area is indicative of significant plastic deformation. Specifically, at lower velocities (i.e. below $\sim$ 1000 m s^{-1}) the gradual increase in W_{adh} with increasing v_{rel} is due to plastic deformation which allows for greater contact between the two surfaces. Although this could occur by elastic deformation, it is important to note that elastic deformation would also involve significant elastic strain energy

(see analysis in next section for further discussion). At higher velocities (above $\sim$ 1000 m s^{-1}), the decrease in W_{adh} is due to the complete fusing of the two nanoparticles along with the generation of significant numbers of coordination defects, and possibly strain energy. The coordination defects correspond to stored energy, and thus result in negative contributions to W_{adh}. In these instances, separation of the two nanoparticles would result in nanoparticles with markedly different structures than before the collision. Nevertheless, W_{adh} is a measure of the internal potential energy of the system with respect to the isolated nanoparticles before the collision. Finally, at the highest simulated values of v_{rel}, the change in internal energy is large enough to result in a phase transition to the liquid state along with very large negative values of W_{adh}.

If elastic strain energy and energy associated with coordination defects are neglected, it is possible to use the computed values of W_{adh} to establish an effective contact area

$$A_{eff} = \frac{W_{adh}}{2\gamma}. \tag{3.11}$$

As in Quadery et al.,[41] we also compare this effective contact area to the cross-sectional area via

$$\eta = \frac{A_{eff}}{\pi R^2}. \tag{3.12}$$

The unit-less parameter η captures both the relative area of the interface as well as the quality of the bonding. Specifically, values of $\eta \approx 1$ imply a perfectly-coordinated interface with both nanoparticles deformed such that the interfacial area corresponds to the entire cross-sectional area. By contrast, values of η that approach 0 imply a weakly bonded interface, either with a small contact area or a significant number of defects. Generally, it is expected that η will have a value intermediate to these extremes. From the data plotted in Figure 3.5, at v_{rel} = 10 m s^{-1}, the value of $\eta = 0.29$ for $R =$ 1.4 nm nanoparticles indicates a substantial contact area at the interface

between the nanoparticles even at the lowest values of v_{rel}. For larger nanoparticles, the values of η are significantly smaller, yet still are indicative of substantial contact and strong bonding. Additionally, the final compression length δ was directly determined from the MD simulations and Eq. 3.4. In Figure 3.6 δ is plotted as a function of v_{rel} for each radius R. It is clear that δ increases strongly with increasing v_{rel}. This observation is consistent with plastic deformation.

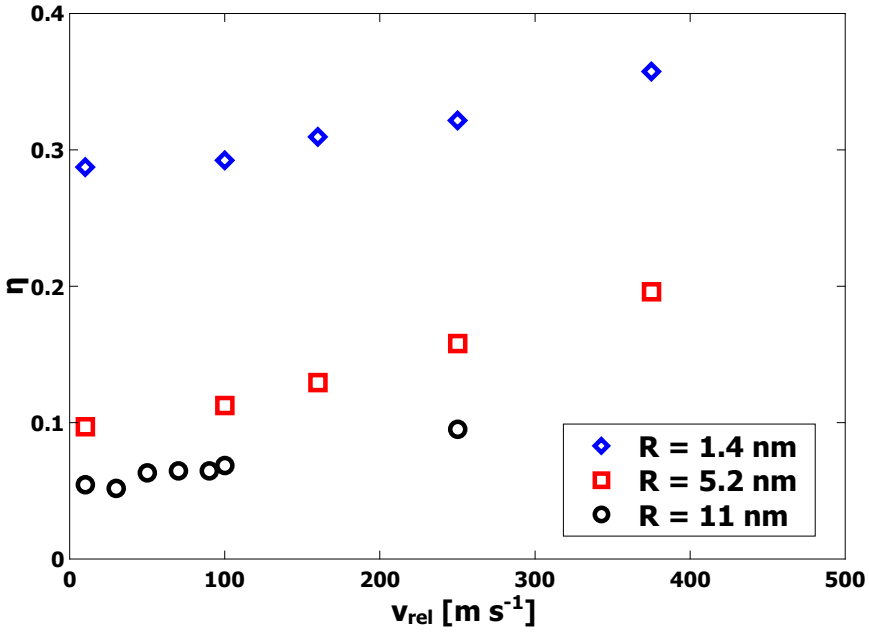

Figure 3.5: Computed values of η for relative collision velocities up to 500 m s^{-1} for all three sizes of nanoparticles plotted as a function of relative collision velocity. Blue diamonds represent data for R = 1.4 nm, red squares represent data for R = 5.2 nm, and black circles represent data for R = 11 nm.

To establish the dissipation mechanism, we will now focus on the low-velocity collisions. In all collisions, the center-of-mass coordinates of each nanoparticle were retained as a function of time, allowing for determination of the acceleration and hence net force during the collision. In Figure 3.7, the velocity and acceleration of both nanoparticles are plotted as a function of time for one simulated collision of two R = 1.4 nm nanoparticles with v_{rel} = 100 m s^{-1}. The collision just after 20 ps is evident; the spike is an artifact of how the initial translational velocity was imparted. Due

to the strong attraction, the nanoparticles initially accelerate towards each other once they enter the interaction range determined by the cutoff of the EAM potential. After significant compression, the acceleration changes sign and the velocities slow. However, before the velocities change sign for the rebound, the forces already have begun to decrease. If this were an elastic deformation, any increased compression of the two particles would lead to increased force as more elastic energy is stored. The point where the velocities change sign corresponds to the rebound phase. However, during the rebound phase, the magnitude of the acceleration is dramatically decreased from the compression phase, and consequently the rebound velocities are quite small. These observations clearly show that dissipation is correlated with strong plastic deformation, and in fact the plastic deformation itself represents the primary dissipation mechanism.

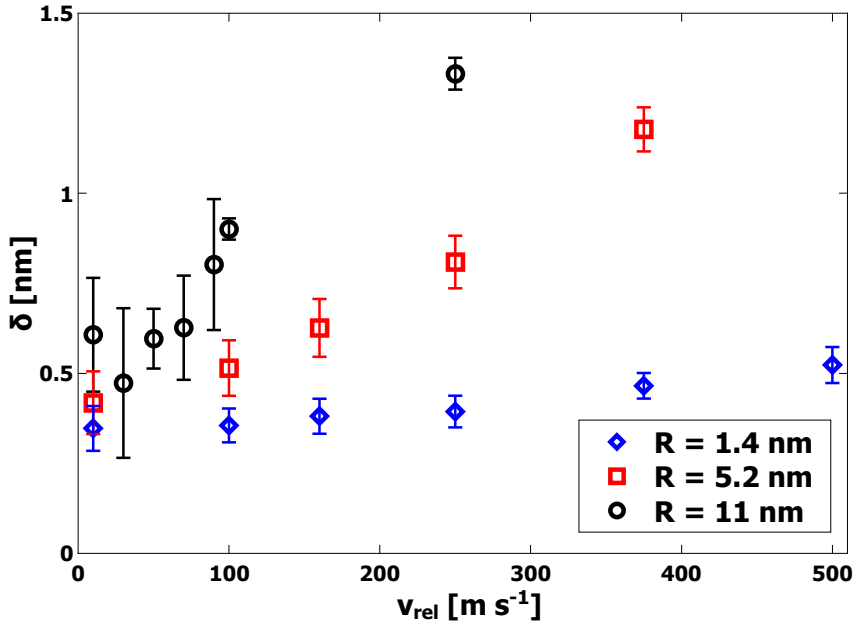

Figure 3.6: Computed values of the compression length δ for relative collision velocities up to 500 m s^{-1} for all three sizes of nanoparticles plotted as a function of relative collision velocity. Blue diamonds represent data for R = 1.4 nm, red squares represent data for R = 5.2 nm, and black circles represent data for R = 11 nm. JKR theory predicts values of δ_{eq} = 0.23 nm, 0.35 nm, and 0.43 nm for the small, medium, and large nanoparticles, respectively.

Table 3.1: Oscillation periods τ and damping times τ_d for v_{rel} = 10 m s^{-1} as a function of nanoparticle radius R

R (nm)	τ (ps)	τ_d (ps)
1.4	3.7	0.7
5.2	18.0	4.6
11.0	45.0	27.0

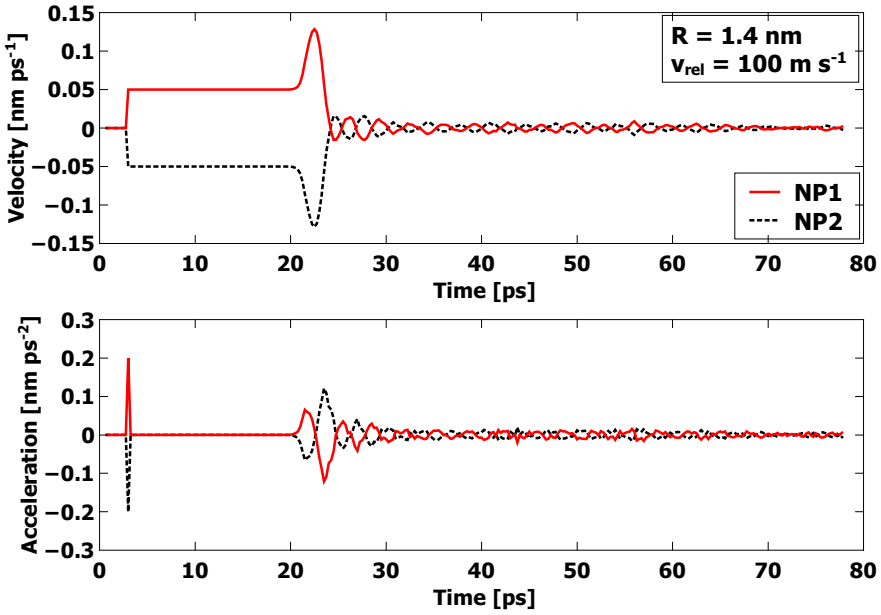

Figure 3.7: Velocities and accelerations of both nanoparticles plotted as a function of time for the R = 1.4 nm nanoparticle collision with v_{rel} = 100 m s^{-1}. Solid red lines denote data for the first of two nanoparticles, and dashed black lines denote data for the second. Phases and behaviors are described in the main text.

After the initial deformation and rebound phase, the subsequent behavior of the center-of-mass coordinates is consistent with that of an under-damped simple-harmonic oscillator. The results for the center-of-mass velocity (e.g. Figure 3.7) were used to establish the oscillation period τ for collisions with v_{rel} = 10 m s^{-1}. As expected, the period increases with increasing radius R. In Figure 3.8, the kinetic energy in the oscillations of two nanoparticles of mass m and center-of-mass

velocity v_{CM}, $K_{CM} = m\, v_{CM}^2$, is normalized by the energy to be dissipated and plotted as a function of time again for v_{rel} = 10 m s^{-1} collisions. It is evident from Figure 3.8 that the energy of the vibrational motion of the particles is very strongly damped. Exponential decay function fits were performed to determine the damping time τ_d. In Table 3.1, the values of τ and τ_d are given for each radius R for v_{rel} = 10 m s^{-1} collisions. For the particles to bounce, the requirement would be that $\tau_d >> \tau$, so that most of the incident energy is available during the rebound phase. In each case, τ is significantly greater than τ_d, demonstrating very strong damping; however, it is evident that τ_d is increasing with R faster than τ, indicating the potential for bouncing at large enough R values. In the next section, this condition will be explored to determine when bouncing might be expected to occur.

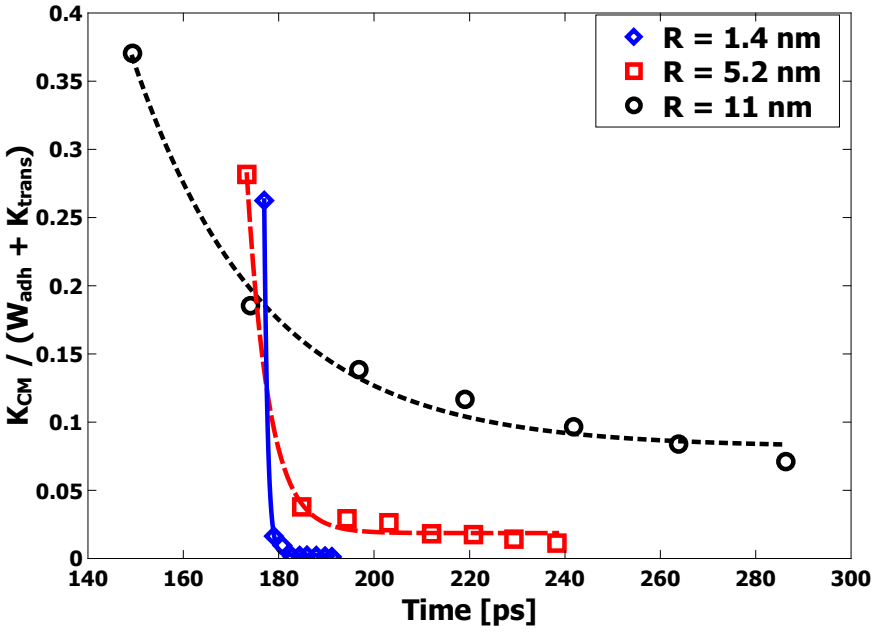

Figure 3.8: Center-of-mass kinetic energy normalized by the energy to be dissipated plotted as a function of time for all three nanoparticle sizes when v_{rel} = 10 m s^{-1}. Blue diamonds represent data for R = 1.4 nm (solid blue line is a fit to exponential decay), red squares represent data for R = 5.2 nm (long dashed red line for fit), and black circles represent data for R = 11 nm (short dashed black line for fit). For R = 11 nm, the decay time was 27 ps. For R = 5.2 nm, the decay time was 4.6 ps. For R = 1.4 nm, the decay time was 0.7 ps.

The stresses at the interface can be estimated from the computed forces as well as a reasonable estimate of the contact area. Using the values of η shown in Figure 3.5 as an estimate of the contact area, the stresses during the collision, both tensile and compressive, are in the range of $3-10$ GPa in magnitude. This is significantly greater than the yield stress for bulk Fe of 80-100 MPa.[116] While yield stresses of nanoparticles can be somewhat larger than for bulk materials the differences are generally fairly small. For example, in Hawa et. al,[117] simulations were used to compute the yield stresses for Ag nanoparticles, with yield stresses in the range 0.5-0.7 GPa for crystalline nanoparticles with $R \sim 5-10$ nm, and somewhat lower yield stresses for amorphous nanoparticles. Therefore, even taking into account the higher yield stresses typically exhibited by nanoparticles, the stresses exerted upon Fe nanoparticles in the simulation are large enough to result in plastic deformation. In Chokshi et al., the authors briefly discuss the sizes below which plastic deformation should be relevant for dissipation.[104] Following their arguments, for the currently presented simulations plastic deformation should only be important for sizes smaller than roughly R $\sim$ 1.3 nm, which is significantly smaller than the R = 11 nm particles reported here. However, it is also clear that more accurate calculations of stress would be worthwhile, including a calculation of the stress gradients in the vicinity of the contact region.

Discussion and Analysis

The results presented above demonstrate some important features. Specifically, at least in the case of particles of $R \leq 11$ nm, plastic deformation and extremely strong dissipation occurs in a manner not consistent with the JKR theory. Though much of the interest in particle interaction dynamics lies in larger particles of at least $R \sim 1\mu$m and beyond, where direct MD simulations are not possible, some behaviors can be predicted based on how various quantities scale with R. In this section we first strengthen the understanding of how JKR fails at nanometer length scales,

and then explore how the results scale with radius R to determine how MD predictions can be used to develop theoretical understanding at larger length scales, including where JKR likely has more validity.

In the JKR model, elastic strain accommodates an increase in the contact area. In addition, it predicts that the final contact area does not depend on the collision velocity v_{rel} and that above a certain velocity, the initial translational kinetic energy is too great to cause adhesion. In order to elucidate which contributions to $U_{JKR} = U_S + U_E$ were most important in determining the value of W_{adh} calculated as per Eq. 3.10, we used the directly computed values of δ to numerically solve Eq. 3.5 and to get an expression for contact radius a as a function of v_{rel}. These contact radii were then used in Eqs. 3.1 and 3.2 to obtain values for the contributions to U_{JKR}. These are plotted on Figures 3.2, 3.3, and 3.4, for comparison to the MD simulation results for W_{adh}. Clearly, the surface energy contribution accounts very well for the values for W_{adh} for velocities up to $v_{rel} = 500$ m s^{-1}. Figure 3.6 shows that δ increases with v_{rel}, resulting in an increase in contact radius a and consequently an increased magnitude for the surface energy contribution U_S. The JKR prediction for the elastic energy component U_E is not consistent with the trend shown by W_{adh}. These observations present a clear picture of plastic deformation as the mechanism responsible for the increased contact area. Hence, both δ and a are found to increase with increasing v_{rel} in a manner which could not occur if the deformation included elastic strain energy. In addition, the computed values of δ plotted in Figure 3.6 are significantly greater than the predictions of JKR. Specifically, JKR theory predicts values of $\delta_{eq} = 0.23$ nm, 0.35 nm, and 0.43 nm for the small, medium, and large nanoparticles, respectively, which in all cases underestimate the values shown in Figure 3.6. This demonstrates enhanced compression beyond the predictions of JKR, consistent with the observation of plastic deformation.

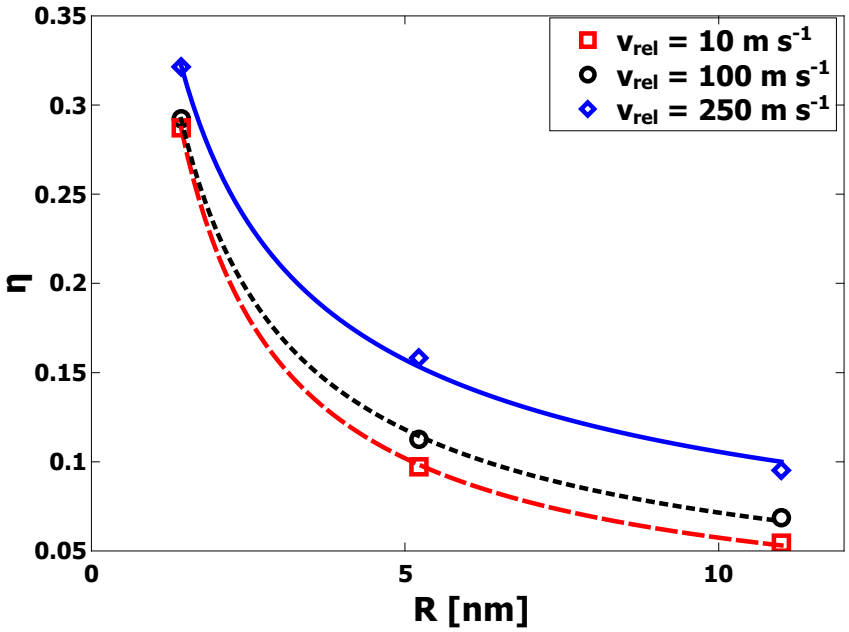

Figure 3.9: Computed values of η plotted as a function of nanoparticle radius. Red circles are for v_{rel} = 10 m s^{-1} and the red long dashed line shows the fitted curve. Black circles are for v_{rel} = 100 m s^{-1} and the black short dashed line shows the fitted curve. Blue diamonds are for v_{rel} = 250 m s^{-1} and the blue solid line shows the fitted curve.

In Figure 3.9, we plot values of η for three velocities as a function of nanoparticle radius R. The gradual increase in η with v_{rel} is consistent with the observation of greater plastic deformation. The decrease in η with increasing radius can be understood to be in part simply a geometric effect. Because the interactions are finite range, when R increases significantly beyond 0.53 nm, the cut off distance for interactions, simple geometric arguments suggest that η should scale as R^{-1}. The actual data shows a trend with a somewhat different scaling exponent, likely due to the fact that the strongest plastic deformation happens for the smallest nanoparticles. The value of η appears to scale with radius R approximately as $R^{-0.83}$ for $v_{rel} = 10$ m s^{-1}. For higher v_{rel}, the scaling changes somewhat. Specifically, for $v_{rel} = 100$ m s^{-1} , η scales as $R^{-0.72}$, while for $v_{rel} = 250$ms^{-1} , η scales as $R^{-0.57}$. The dependence on v_{rel} is clearly due to the fact that K_{trans} becomes dominant in comparison to surface interaction as v_{rel} increases. For low enough velocities the contact area

indicated by η appears to increase approximately linearly with R. The relevance for collisions at very large scale, both in terms of the dissipation mechanism and the crossover towards bouncing behavior, will be addressed in the final section. However, we note that for v_{rel} = 10 m s^{-1} and R = 1 μm, the scaling behavior results in a prediction $\eta \approx 1.2 \times 10^{-3}$, which indicates that the adhesion and dissipation occurs over a much smaller relative area than for $R = 11$ nm and smaller particles.

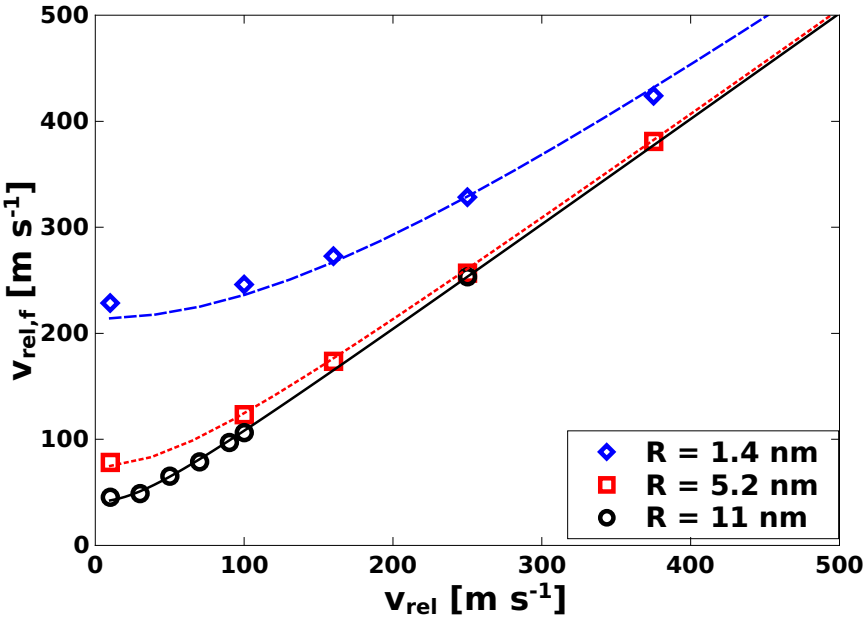

Figure 3.10: Final collision velocity $v_{rel,f}$ plotted as a function of initial kick velocity v_{rel} for all three nanoparticle sizes. This figure clearly demonstrates the existence of a minimum collision velocity due to surface attraction effects. Values are denoted by blue diamonds for R = 1.4 nm, red squares for R = 5.2 nm, and black circles for R = 11 nm; the fitted curves are denoted by a blue short dashed line for R = 1.4 nm, a red long dashed line for R = 5.2 nm, and a black solid line for R = 11 nm.

For small particles $R = 11$ nm and below, the results indicate that plastic deformation always occurs. Indeed, we observe that is not possible at these scales to lower v_{rel} sufficiently to observe elastic behavior consistent with JKR theory. For small particles, surface attraction energy dominates K_{trans} for the lower values of v_{rel}. The result of the strong attraction is that the nanoparticles

accelerate significantly just before the collision, and the effective collision velocity $v_{rel,f}$ can often be substantially greater than the initial velocity v_{rel}. Assuming that the surface interaction is conservative, then the effective collision velocity $v_{rel,f}$ should depend on the initial velocity v_{rel} and the size-dependent velocity v_c,

$$v_{rel,f} = v_c \left[1 + \left(\frac{v_{rel}}{v_c} \right)^2 \right]^{1/2}. \tag{3.13}$$

The value of v_c is a parameter which depends on R and was determined by examination of the maximum nanoparticle velocity during the collision. In Figure 3.10, $v_{rel,f}$ obtained from simulation is plotted as a function of v_{rel} along with the fit curve from Eq. 3.13. All data was used to obtain fits, but only a subset is plotted for clarity. For the three radii $R = 1.4$ nm, $R = 5.2$ nm, and $R = 11$ nm, the values for the fitted parameter v_c are respectively $v_c = 213.9 \pm 4.9$ m s^{-1}, $v_c = 74.3 \pm 1.7$ m s^{-1}, and $v_c = 41.2 \pm 1.5$ m s^{-1}. This demonstrates that, for these small particle sizes, the velocity at collision $v_{rel,f}$ is substantially greater than the lowest value of v_{rel} simulated. Consequently, a simulation with a very small v_{rel} will result in $v_{rel,f} \approx v_c$ as a minimum effective collision velocity. Therefore, while it might be thought that a low enough value of v_{rel} should exist where collisions are elastic, the present results demonstrate that for $R = 11$nm and below, this is not the case. Specifically, for $R = 11$nm, $v_c = 41.2 \pm 1.5$ m s^{-1} is substantially greater than the lowest v_{rel} = 10 m s^{-1}, and even much lower values of v_{rel} would yield essentially the same collisions with plastic deformation. For smaller particles surface attraction is even more important, and the very large values of v_c result in even more dramatic plastic deformation at all values of v_{rel}. In understanding scaling behavior, we note that $v_c \propto R^{-0.81}$. This indicates that as R increases, surface attraction becomes a less significant factor. However, even for $R = 1$ μm particles, the scaling of v_c predicts $v_c \approx 1$ m s^{-1}. Therefore, even if v_{rel} is below 1 m s^{-1}, the effective collision velocity will be $v_{rel,f} \approx 1$ m s^{-1}, which is still substantial and should involve some plastic deformation at the interface. This is further discussed in the last section of the paper.

It is possible to use scaling relations to predict the size R where bouncing will occur. Specifically, one criterion for bouncing is that the kinetic energy during the first rebound should be larger than W_{adh} in order for the particles to separate. We apply this criterion for v_{rel} = 10 m s^{-1} collisions. The results above for η demonstrate that $W_{adh} \propto R^{1.1}$, whereas the kinetic energy during the first rebound scales $K \propto R^{3.4}$, hence eventually the rebound kinetic energy will be substantially greater than W_{adh}. For v_{rel} = 10 m s^{-1}, this criterion results in the prediction that bouncing might occur for $R \approx 23$ nm. However, the fact that substantial plastic deformation occurs casts some doubt on these results, since the neck formed by the deformed surfaces means the behavior is strongly irreversible. In fact, as the results plotted in Figures 3.2, 3.3, and 3.4, demonstrate, even negative values of W_{adh} occur without bouncing, due to the very strong deformation of the particles.

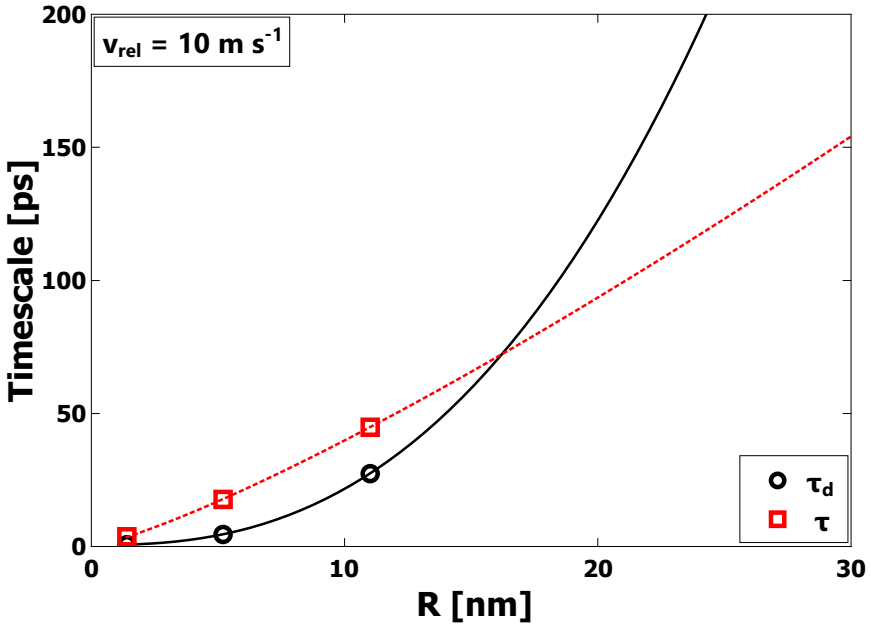

Figure 3.11: Plot of τ and τ_d as a function of nanoparticle radius R for $v_{rel} = 10$ m s^{-1}.

Another approach to predict behavior at larger scales is to use the computed scaling of the oscillation period τ and the damping time τ_d. As described above, bouncing would seem to require $\tau_d >> \tau$ in order for bouncing to occur, since strong dissipation of the kinetic energy of the two

particle oscillations prevents separation of the particles. In Figure 3.11, the scaling of τ and τ_d with particle size R is shown. From Figure 3.11, the fit indicates $\tau \propto R^{1.23}$, and $\tau_d \propto R^{2.50}$, which leads to a crossover at $R = 17.3$nm. Beyond $R \approx 20$ nm, τ_d eventually becomes substantially greater than τ and eventually bouncing should occur.

Conclusions

For metallic nanoparticles of radii $R = 11$ nm and below, simulation results indicate adhesion occurs in every head-on collision. Simulation results show extremely large stress values and strong plastic deformation, indicating that JKR is not applicable in the present case. Because the observed deformation is plastic, it does not include large elastic strain energy contributions predicted by JKR, thereby resulting in a larger contact area that increases strongly with increasing v_{rel}. Moreover, the primary mechanism for the dissipation appears to be connected strongly to the atomic rearrangement that occurs at the interface associated with the plastic deformation. Scaling behavior suggest that for relatively low collision velocities, $v_{rel} \sim 10$ m s^{-1}, nanoparticles would need to be at least $R \sim 20$ nm in order for bouncing to occur.

For nanoparticles, surface attraction can often dominate incident kinetic energy, and plastic deformation is expected to always occur for any v_{rel}. The results show that even for $R \approx 1\mu m$, the relative velocity during the collision is at least $v_{rel,f} \approx 1$ m s^{-1}. Using the scaling of $v_c \propto R^{-0.81}$ at $v_{rel} = 10$ m s^{-1}, and the fact that the mass of a grain scales as R^3, the minimum kinetic energy in a collision scales as $R^{1.38}$. However, the scaling of η at the same v_{rel} shows that the kinetic energy associated with v_c needs to be dissipated over an effective area which scales as $R^{1.1}$. This suggests that the minimum kinetic energy associated with v_c increases more rapidly with R than the area available to dissipate the energy. Therefore, it is quite possible that while dissipation becomes less effective as R increases, and as expected bouncing becomes the dominant behavior, strong plastic

deformation at the contact interface likely occurs. Hence, while v_c decreases with R, the kinetic energy associated with v_c actually increases, and because the relative area for the collision tends to decrease, it is reasonable to expect high stress and plastic deformation at the contact. However, this possibility remains a subject requiring more direct verification.

There is a direct relationship to the conventional explanation of Amonton's laws of friction, wherein dissipative frictional forces are independent of apparent contact area and are solely dependent on the normal force at an interface. This has been contradicted based on the presence of nanoscale asperities[118] which result in an actual contact area which is generally much smaller than the apparent contact area. When normal forces exist, either due to surface attraction or some other applied force, the actual contact area grows often due to plastic deformation of the asperities, and hence the frictional force increases. When the actual contact area is much smaller than the apparent contact area, the stresses in the asperities can become quite large. This is very similar to the results found here. Specifically, since $\eta \propto R^{1.1}$ is less than R^2, the predictions here indicate that as R increases, the stress at the contact point will tend to increase quite dramatically, thereby leading to plastic deformation. However, the results also show that any enhanced dissipation with increasing R is not enough to prevent bouncing behavior at larger values of R.

In addition, the strong attraction which results in the larger effective collision velocities is the same reason plastic deformation occurs. In other words, even when the incident kinetic energy is relatively low, strong interaction tends to result in plastic deformation. As R increases, surface attractive forces do not become weaker. Instead, the area where strong interactions occur increases less rapidly with R than the overall mass of the particles does, and hence the value of v_c decreases with increasing R. However, because the interactions are localized over a smaller relative area, they can still be very strong even when v_c is small. In fact, we expect that not only stresses at the contact are very strong, but that very strong stress gradients likely are responsible for the observed plastic deformation. This point will be a focus of future efforts.

While the general picture of plastic deformation as the dominant mechanism for adhesion and dissipation is in stark contrast to JKR, some features remain consistent. Specifically, the simulations demonstrate the formation of a "neck" which tends to increase the adhesion and more strongly prevent rebound. The distinction is in the mechanism for the formation of the neck, which we find to be plastic deformation rather than elastic deformation. This view is also consistent with previous efforts in simulations of silica particles which demonstrated strong plastic deformation.[41,108] It should also be noted that other works have explored viscoelastic dissipation mechanisms associated with plastic deformation,[99] even though it appears that the dependence of the contact area on v_{rel} and R has not been previously considered. These insights could be of particular interest to the nuclear and pharmaceutical industries, where critical processes depend on tightly controlled powder flows. Additionally, the adhesion of nanoparticles could have a significant effect on their catalytic performance via a reduction in surface area.

Future work will be directed towards elucidating behavior of silicate and other oxide particles, using some of the same approaches here. It is expected that surface bonding occurs with more defects when cations and anions are present, and also that plastic deformation by the motion and generation of dislocations at the interface occurs less readily than with metals. It is also possible that the approach of determining the oscillation and damping times τ and τ_d can be extended to computation of the coefficient of restitution when bouncing occurs.

Acknowledgements

This research was made possible by support from the National Science Foundation, Division of Astronomical Sciences, under grant 1616511. The authors also acknowledge support and computational time provided by the Institute of Simulation and Training and the STOKES computer cluster at the University of Central Florida.

CHAPTER 4: KINETICS AND CHEMISTRY OF ADSORBED ORGANIC SPECIES IN NANOPARTICLE COLLISIONS

As mentioned in the introduction chapter, iron is an ideal material for the modeling and analysis of dissipation during collisions. It is a single element mineral that affords the use of efficient computational algorithms. In addition, it shows strong dissipative effects and possesses a high melting point. As a model material, iron represents an extreme in unpassivated mineral surfaces. Many radical and organic species readily adsorb on iron surfaces.

For this chapter, I chose the model adsorbate CH_2 for a few reasons. Firstly, CH_2 is a simple intermediate hydrocarbon radical which still has some valence electronic states open, so it bonds well. In protoplanetary disks, CH_2 is thought to play a key role in the formation of HCN, as well as being a key hydrocarbon intermediate as C and H_2 can readily radiatively associate.[119]

Therefore, the central idea of this chapter is to explore the role of this adsorbate in dissipation, and how it can chemically evolve on the surface. Prior to collisions, adsorbed CH_2 can be thought of as a kind of kinetically trapped, high energy state. As established in the introduction, both molecular clouds (with many kinds of radicals) and dust are widespread throughout the galaxy - this chapter explores some relationships between these radicals and their role in collisions and mechanocatalysis, and the states that become accessible on mineral surfaces in the space environment once a high energy event such as a collision occurs.

Methods

For all simulations carried out within this chapter, the molecular-dynamics (MD) simulation methodology was utilized. Practically, MD calculations were performed using the LAMMPS simulation

code[113] and an empirical ReaxFF[45] potential specifically designed for the Fe-C-H system and carbon interactions with amorphous Fe phases,[120] which was an extension of a potential set developed by Zou et al.[121] used to model C-H radical chemistry on Fe surfaces. ReaxFF allows charge transfer and equilibration,[122] and is able to capture the physics of charge transfer and transitions between metallic, covalent, and ionic bonding depending on how the chemical environment changes. A small timestep of 0.1 fs was chosen to ensure that even high-energy H-H vibrations would sample many times per oscillation. Charge equilibration was performed on every step.

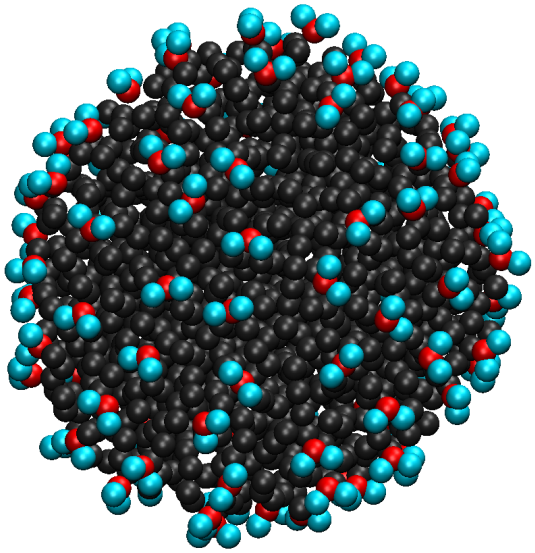

Figure 4.1: An iron nanoparticle with 104 CH_2 radicals adsorbed onto the surface. Fe atoms are dark gray, carbon atoms are red, and hydrogen atoms are blue.

To prepare and then collide a bare amorphous iron nanoparticle, the procedure used in chapter 3 was followed aside from the use of potential, which yielded an 1024 amorphous iron nanoparticle of radius R = 14.1 nm. Collisions were carried out at a variety of velocities with this initial iron nanoparticle, which behaved similarly to those modeled in chapter 3. In a similar fashion, works of adhesion were calculated for those velocities in the range 100 m s^{-1} to 3000 m s^{-1}.

Next, varying combinations of C and H atoms — specifically, C, H, CH, CH_2, CH_3, CH_4, C_2H, C_2H_2, and H_2 — were added to the surface of the bare iron nanoparticle such that they were equally spaced upon the roughly 2500 $Å^2$ of surface area. An example here is given for the placement of one chosen molecule, CH_2, a radical. Carbon atoms were placed such that they were at least 1.5 Å away from the Fe nanoparticle surface and equally spaced apart from one another. Next, two hydrogen atoms were placed 1 Å from each of these carbon atoms, ensuring that they were each at least 2 Å from the Fe nanoparticle surface. The resulting structure then underwent a conjugate-gradient potential energy minimization. Next, it was equilibrated in a constant temperature regime of T = 300 K for 10 ps to allow carbon atoms to reasonably diffuse to lower energy surface sites, ramped down in temperature to T = 5 K for another 10 ps, and then equilibrated at T = 5 K for another 10 ps.

Table 4.1: CH_2 adsorbate coverage summary

# adsorbates	Area per adsorbate $\left(Å^2\right)$	distance to next adsorbate $\left(Å\right)$
104	24.3	4.9
207	12.2	3.5
250	10.1	3.2
293	8.6	2.9
401	6.3	2.5
501	5.0	2.2

At this point the evolutions of these various species were simulated in a constant temperature ensemble, for each coverage level, for 5 temperatures: T = 100, 300, 500, 700, and 900 K. C-H and C-C coordination numbers were determined and tracked over time. C-C bonds were counted when two C atoms were less than 2 Å from each other. The cutoff for counting C-H bonds was 1.5 Å. Their temperatures were ramped up from T = 5 K to the target temperature over a period of 10 ps. Then, mean-squared-displacement and coordination data was collected by simulating the system at the constant target temperature for 40 ps.

Next, adsorption and free cluster energies were calculated for each adsorbate, at a coverage level of 100 adsorbates per nanoparticle. At this coverage level, each adsorbate is approximately 5 Å distant from its neighbors. We then moved on to simulating collisions of two nanoparticles with varying levels of CH_2 adsorbed on their surfaces. These CH_2 coverages were as low as 104 CH_2 groups to as high as 501 CH_2 group per nanoparticle. On the higher side, this coverage was essentially a skin of amorphous carbon with some hydrogen bond termination. These coverages are summarized in table 4.1. Nanoparticles were prepared according to the constant temperature recipe defined above. These particles began with a separation of at least 15 Å between their surfaces, and their centers of mass were given a kick towards each other. Works of adhesion were calculated just as in chapter 3. The resulting collided systems were then analyzed to see how C-H and C-C bonds had evolved over time. All collisions were run in a constant-energy ensemble.

Initially, only the 104xCH_2 coverage level was simulated. A wide range of velocities was chosen for this coverage level. It was then decided to add additional coverage levels, and to only focus on a smaller number of velocities. Thus, all other collisions with coverage levels above 104 were carried out with relative velocities of 250, 1000, 1500, and 2000 m s^{-1}. 10 collisions were performed per relative velocity, where the rotational orientation of the nanoparticles was varied at the beginning of each simulation.

Table 4.2: Cluster and adsorbate properties. Free floating and adsorption energies, C-H bond lengths. The energies for CH_2 are entirely coincidental.

Molecule	Formation/Adsorption energy (eV)	Cluster/Adsorbed C-H bond length (Å)
C	0.0 / -7.76	* / *
H	0.0 / -2.12	* / *
CH	-4.49 / -5.51	1.04 / 1.07
CH_2	-6.56 / -6.56	1.04 / 1.09
CH_3	-13.2 / -2.96	1.04 / 1.09
CH_4	-17.5 / -1.20	1.06 / 1.07
C_2	-8.11 / -7.27	* / *
H_2	-4.71 / -0.342	* / *
C_2H	-12.3 / -5.29	1.05 / 1.08
C_2H_2	-17.4 / 2.2	1.05 / 1.07

Free-floating and adsorbed energies (and C-H bond lengths, when relevant) for molecules were calculated and are reported in table 4.2. The energies for CH_2 are entirely coincidental. A few trends can be observed. There is some stretching of C-H bonds when adsorbed on an iron surface. Adsorption energies for CH_x peak with CH_2, and H_2 and CH_4 are only weakly adsorbed, consistent with these molecules' full valence states. The difference of adsorption energies for H and H_2 (H is more than 1.75 eV more strongly bound to the Fe surface) leads to an H_2 desorption mechanism common in all simulated collisions and NVT constant temperature runs. First, a hydrogen atom dissociates from a carbon atom, and begins freely diffusing on the nanoparticle surface. It then finds another hydrogen atom, and becomes an $H_{2,ads}$ molecule. Temperature increases lead to the thermally activated desorption of these hydrogen molecules at higher temperatures, as there is only a modest adsorption energy barrier to overcome.

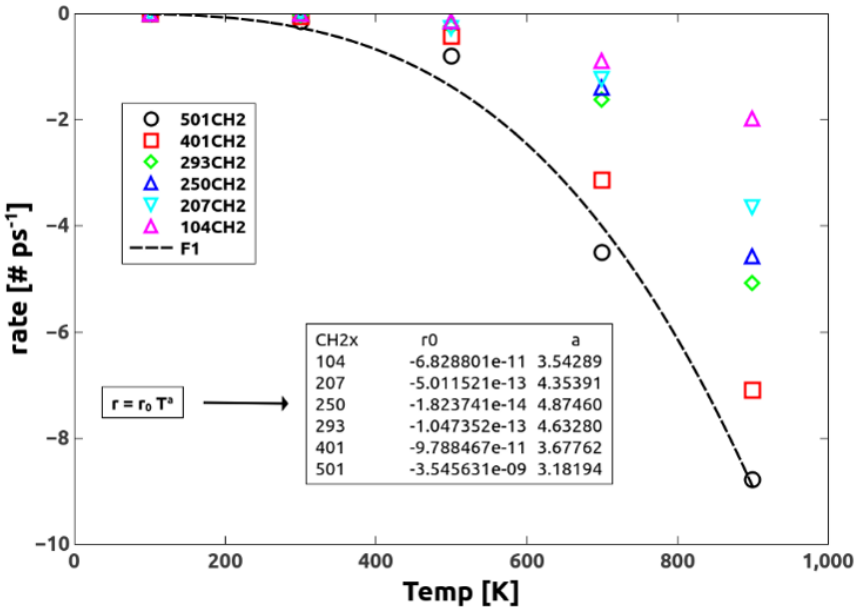

Figure 4.2: CH_2 decomposition rates at various temperatures, dashed line is fit for N=501

Consider the evolution of adsorbed CH_2 in a constant temperature, non-collision setting. Here, various coverage levels of CH_2 were placed onto a nanoparticle surface, which was then run at constant temperature for 40 ps for varying temperatures. Changes in C-H coordination numbers allowed tracking of how many carbons, over time, were still coordinated with two hydrogen atoms. The rate of this change over time was found to be constant, and linear rate constants were calculated for all temperatures and coverage levels. These rate constants are plotted in figure 4.2 per coverage level as a function of temperature, and a simple power law fit was performed per coverage level, to get the rate dependence upon temperature. These power laws can then be compared to later collisional results. Constant temperature C-C bond formation rates due to surface diffusion of C atoms, which may or may not have any hydrogen atoms attached, were also computed and are plotted in figure 4.3.

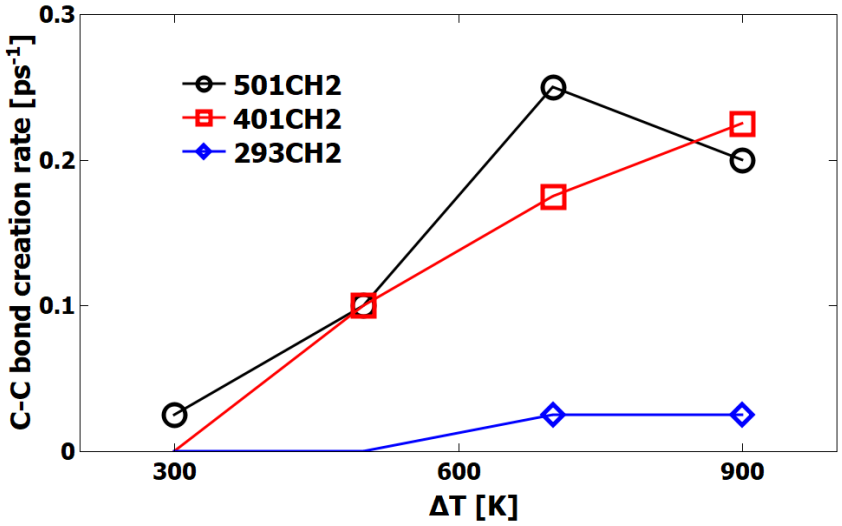

Figure 4.3: C-C bond formation rates at various temperatures from NVT. Only temperatures and coverages which saw bond formation are plotted with symbols.

Turning to the collision simulation results, we first look at the change in temperature from the initial T = 5 K system, to the post-collided system which has warmed due to dissipation of the initial translational kinetic energy. Here, in comparison to bare iron nanoparticle collisions, final system temperatures show a marked decrease with increasing surface coverage. These final temperatures are plotted as a function of collision velocity for varying coverages in figure 4.4. Comparing the bare nanoparticle to the highest coverages, some sort of activity seems to be occurring related to the adsorbates. Of course, our model reaction, molecular hydrogen desorbing from CH_2, certainly does seem to occur. Figure 4.5 plots the change in CH_2 population as a function of collision velocity. Here, we see clearly that the collisions with the highest temperatures correlate to those with the largest decrease in adsorbed CH_2. Looking in detail at one collision velocity, v_{rel} = 2000 m s^{-1}, and at the highest coverage level, the change in the number of adsorbed CH_2 is plotted as a function of time for all 10 collisions in figure 4.6. Their mean is also plotted as a black dashed line, and the prediction made by the NVT fits plotted in figure reffig:adsNVTCH2 as a red dashed line. Clearly, the two are in good agreement here. CH_2 evolution on the surface of iron nanoparticles

on the timescale of this simulation, 40 ps, seems to be governed by simple thermally activated, temperature-driven effects.

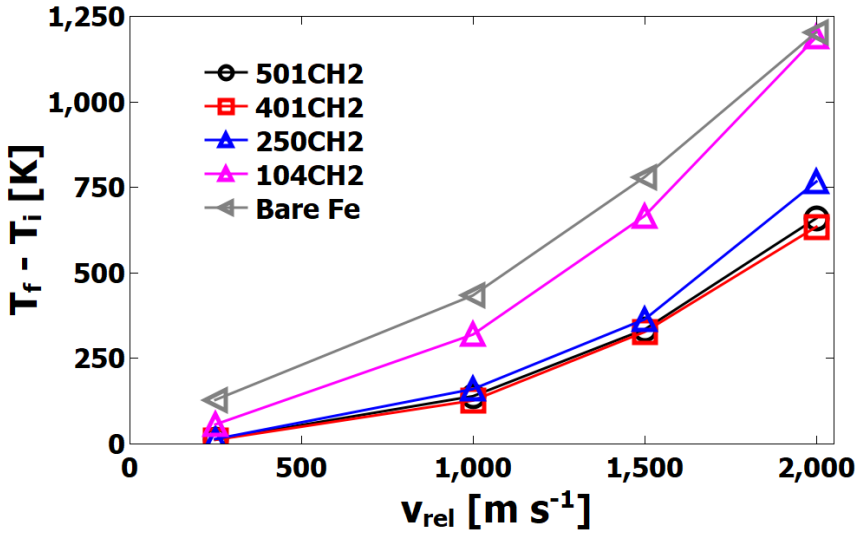

Figure 4.4: Change in temperate for various coverages as a function of collision velocity

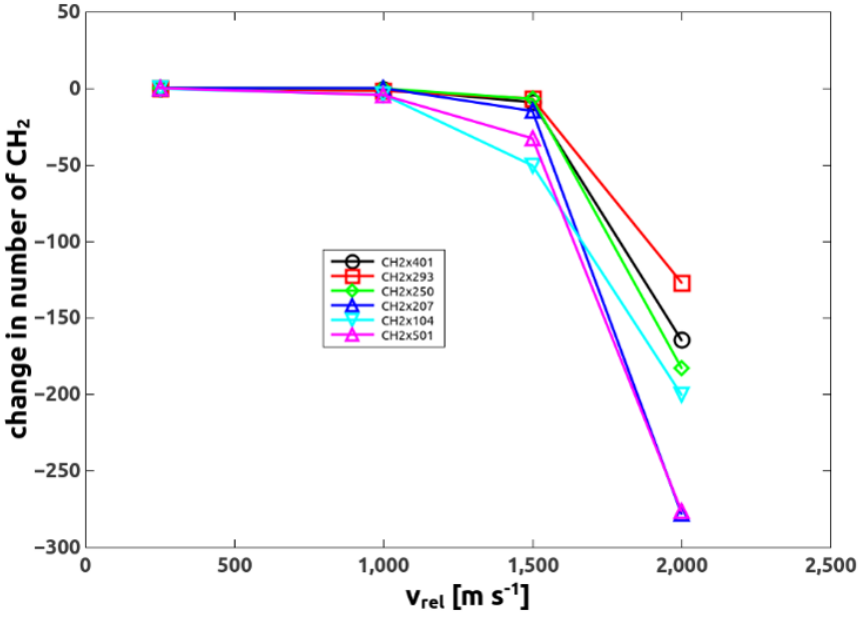

Figure 4.5: Change in CH_2 population for various coverages as a function of collision velocity

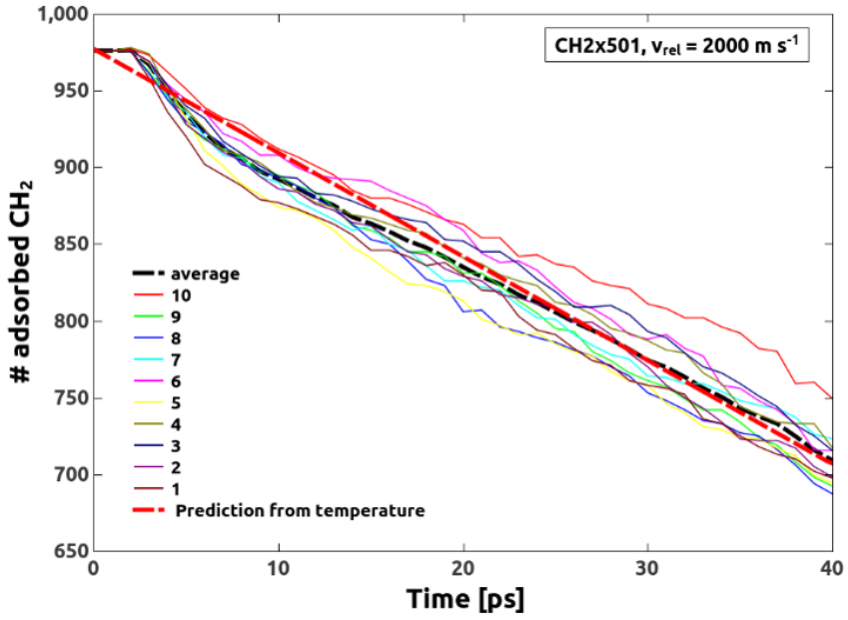

Figure 4.6: Change in CH_2 population over time for the highest coverage level from collisions, and comparison to NVT rate constant predictions - very good agreement

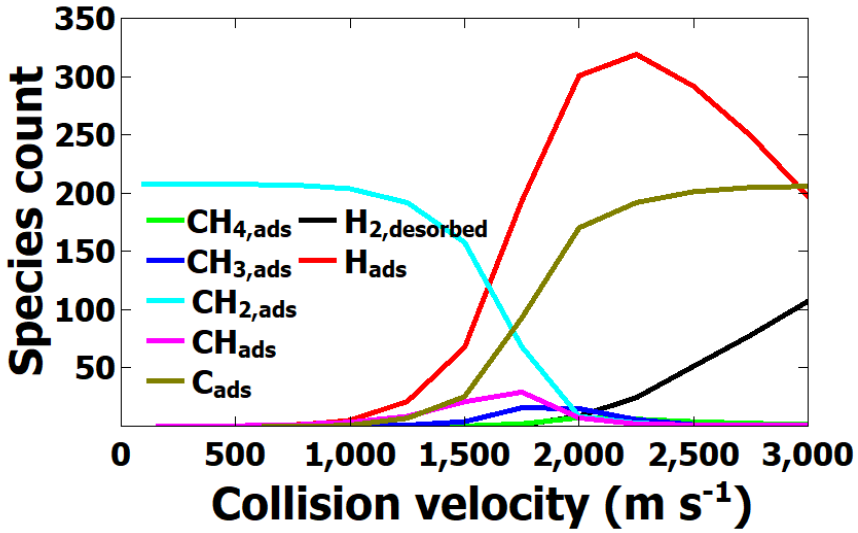

Figure 4.7: Change in all species for 104 coverage level collisions

Now, we will examine in detail the count of all species on the surface of an iron nanoparticle as a function of collision velocity for the lowest coverage level, 104 CH_2 groups. These data are plotted in figure 4.7. These collisions, allowed to equilibrate for 40 ps after the collision, show increasing activity with increasing collision velocity (and thus increasing temperature). At around v_{rel} = 1250 m s^{-1}, which corresponds to about T = 450 K, we see the beginnings of activity. The number of CH_2 groups decreases, along with a rise in the populations of CH, C_{ads}, and H_{ads}. As velocities and temperatures increase further, more and more hydrogen dissociates from any carbon atoms at all, and molecular hydrogen begins to form and desorb. At the highest velocity, all hydrogen has dissociated from carbon atoms and is either freely surface diffusing, or has desorbed as molecular hydrogen. Thus the main reaction pathway seems to be,

$$CH_{2,ads} \rightarrow C_{ads} + 2H_{ads} \rightarrow C_{ads} + H_{2,desorbed}, \tag{4.1}$$

which is endothermic and requires about 0.65 eV of energy per radical. One can easily verify this from the data in table 4.2. When one considers the numbers of CH_2 groups which have dissociated and the amount of H_2 which has desorbed, this mechanism clearly accounts for a large amount of the difference in temperatures between systems with CH_2 radicals and bare nanoparticles. As a consequence, it is an instance of the well-known Le Chatelier's principle. Here, an increase in temperature has freed some energy to drive endothermic chemical reactions on the surface.

One can in principle compare the work of adhesion for a system with adsorbates, and one without, and then compare the two. Calculating W_{adh} controls for the increased number of particles as it has a heat capacity-like term ($3Nk_B$) which scales linearly with the number of particles. The works of adhesion for the bare and smallest coverage case are plotted in figure 4.8. Additionally, if one goes along and accounts for all C-C and C-H coordination changes, one can use the data in table 4.2 to count up all the contributions due to these coordination changes.

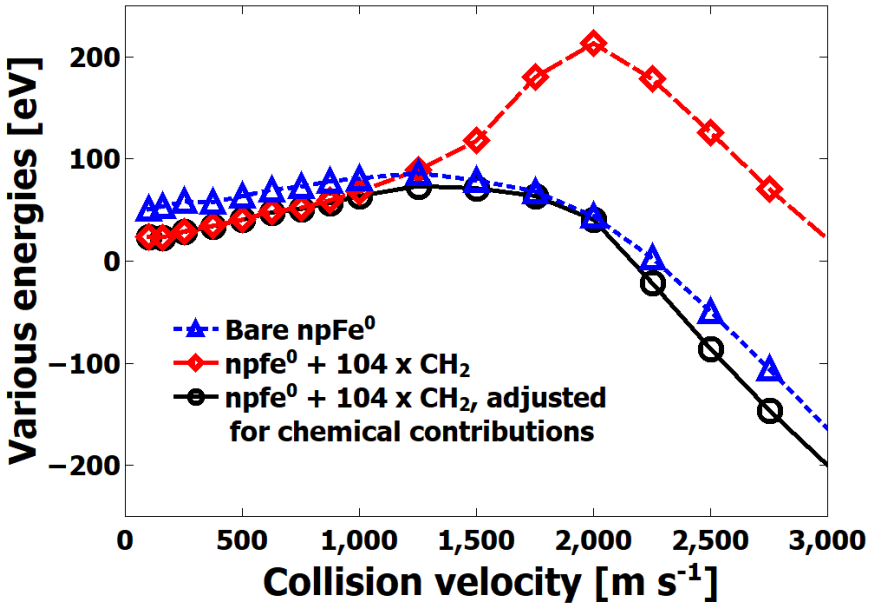

Figure 4.8: Comparison of various adhesion energies

Here, in figure 4.8, W_{adh} for a range of collision velocities is reported in blue for the bare system, and in red for the system with adsorbates. At lower velocities, the work of adhesion is only moderately reduced, consistent with a reduced surface energy due to the partial coordination of surface atoms by adsorbates. Note that the system with adsorbates has a distinct change in behavior compared to the bare system at about 1250 m s^{-1}. This velocity and temperature is precisely where we began to see chemical evolution in figure 4.7. Finally, the black line in figure 4.8 is the work of adhesion for the particle with adsorbates, but corrected for the chemical coordination changes. At higher velocities, these changes in coordination number account quite well for the observed changed in adhesion energy.

One specific reaction of interest was the formation of carbon-carbon bonds. It was initially hoped that the presence of radicals on the surface would lead to extensive carbon bonding, and thus via this nominally exothermic process increase dissipation and adhesion of nanoparticles. This reac-

tion, simply $2C_{ads} \rightarrow C_{2,ads}$ was in our simulations observed only at rates which can be accounted for by simple surface diffusion and thermal effects.

Figure 4.9 shows the change in the number of carbon-carbon bonds as a function of collision velocity. Again, all collided systems were allowed to equilibrate for 40 ps post-collision, a time which matches the run time of the diagnostic constant temperature simulations. There is only very modest C-C formation except for the highest temperatures and coverages. This is consistent with the constant temperature results plotted in 4.3.

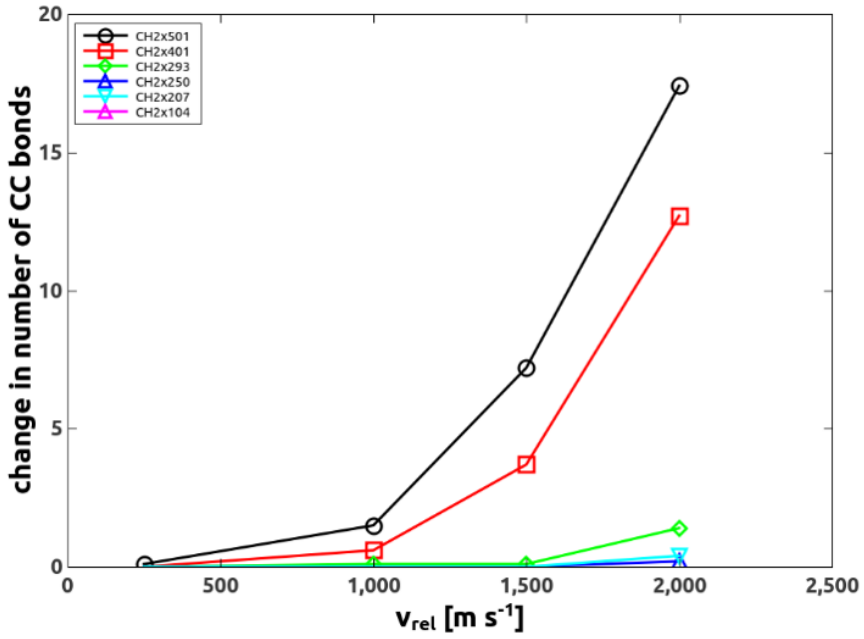

Figure 4.9: C-C bond formation from collisions

Additionally, we looked in detail at carbon-carbon bonding at the highest velocity (and thus highest temperature), for the two highest coverages. The individual simulation data are plotted, along with their mean, in figure 4.10. A simple fit of the form $\sqrt{time}$ matches the data quite nicely for both coverages, with a very high confidence rating of $R^2 > 0.995$. This perhaps indicates a simple mean-squared-displacement type surface diffusion mechanism where C atoms find each other and bond.

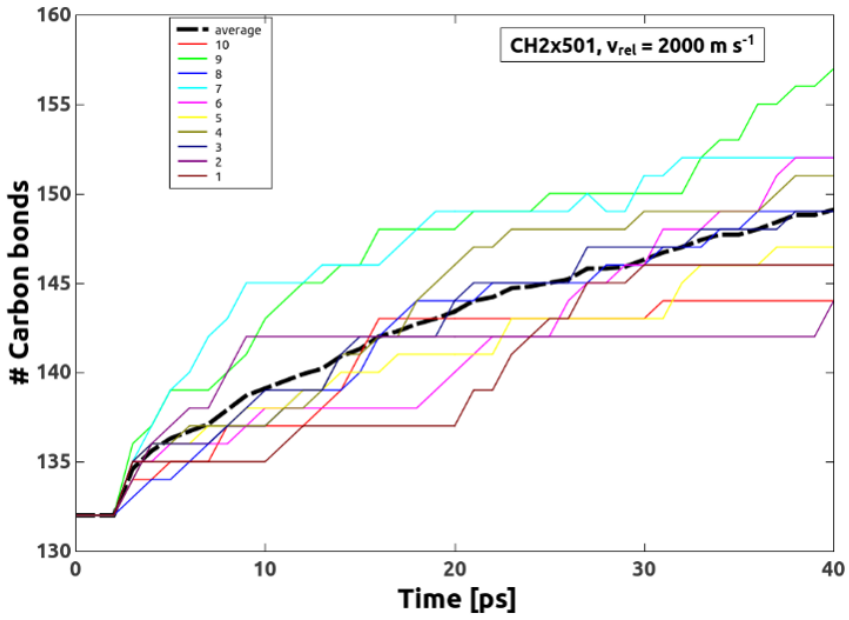

Figure 4.10: TOP: C-C bond formation evolution over time for N=401 coverage, $y \sim 2.03\sqrt{time}, R^2 > 0.995$. BOTTOM: the same for N=501 coverage. Here, the number of bonds goes like $y \sim 2.71\sqrt{time}, R^2 > 0.995$.

Looking at the (admittedly noisy) C-C bond formation rates from the constant temperature runs, one can see that these rates are adequate to explain all C-C bonding observed in collided systems.

Much of the more complex chemistry likely takes place on timescales much longer than those currently able to be simulated with the molecular-dynamics formalism, yet these results do demonstrate that iron nanoparticles, as a model mineral surface, prepared in a manner expected to occur in the space environment, can play host to a variety of chemical changes when adsorbates are present. It has also been demonstrated that these chemical states and changes affect dissipation.

CHAPTER 5: A MICROSCOPIC DESCRIPTION OF DISSIPATION

Dissipation is the phenomenon wherein some sort of whole-body motion and its inherent kinetic energy turns into thermal vibrations in the internal degrees of freedom which make up that object, and any other objects with which it interacts. In this chapter, a model is presented for dissipation which can account for per-mode contributions and which depends only on interaction forces and velocities. In this way the internal degrees of freedom of a large system are represented as normal modes. These degrees of freedom are the participants in the dissipative process. Here, we will use it to analyze nanoparticle collisions, but it can be readily adapted for a variety of dissipative contexts, including with nanotribology. Additionally, this model can also be applied within a density functional theory context to study additional chemical and electronic influences on dissipation in general.

Building upon that work, here two different head-on collisions of iron nanoparticles are analyzed and represented as a series of harmonic oscillators to elucidate dissipative behaviors. For the initial analysis of these nanoparticle collisions, please see chapter 3. In the below sections, we will present the results of this model for two different collisions. One is allowed to proceed normally as per the collisions in chapter 3, but the other has a constraint force applied upon its center of mass to reduce inter-surface attraction and consequent high collision velocity. This model bears a remarkable similarity to some models of tribology, a connection which will be further explored later in this chapter. This framework has been generalized, as it is also intended to be used in density functional calculations to elucidate additional chemical and electronic contributions to dissipation. We will demonstrate the relevance of surface chemistry and interactions in dissipative and chemical processes on mineral surfaces, and posit that using density functional theory to further investigate this problem will elucidate detailed chemical and electronic effects on dissipation.

Methods

The specific simulation details and potential are provided in chapter 3, but a quick summary will be given here. Using molecular-dynamics, we simulate the dynamics of iron nanoparticles using an empirical embedded-atom inter-atomic potential. Integrating the atomic equations of motion numerically, one evolves the system classically, with a time step chosen to be small enough to ensure energy conservation. In this chapter, two collisions between 1024-atom Fe nanoparticles were carried out under differing collision conditions: one at a relative velocity of 100 m s^{-1}, and another at 10 m s^{-1}. Additionally, the slower collision was subjected to additional constraints which slowed its acceleration due to inter-surface attraction. Using the trajectory files generated by the molecular-dynamics simulation, it is possible to represent the nanoparticles as a series of oscillators and thus gain a new understanding of dissipation.

Eigenstate Calculation

Here, we will perform a transform of the positions and velocities of a system during a collision. We then will describe a set of particles as a set of simple harmonic oscillators. During a collision or interaction with another surface, those oscillators on both surfaces can be coupled by interactions between the two surfaces. We consider the positions of the particles in terms of their equilibrium coordinate R, which might be changing with time if the particles are translating, as during a collision, and the displacements from equilibrium u. These equilibrium coordinates R can changing over time due to rotations and other deformations. Specifically, we define the position of atom i in Cartesian direction μ at time t as,

$$r_{i\mu}(t) = R_{i\mu}(t) + u_{i\mu}(t). \tag{5.1}$$

From hereon the time dependence of these coordinates and their time derivatives will be implicit. The Hamiltonian for small displacements in the harmonic regime is, for kinetic energy T and potential energy V,

$$H^{harm} = T + V^{harm} = \sum_{i\mu} \frac{p_{i\mu}^2}{2m_i} + V_0 + \frac{1}{2} \sum_{i\mu} \sum_{j\nu} \Phi_{i\mu,j\nu} u_{i\mu} u_{j\nu}, \tag{5.2}$$

where V_0 can be arbitrarily set to zero, we have,

$$V = \frac{1}{2} \sum_{i\mu} \sum_{j\nu} \Phi_{i\mu,j\nu} u_{i\mu} u_{j\nu}, \tag{5.3}$$

and the equation of motion for particle i in direction μ is,

$$m_i \frac{d^2 u_{i\mu}}{dt^2} = -\sum_{j,\nu} \Phi_{i\mu,j\nu} u_{j\nu}. \tag{5.4}$$

At zero temperature, the kinetic energy is zero and the spring constant matrix element $\Phi_{i\mu j\nu}$ of oscillator i in direction μ acting on atom j of direction ν takes the form,

$$\Phi_{i\mu,j\nu} = \left[\frac{\partial^2 U}{\partial r_{i\mu} \partial r_{j\nu}} \right]_0, \tag{5.5}$$

with U being the potential energy of the system. When this matrix Φ is divided by a mass, its units become those of angular momentum squared. We define the dynamical matrix elements $D_{i\mu j\nu}$ as,

$$D_{i\mu j\nu} = \frac{\Phi_{i\mu,j\nu}}{(m_i m_j)^{1/2}}. \tag{5.6}$$

We write the characteristic equation for this system as so,

$$\sum_{j\nu} D_{i\mu j\nu}\varepsilon_{j\nu,\lambda} = \omega_\lambda^2 \varepsilon_{i\mu,\lambda}. \tag{5.7}$$

We can then solve this system of equations to yield the eigenstates. Here, for N atoms in a nanoparticle, we have a set of 3N harmonic oscillators, one per atom per degree of freedom. We have 3N normal modes λ, with 3N eigenvalues ω_λ^2 and eigenvectors $\varepsilon_{i\mu,\lambda}$. The equation of motion can be solved with the following ansatz,

$$u_{i\mu}(t) = a_\lambda m_i^{-1/2} \varepsilon_{i\mu,\lambda} e^{-i\omega_\lambda t}. \tag{5.8}$$

The total energy of this system is simply the sum of the energy in each mode, which is to say over all degrees of freedom,

$$E_\lambda = a_\lambda^* a_\lambda \omega_\lambda^2 \tag{5.9}$$

$$E_{tot} = \sum_\lambda E_\lambda \tag{5.10}$$

.

In a practical fashion, the workflow for this process proceeds in the follow manner. A collision is simulated in molecular dynamics software. We chose the popular code LAMMPS.[113] Every N_{step} steps, the positions and velocities of all atoms are written to trajectory files. Then for these every N_{step} steps, eigenstates are calculated like so,

1. Positions and velocities for each nanoparticle are separated into separate files.

2. Each of these resulting structures undergoes an energy minimization such that changes in forces and energies are less than 1 part in 10^{-12}. This ensures that all particles are at the bottom of their potential wells.

3. For N atoms per nanoparticle, 6N structures are generated wherein each atom is displaced in the positive and negative x, y, z Cartesian directions by $\Delta d = 0.0005$Å. This displacement is chosen to be small enough such that the harmonic approximation applies.

4. Per nanoparticle, forces are calculated from these 6N structures. These are averaged over positive and negative Cartesian directions to yield 3Nx3N forces.

5. Per nanoparticle, for pairs of atoms i and j, and Cartesian directions μ and ν, the force $F_{i\mu j\nu}$ on atom i in direction μ exerted when atom j is displaced in direction ν by Δd is used to construct the dynamical matrix:

$$D_{i\mu,j\nu} = -\frac{F_{i\mu,j\nu}}{\Delta d\sqrt{m_i m_j}}, \tag{5.11}$$

   where m_i and m_j denote the masses of atoms i and j. The units of $\mathbf{D}$ are the square of angular frequency, specifically, $eV\ amu^{-1}\ A^{-2}$.

6. The 3Nx3N dynamical matrix $\mathbf{D}$ is diagonalized, and its eigenfrequencies ω_λ^2 are converted to THz. The eigenvectors ε_λ are calculated for each mode λ. There are 3N total normal modes, 3 of which are zero due to translational symmetry and 3 of which are very small as they correspond to rotations of the entire nanoparticle. Therefore, practically, there are 3N-6 normal modes calculated for each nanoparticle per timestep desired.

Estimating Per-Mode Power

We now concern ourselves with determining how inter-surface interactions change mode energies. Thus, we start with taking the time derivative of the energy in mode λ,

$$\frac{dE_\lambda}{dt} = \left(\frac{da_\lambda^*}{dt}a_\lambda + \frac{da_\lambda}{dt}a_\lambda^*\right)\omega_\lambda^2. \tag{5.12}$$

Due solely to interactions between the two surfaces the normal mode amplitudes will change. Ignoring the constant phase factor in the expressions above, we can write perform an inverse transform to get the expressions for the normal mode amplitudes,

$$a_\lambda = \sum_{i\mu} m_i^{1/2}\left(u_{i\mu} + i\frac{v_{i\mu}}{\omega_\lambda}\right)\varepsilon_{i\mu,\lambda}^* \tag{5.13}$$

$$a_\lambda^* = \sum_{i\mu} m_i^{1/2}\left(u_{i\mu} - i\frac{v_{i\mu}}{\omega_\lambda}\right)\varepsilon_{i\mu,\lambda} \tag{5.14}$$

Above, the velocities are in the center-of-mass frame. However, velocities from a simulation may not be in this frame of reference, as the entire set of particles as a whole may be translating (as in the run up to a collision). Therefore, we define the center-of-mass velocity $v_{i\mu}$ as the difference between the center of mass velocity V_μ and same-frame velocity $v'_{i\mu}$, and then take its derivative. This yields,

$$v_{i\mu} = v'_{i\mu} - V_\mu, \tag{5.15}$$

and,

$$\frac{dv_{i\mu}}{dt} = \frac{dv'_{i\mu}}{dt} - \frac{dV_\mu}{dt} = \frac{F_{i\mu}}{m_i} - \frac{F_\mu^{(tot)}}{M}. \tag{5.16}$$

Note the time derivative of the displacements can be expressed in terms of these velocities as well,

$$\frac{du_{i\mu}}{dt} = v_{i\mu} = v'_{i\mu} - V_\mu. \tag{5.17}$$

Thus, for the time derivatives of the mode amplitudes, we get,

$$\frac{da_\lambda}{dt} = \sum_{i\mu} m_i^{1/2} \left[v_{i\mu} + i\left(\frac{F_{i\mu}}{m_i} - \frac{F_\mu^{tot}}{M}\right)\left(\frac{1}{\omega_\lambda}\right)\right] \varepsilon^*_{i\mu,\lambda}, \tag{5.18}$$

and

$$\frac{da^*_\lambda}{dt} = \sum_{i\mu} m_i^{1/2} \left[v_{i\mu} - i\left(\frac{F_{i\mu}}{m_i} - \frac{F_\mu^{tot}}{M}\right)\left(\frac{1}{\omega_\lambda}\right)\right] \varepsilon_{i\mu,\lambda}. \tag{5.19}$$

If the nanoparticle is made of a large number of equal-mass particles, then $\frac{m_i^{1/2}}{M} \ll 1$, and we get,

$$\frac{da_\lambda}{dt} = \sum_{i\mu} m_i^{1/2} \left[v_{i\mu} + i\left(\frac{F_{i\mu}}{m_i\omega_\lambda}\right)\right] \varepsilon^*_{i\mu,\lambda}, \tag{5.20}$$

and

$$\frac{da^*_\lambda}{dt} = \sum_{i\mu} m_i^{1/2} \left[v_{i\mu} - i\left(\frac{F_{i\mu}}{m_i\omega_\lambda}\right)\right] \varepsilon_{i\mu,\lambda}. \tag{5.21}$$

Recall that,

$$\frac{dE_\lambda}{dt} = \left(\frac{da_\lambda^*}{dt} a_\lambda + \frac{da_\lambda}{dt} a_\lambda^* \right) \omega_\lambda^2. \tag{5.22}$$

In general, the forces between atoms can be expressed as the sum of inter-particle and intra-particle components, and also harmonic and non-harmonic components,

$$F_{i\mu} = F_{i\mu}^{inter} + F_{i\mu}^{intra} = F_{i\mu}^{inter} + F_{i\mu}^{intra,harm} + F_{i\mu}^{intra,anharm}. \tag{5.23}$$

The harmonic contribution is,

$$F_{i\mu}^{intra,harm} = -\sum_{j\nu} \Phi_{i\mu,j\nu} u_{j\nu}. \tag{5.24}$$

If purely harmonic intra-particle forces were acting, then we would get,

$$\frac{da_\lambda^*}{dt} = \frac{da_\lambda}{dt} = 0. \tag{5.25}$$

Thus, we can eliminate this contribution from Eqn. 5.23. What remains can be substituted into the mode energy time derivative,

$$\frac{dE_\lambda}{dt} = \left[-i \sum_{i\mu} m_i^{1/2} \left(\frac{F_{i\mu}^{inter}}{m_i \omega_\lambda} + \frac{F_{i\mu}^{intra,anharm}}{m_i \omega_\lambda} \right) \varepsilon_{i\mu,\lambda} \right] \left[\sum_{j\nu} m_j^{1/2} \left(u_{j\nu} + i \frac{v_{j\nu}}{\omega_\lambda} \right) \varepsilon_{j\nu,\lambda}^* \right] + h.c. \tag{5.26}$$

Terms involving $v_{i\mu}u_{j\nu}$ and $v_{i\mu}v_{j\nu}$ are separated into inter-particle and intra-particle, and harmonic and anharmonic contributions. In the harmonic regime, Eqn. 5.25 applies, and these specific terms involve those products. Physically, it also must be the case that only terms that include either anharmonic intra-particle forces or inter-particle forces can generate normal mode energy or redistribute that energy between the modes. Terms with products $F_{i\mu}^{inter}u_{j\nu}$ and $F_{i\mu}^{intra,anharm}u_{j\nu}$ in the above equation vanish as the real-symmetric force-constant matrix yields real eigenvectors. Additionally, in this manner all imaginary contributions drop out when products of two amplitudes are taken. All of this being taken into account,

$$\frac{dE_\lambda}{dt} = \sum_{i\mu}\sum_{j\nu}\left(\frac{m_j}{m_i}\right)^{1/2}\left[F_{i\mu}^{inter}+F_{i\mu}^{intra,anharm}\right]v_{j\nu}\left[\varepsilon_{i\mu,\lambda}^{*}\varepsilon_{j\nu,\lambda}+\varepsilon_{i\mu,\lambda}\varepsilon_{j\nu,\lambda}^{*}\right]. \tag{5.27}$$

With real eigenvectors,

$$\frac{dE_\lambda}{dt} = 2\sum_{i\mu}\sum_{j\nu}\left(\frac{m_j}{m_i}\right)^{1/2}\left[F_{i\mu}^{inter}+F_{i\mu}^{intra,anharm}\right]v_{j\nu}\varepsilon_{i\mu,\lambda}\varepsilon_{j\nu,\lambda}. \tag{5.28}$$

These per-mode powers can be numerically integrated over time to yield per-mode energies over time, and the evolution of those energies.

Direct Calculation of Per-Mode Kinetic Energies via Atomic Velocities

There is an alternative method which directly yields per-mode kinetic and potential energies. Unfortunately, this method cannot be used to calculate potential energies in non-periodic systems due to thermal expansion, for reasons that will be explained shortly. However, this can be used to directly calculate kinetic energies and this can be compared to the previous subsection's method.

First, the per-atom displacements from equilibrium $u_{i\mu}$ and velocities $v_{i\mu}$ for each atom i, and each Cartesian direction μ, are used to construct per-mode normal mode coordinates and velocities via projection onto the eigenvectors ε_λ and eigenfrequencies ω_λ. These real mode amplitudes differ from those in the previous subsection, as here we have uncoupled positions and velocities, thus all imaginary components here are zero. Taking m_i as the mass of atom i and with the assumption of real eigenvectors, these normal mode variables and their time derivatives are defined as,

$$b_\lambda = \sum_{i\mu} m_i^{1/2} u_{i\mu} \omega_\lambda \varepsilon_{i\mu,\lambda}, \tag{5.29}$$

and,

$$\dot{b}_\lambda = \sum_{i\mu} m_i^{1/2} v_{i\mu} \varepsilon_{i\mu,\lambda}, \tag{5.30}$$

Using these quantities, we can calculate the per-mode and overall kinetic (T), potential (U), and total (E) energies via:

$$T_{all} = \sum_\lambda T_\lambda = \sum_\lambda \dot{b}_\lambda^2, \tag{5.31}$$

$$U_{all} = \sum_\lambda U_\lambda = \sum_\lambda b_\lambda^2, \tag{5.32}$$

and

$$E_{all} = \sum_{\lambda} (T_{\lambda} + U_{\lambda}) \,. \tag{5.33}$$

Unfortunately, the definition of q, and thereby U_{λ}, U_{all}, and E, depends on the per-atom displacement u, which is defined as the distance from an (elastic) equilibrium position. However, this equilibrium position itself can vary in non-periodic systems due to thermal expansion over time, which certainly happens in these simulated collisions, and is therefore not a valid reference state for these purposes. However, the kinetic energy calculated here is accurate, as will be demonstrated in the results section.

Simulating the Effects of Increased Mass

Next, a method is described to apply a constraint force F_c to the center of mass of each nanoparticle such that their acceleration a is reduced by a factor of α:

$$a' = \frac{a}{\alpha} = \frac{F_{tot}}{\alpha M_{tot}} = \frac{F'_{tot} - F_c}{M_{tot}}. \tag{5.34}$$

Here, F_{tot} refers to the sum of forces originally acting upon the nanoparticle— practically, this means the inter-surface attractive force felt by one nanoparticle due to another, caused by under-coordinated surface atoms— and M_{tot} is the total mass of the nanoparticle. Solving for F_c, we get this simple expression for the constraint force F_c,

$$F_c = -\frac{\alpha - 1}{\alpha} F_{tot}. \tag{5.35}$$

This constraint force is calculated (independently for each nanoparticle) and applied to the center of mass of each nanoparticle on every timestep.

Calculation of the Coupling of Vibrational Modes between Surfaces

Once we have determined how E_λ evolves over time and which modes are most responsible for dissipation, we can compute the coupling of modes between surfaces. We define $\mathbf{\Phi^0}$ for the two-surface system as a block diagonal matrix where the top-left block and bottom-right block would be equal to $\mathbf{\Phi}$ in subsection 5 for a single surface, with all other elements being zero. This would correspond to a two-surface system where the surfaces are infinitely separated in space. One can consider the overall system of vibrational modes in terms of this infinitely separated matrix and a perturbation $\mathbf{\Gamma}$ which will represent the mixing of vibrational modes when the surfaces approach each other,

$$\Phi_{i\mu jv} = \Phi^0_{i\mu jv} + \Gamma_{i\mu jv}. \tag{5.36}$$

At infinite separation, all elements of $\mathbf{\Gamma}$ would be zero, and $\mathbf{\Phi} = \mathbf{\Phi^0}$. Restating the potential energy,

$$U = \frac{1}{2} \sum_{<i,j>} \sum_{\mu,v}^{1,2,3} \left(\Phi^0_{i\mu jv} u_{i\mu} u^*_{jv} + \Gamma_{i\mu jv} u_{i\mu} u^*_{jv} \right), \tag{5.37}$$

we can constrain the separation between the two surfaces with either MD or DFT. At each separation, we can calculate the overall force constant matrix, and obtain the perturbation matrix via $\mathbf{\Gamma} = \mathbf{\Phi^0} - \mathbf{\Phi^0}$. Restating the potential energy in terms of the amplitudes and eigenvectors of the

isolated surfaces for all pairs of modes $<\lambda,\lambda^{'}>$ from the two-surface system:

$$U = \left(\frac{1}{2}\sum_{<i,j>}\sum_{\mu,\nu}^{1,2,3}\sum_{<\lambda,\lambda'>} a^{*}_{\lambda}a_{\lambda'}\varepsilon_{i\mu\lambda}\Phi^{0}_{i\mu j\nu}\varepsilon_{j\nu\lambda'}\right) + \left(\frac{1}{2}\sum_{<i,j>}\sum_{\mu,\nu}^{1,2,3}\sum_{<\lambda,\lambda'>} a_{\lambda}a_{\lambda'}\varepsilon_{i\mu\lambda}\Gamma_{i\mu j\nu}\varepsilon_{j\nu\lambda'}\right) \tag{5.38}$$

Expressing the left-hand set of parentheses in terms of amplitudes and frequencies, and the right-hand set of parentheses in terms of a coupling matrix $\boldsymbol{\tau}$,

$$U = \left(\frac{1}{2}\sum_{\lambda}\omega^{2}_{\lambda}a^{*}_{\lambda}a_{\lambda}\right) + \left(\sum_{<\lambda,\lambda'>} a^{*}_{\lambda}a_{\lambda'}\tau_{\lambda\lambda'}\right) \tag{5.39}$$

The following expression will be used to explicitly calculate the coupling matrix elements in terms of the perturbation matrix $\boldsymbol{\Gamma}$ and the eigenvectors $\boldsymbol{\varepsilon}_{i\lambda}$ of the isolated surface:

$$\tau_{\lambda\lambda'} = \frac{1}{2}\sum_{<i,j>}\sum_{\mu,\nu}^{1,2,3} a^{*}_{\lambda}a_{\lambda'}\varepsilon_{i\mu\lambda}\Gamma_{i\mu j\nu}\varepsilon_{j\nu\lambda'} \tag{5.40}$$

We can constrain the separation and calculate the coupling matrix at incrementally smaller separations. This will allow us to relate the mixing of eigenstates during a collision to the time evolution of E_{λ} calculated in the previous subsection. We will thus show how the energy in each mode changes over time to dissipate kinetic energy, and then gain an understanding of the relationship between the magnitude of this dissipation and the coupling of modes between surfaces. The coupling of modes and the time evolution of E_{λ} in the presence of different adsorbates on the surface can be compared.

Though we have initially simulated collisions and dissipation between two surfaces of amorphous

silica and iron nanoparticles with and without adsorbates, in the future our group will also study dissipation in other relevant systems, such as in iron oxide clusters and in more complex silicates such as fayalite. We will use a mix of both molecular-dynamics and density functional theory to understand the effect of adsorbates on dissipation on an electronic scale. Additionally, as noted in chapter 6, this may be equally relevant to the study of nanotribology and the effect of adsorbates on dissipative mechanisms.

Results and Discussion

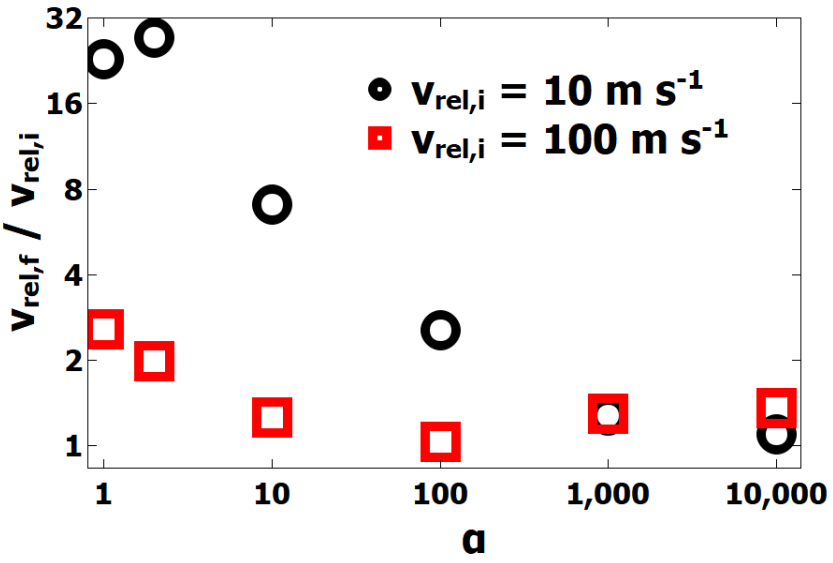

Figure 5.1: Maximum velocity normalized by kick velocity as a function of α for two different initial relative velocities.

First, we examine the maximum velocity, normalized by kick velocity, as a function of α for two different relative velocities. These normalized values are plotted in figure 5.1. For v_{rel} = 10 m s^{-1} with α = 100 specifically, the maximum velocity achieved was about 2.5 times its initial velocity, whereas the same initial velocity without a constraint force, v_{rel} = 10 m s^{-1} with α = 1, would

have resulted in a final collision velocity of about 250 m s^{-1}. Instead it only reaches a maximum of 25 m s^{-1}, an order of magnitude lower.

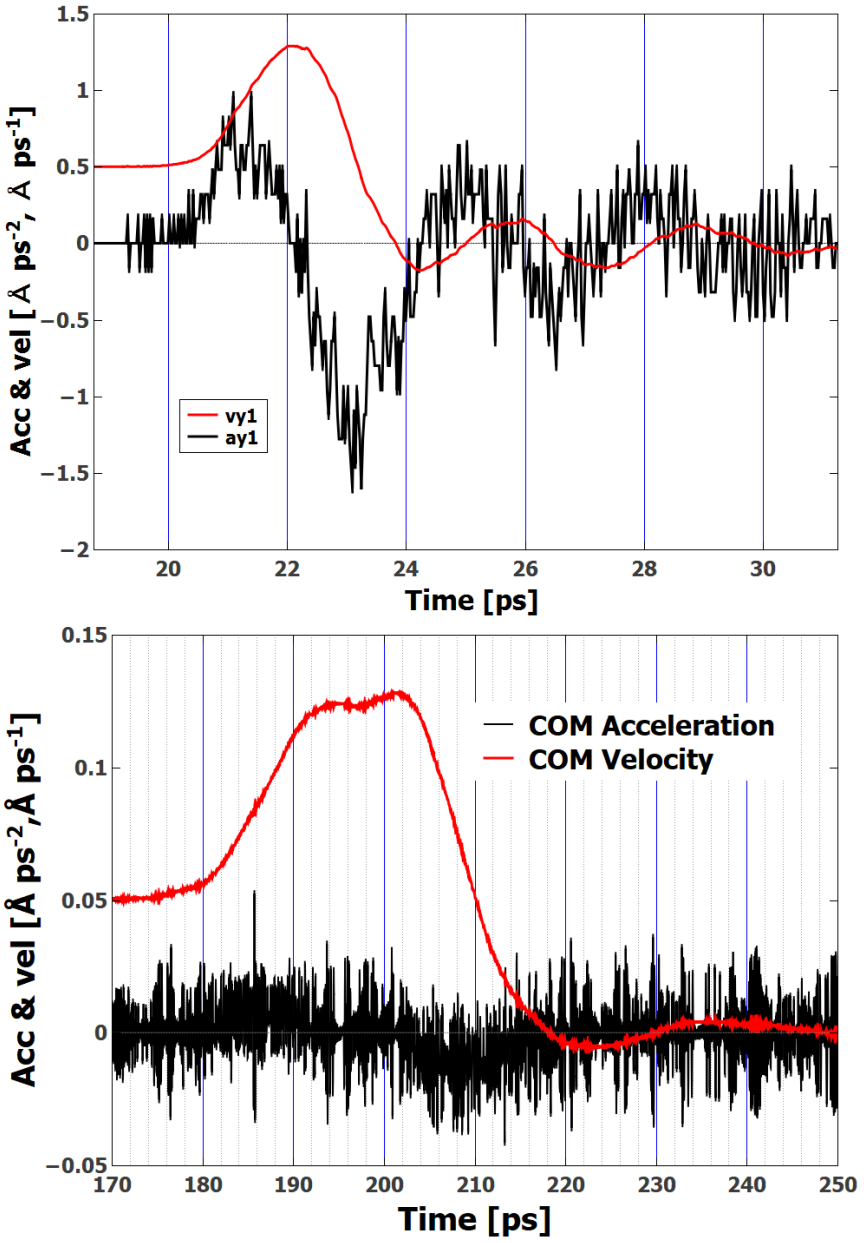

Figure 5.2: Acceleration and velocity of the center of mass of a nanoparticle as a collision occurs for v_{rel} = 100 m s^{-1} with α = 1 (TOP), and v_{rel} = 10 m s^{-1} with α = 100 (BOTTOM).

From this point forward, we will analyze and contrast results from two specific collision conditions:

v_{rel} = 100 m s^{-1} with α = 1, and v_{rel} = 10 m s^{-1} with α = 100.

First, the acceleration and velocity of the center of mass of a nanoparticle during a collision can be seen on the top in Fig. 5.2. At t = 5 ps (off-plot, to the left), an initial kick is given to each nanoparticle of 0.5 Å/ps (for v_{rel} = 100 m s^{-1}). Around t = 20.5 ps, the surfaces of the two colliding nanoparticles come into range of each other and start attracting each other. At t = 22 ps, the particles reach maximum velocity. From t = 22 ps to t =23.5 ps, the particles crash into each other and compress, coming to a full stop at t = 23.5 ps. They then rebound and (unsuccessfully) attempt to separate, reaching maximum neck stretch at t = 25 ps. There follow a series of ever-reducing oscillations as the kinetic energy is dissipated into finer-grained modes than just whole-particle oscillations. On the bottom of Fig. 5.2, roughly the same behavior occurs. The initial kick velocity of 0.05 Å ps^{-1} (for v_{rel} = 10 m s^{-1}) with a alpha value α = 100 leads to less inter-surface acceleration. Maximum velocity is reached at about 202 ps, maximum compression occurs at about 218 ps, and maximum tension occurs at about 223 ps.

In Fig. 5.3, we have plotted the maximum single-particle eigenfrequency as a function of time for both collision conditions. This is instructive as it shows when the structure of a nanoparticle becomes deformed beyond elastic deformation - i.e., when specific plastic deformation events occur. Looking at the left-hand figure, until about t = 22.5 ps, the maximum frequency is relatively stable, as the only interactions occurring are the pre-collision attraction and the beginnings of the particles deforming into each other. Around t = 23 ps to t = 23.5 ps, as maximum compression is reached, enough plastic deformation occurs such that a new maximum eigenfrequency of around 12 THz becomes present. Then just after the maximum neck stretch and rebound, another significant plastic deformation event occurs which shifts the maximum eigenfrequency to around 12.5 THz. From this point forward the system becomes relatively stable in terms of significant deformations of positions.

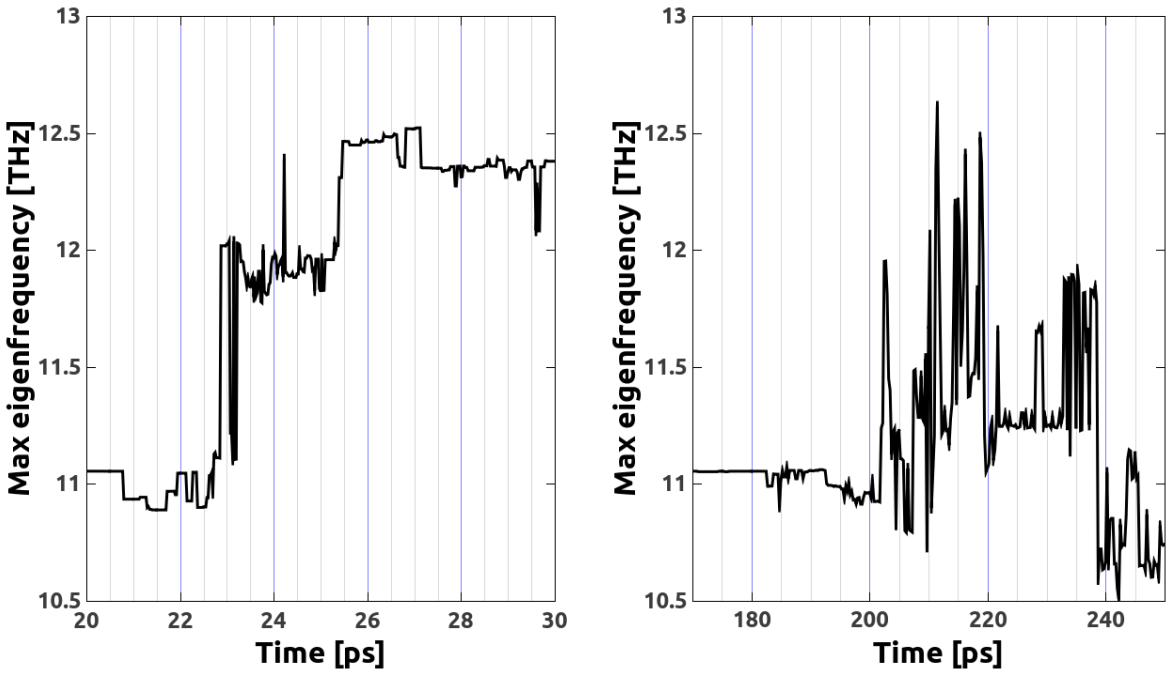

Figure 5.3: Maximum single-particle eigenfrequency as a function of time for v_{rel} = 100 m s^{-1} with α = 1 (LEFT), and v_{rel} = 10 m s^{-1} with α = 100 (RIGHT).

In contrast, the behavior evident on the right hand plot of Fig. 5.3 which involves a slower collision due to a constraint force shows a somewhat different story. In essence, it suffers even more plastic deformation than the faster collision. At first, this seems counter-intuitive, as the collision velocity is reduced, until one considers the nature of the constraint force. It is applied at every timestep. Therefore, as the particles begin to deform into each other leading towards the first compression, the resistant force which slows them down is actually suppressed with α = 100. In the same way, upon rebound, when maximum tension is reached and the neck attempts to break, forces trying to hold this neck together are suppressed by a constraining force. Interestingly, this means that these nanoparticles are now behaving as if they were nanoscale asperities on a much larger particle. In the same way in which nanoasperities are thought to be responsible for reduced contact area during friction processes, in the same way surface roughness of a micron-scale nanoparticle must

lead to specific nanoasperities colliding. This point was hypothesized in chapter 3 and actually seems to be partially confirmed here: that, with larger nanoparticle collisions, stress and therefore plastic deformation at the contact side will be enhanced with increasing particle mass, as the entire translational momentum of that large nanoparticle must now be dissipated via nanoscale asperities.

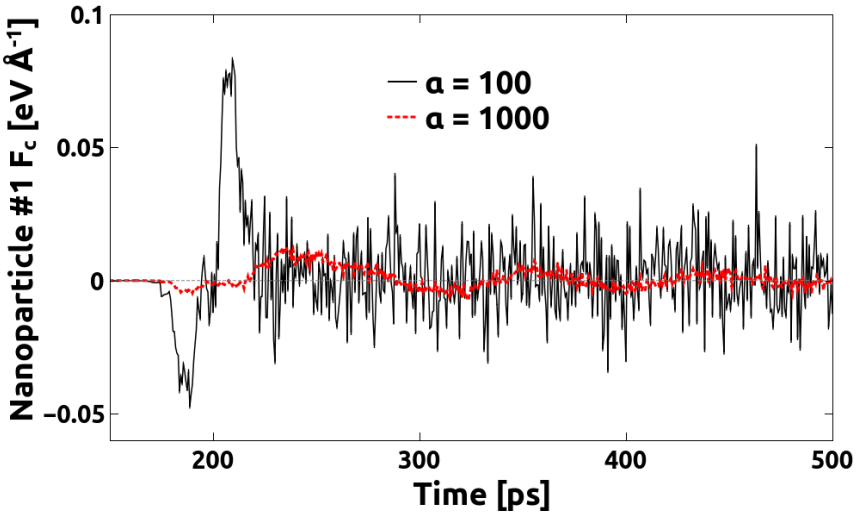

Figure 5.4: Inter-particle interaction forces as a function of time for two values of α.

It is also instructive to look at the interaction forces between the particles, as they are a key part of the approximation used in Eqn. 5.28. These forces are plotted in Fig. 5.4 for two values of α. Now we examine in detail the plot for the value α = 100. As the particle approach each other, they are subject to inter-surface attraction and therefore accelerate towards each other. However, here, we see that there is a corresponding constraint force acting upon the nanoparticle and reducing its acceleration up until about t = 200 ps. This corresponds to the maximum velocity condition from figure 5.2, bottom. Recalling the other conditions of maximum compression occurs at about 218 ps, and maximum tension at about 223 ps, followed by equilibration, we see at approximately this point the constraint force is oscillating around 0. However, it continues to modify the motion as described in the above paragraph, as if additional mass were behind an asperity.

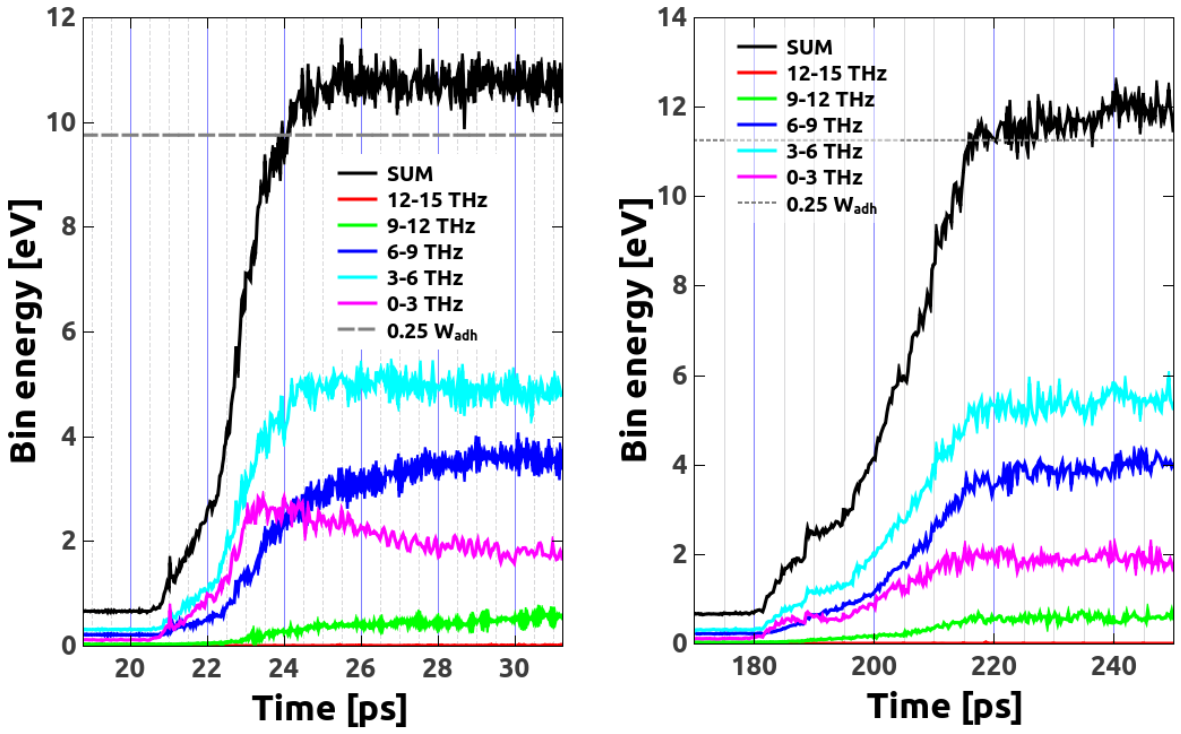

Figure 5.5: Per-mode kinetic energy, summed into 3 THz-wide bins, as a function of time for a nanoparticle collision for v_{rel} = 100 m s^{-1} with α = 1 (LEFT), and v_{rel} = 10 m s^{-1} with α = 100 (RIGHT).

Direct Calculation of Per-Mode Kinetic Energies via Atomic Velocities

The results presented in this subsection are calculated via the math in subsection 5. The data plotted in Fig. 5.5 present the kinetic energy as a function of time, for all the modes in a nanoparticle, aside from whole-particle translational and rotational modes, as a function of collision time for two different velocities and values of alpha. We first look at the left-hand figure, where v_{rel} = 100 m s^{-1} and α = 1. Before the time t = 22 ps, inter-surface attraction has already begun to not only accelerate the nanoparticles towards each other, as seen in the chapter 3, but has also begun to pump a modest amount of kinetic energy ($\sim$ 2 eV, roughly 10% of this nanoparticle's share of the W_{adh}) into non-translational modes. From the maximum-velocity time at t = 22 ps, to the

maximum-compression time at roughly t = 23.5 ps, a linear growth in dissipated kinetic energy as a function of time is observed. Note that at this point, when an attempt at a bounce has not yet started, 90% of the kinetic half of the W_{adh} to be dissipated has already been dissipated. As the rebound attempt occurs, from maximum compression to maximum tension at t = 25 ps, some 1 eV more is dissipated. Taking this roughly $\sim$ 10 eV of dissipated energy into kinetic modes in one particle as a 1/4 share of the total energy for both particles' normal modes, one sees that the $\sim$ 40 eV total dissipated into normal modes correlations well to the work of adhesion of this collision, W_{adh} = 38 eV. We next examine the right side of figure 5.5. For this collision, where v_{rel} = 10 m s^{-1} and α = 100, the same story emerges. For this collision, W_{adh} for both particles is about 45 eV and the direct kinetic method accounts well for 1/4 of this energy.

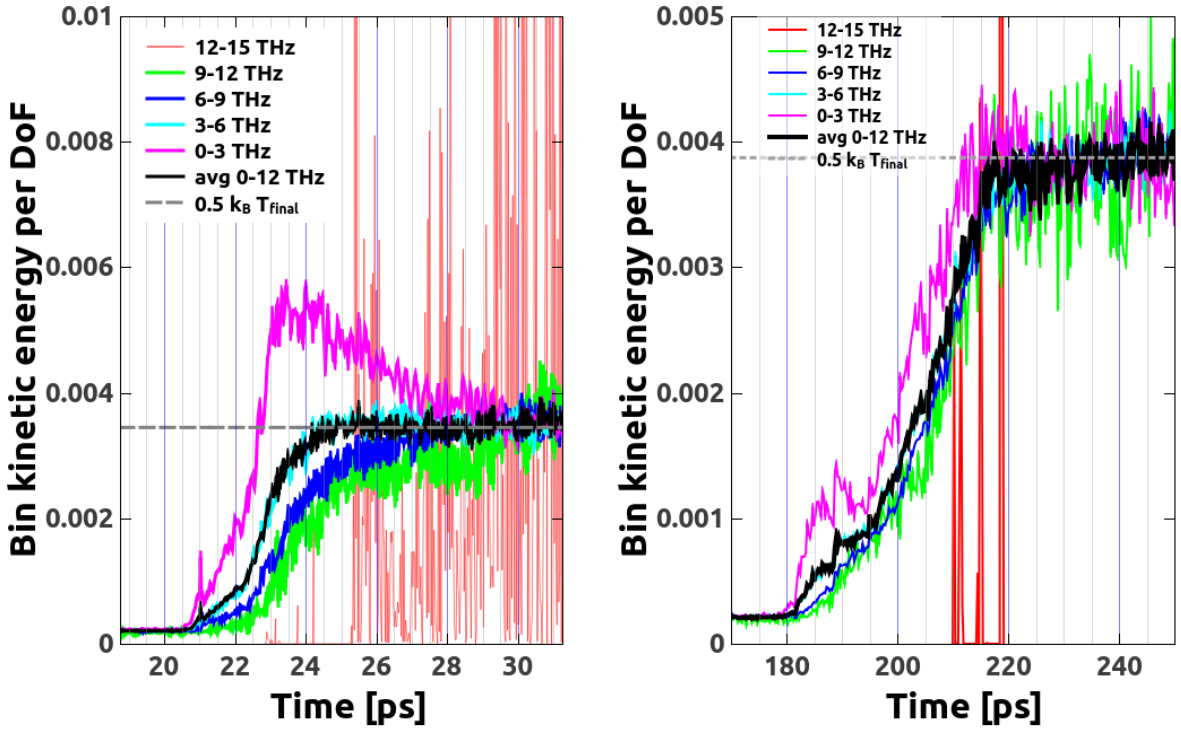

Figure 5.6: Per-mode kinetic energy, summed into 3 THz-wide bins and divided by the degrees of freedom per bin, as a function of time for a nanoparticle collision for v_{rel} = 100 m s^{-1} with α = 1 (LEFT), and v_{rel} = 10 m s^{-1} with α = 100 (RIGHT).

Next, the data plotted in Fig. 5.6 shows the kinetic energy per degree of freedom plotted as a function of time for the same two collisions. By dividing the kinetic energy in each 3 THz-wide bin by the density of states, one can elucidate which specific frequency ranges are most disproportionately responsible for the dissipation of the collision's translational kinetic energy. First, it is apparent that the timescale for all modes to equilibrate is about 5 to 6 ps. Here, we observe that the lowest frequency bin is most responsible for the dissipation of kinetic energy. This bin is also associated with the longest-wavelength normal modes, i.e., whole-particle and larger wavelength oscillations. As the normal modes increase in frequency, their proportional energies decrease. Eventually the energies equilibrate to those expected from energy equipartition into degrees of freedom. The wildly oscillating red lines are due to the fact that there are very few modes in the highest frequency bin, and that these frequencies change often. Their total contribution to the energy is negligible.

Per-Mode Power Approximation

We now proceed to the results of the power approximation. The powers plotted and reported in this subsection are directly calculated with equation 5.28. The data plotted in Fig. 5.7 presents power summed into 3 THz-wide bins. The most apparent feature is the bump from t = 22 ps (maximum center-of-mass velocity) to t = 23.5 ps (maximum compression). One can immediately see that the highest power levels are attained by the lowest frequency bins, which also correspond to the longest wavelength oscillations. Participation by middle frequencies is moderate. One can also see that the high-frequency bins are relatively unpopulated, but eventually these bins exhibit power as well, as thermal equilibrium is reached.

Figure 5.8 shows the energy in each bin as a function of time for both collision conditions. The energies attained by this method as substantially higher than those of the direct kinetic mode, but an argument can be made as to their cause. Here, we are using only interaction forces and atomic

velocities to determine per-mode power and are ignoring anharmonic effects. However, in these specific collisions, a sufficient amount of plastic deformation occurs, wherein strong anharmonic effects must occur as individual particles are nowhere near the bottom of their equivalent local, relaxed, and equilibrated potential energy surfaces.

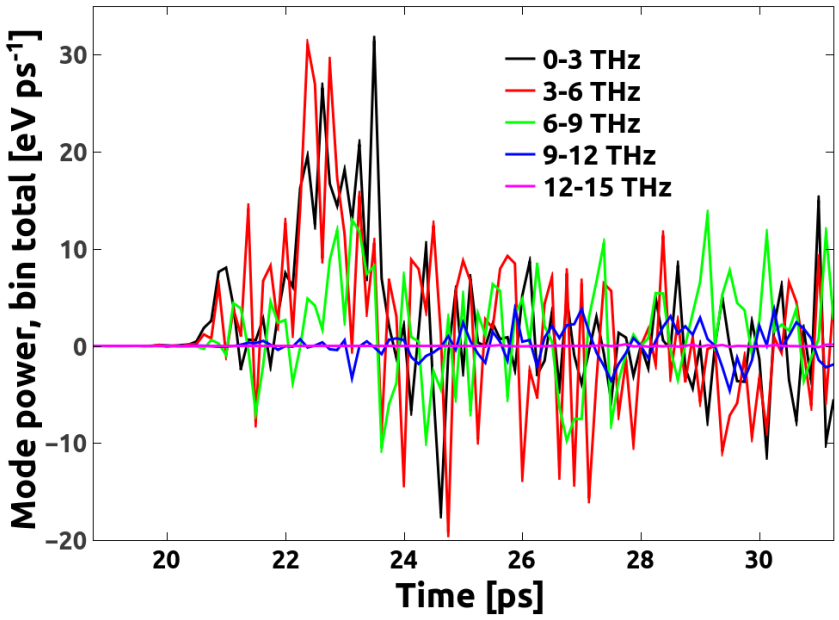

Figure 5.7: Power (in 3 THz-wide bins) as a function of time for a nanoparticle collision, where the parameters of the collision are v_{rel} = 100 m s^{-1} with $\alpha = 1$.

In addition, transfer of power from modes is also not handled by this approximation. With the previous, direct kinetic energy calculations, energy in those excited modes will leak out to other modes. Additionally, plastic deformation acts not only as an energy sink but to change the eigenfrequencies and eigenvectors themselves. All of these contributions are picked up by the direct kinetic energy calculations. However, the power approximation does not account for these additional processes.

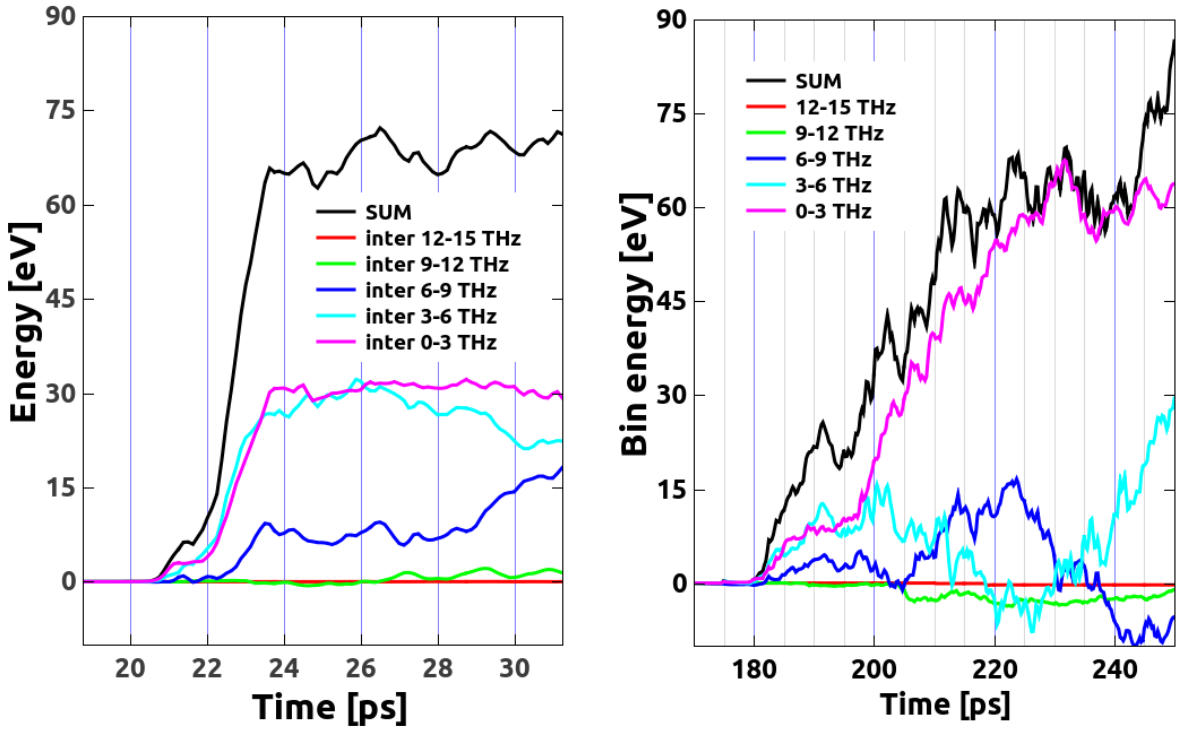

Figure 5.8: Integrated power (in 3 THz-wide bins) as a function of time for a nanoparticle collision for v_{rel} = 100 m s^{-1} with α = 1 (LEFT), and v_{rel} = 10 m s^{-1} with α = 100 (RIGHT).

With the power approximation (equation 5.28), modes will continue to accrue energy without loss, as per-mode power exists and is integrated, but will not decrease due to leaking and plastic deformation. For both collisions studied in detail, the same trend can be observed in terms of which modes receive the most energy. Up until compression and substantial plastic deformation, the two lowest frequency bins receive the majority of power. The medium frequency bin receives relatively little, and the highest frequency bins even less. After maximum compression and its consequent plastic deformation, the behaviors deviate, but this is promising in that it seems to describe dissipation well prior to plastic deformation.

Though these collisions were run in a constant energy regime, the parameter α is a direct modification to the system's forces, and thus will affect the total energy. The total energy drift (caused

by $\alpha > 1$) is reported in table 5.1. Total energy values were taken from completely equilibrated post-collided systems. Energy drift grows with alpha linearly with a confidence value of 0.9995. This makes sense because it is a constant modification to the total force, and thus will just be a constant energy factor when integrating those forces. The most important thing here is to note the energy drifts for $\alpha = 100$ and $\alpha = 1$, which is a difference of ~ 6 eV, comparable to the difference in total energies between the two systems.

Table 5.1: Total energy drift as a function of α

α	Energy drift [eV]
1	0
10	4.531
100	5.974
1,000	23.86
10,000	199.4

A Note on Nanotribology and Density Functional Theory

Here, have analyzed nanoparticle collisions, but this model can just as easily be used in a variety of dissipative contexts including nanotribology. Although tribology is usually focused on understanding adhesion and sliding friction including wear, the effect of surface adsorbates and lubricants in dissipation,[39] in a broader sense it builds upon surface chemistry, which we have already demonstrated should be relevant for dissipation in inter-grain collisions. In addition to the previously noted links to tribology, Judith Harrison showed that radical sites on the surface of diamond can lead to increased wear and friction.[123] Specifically, atomic-scale surface interactions, mediated primarily by strong chemical bonding, are responsible for dissipation of translational kinetic energy during a collision event, which is a requirement for grain aggregation. Building upon chapter3, in this chapter two different head-on collisions of iron nanoparticles were represented as a series of harmonic oscillators to elucidate dissipative behaviors. This harmonic oscillator representation

itself bears some resemblance to tribology models. This connection will be further explored in chapter 6.

This model also opens the door to even more detailed examinations of dissipation in general. Using density functional theory (DFT) to model these interfacial interactions required working out this methodology, which has been confirmed by these molecular-dynamics results. Thus, in addition to using MD to compute the time evolution of the energy in each mode and the coupling of modes between interacting surfaces, it is also possible to use DFT. Though MD, and classical molecular dynamics in general, has the advantage of being able to model many hundreds or even thousands of atoms during a collision for picoseconds to nanoseconds, DFT can more accurately describe charge transfer and thus chemistry. Likewise, though DFT is far more computationally expensive, it has the advantage of being an *ab initio* method and therefore does not require the development of a potential parameter set for every system.

CHAPTER 6: CONCLUSIONS

This specific focus of this dissertation is the chemistry and dissipation possible due to varying states of surface chemistry of mineral surfaces specific to the space environment. These unpassivated, high-energy surfaces, of which iron is a prime example, exhibit strong dissipative effects and thus are a model surface for the study of dissipation.

First, in chapter 2, the mineral olivine, when exposed to conditions specific to the space environment, exhibited growth of nanophase iron which was found to be strongly catalytic for the decomposition of ammonia and the build-up of complex hydrogen-terminated sp^2-bonded carbon features such as nanotubes and nanohorns. In elucidating the strong catalytic effect of space-weathered surfaces, we showed how simple volatiles can be built up into more complex species on mineral surfaces in space. This is a specific mechanism to synthesize and process organics in space, and establishes a clear connection between space weathering and organic chemistry.

Next, in chapter 3, we examined the head-on collisions of amorphous iron nanoparticles of radii R = 1.4 nm to R = 11 nm, and found that at all velocities and sizes simulated, sticking always occurred. Inter-surface attraction resulted in higher collision velocities, which in turn drove strong plastic deformation and other dissipation on a timescale much shorter than that of possible rebound. Additionally, we showed that the increasing contact area with collision velocity is due to plastic deformation, and that most of the adhesion energy can be explained by the healing of surfaces on the nanoparticles. We showed that as a model mineral surface, iron exhibits very strong dissipation at the nanoscale. Thus, we can conclude that not only can these mineral surfaces process organics on their surfaces, they can also strongly interact with other surfaces. In general, it is clear that the surface state of these mineral surfaces is important both chemically and in a dissipative manner.

We then examined the effect of radical organic chemistry on collisions of the smallest of these sim-

ulated nanoparticles in chapter 4. This further solidified the connection between our experiment and chapter 3. We found that at lower velocities the reduction in surface energy led to a modest reduction of the work of adhesion, thus affecting dissipation in one manner. However, at higher velocities, the dissipation of increased translational kinetic energy leads to heating of the underlying iron nanoparticle, which drives hydrogen dissociation from adsorbates, leading to H_2 formation on the surface and subsequent desorption and another possible dissipation mechanism. This process of course bears resemblance to the well-known Langmuir-Hinshelwood mechanism,[124] wherein two different pieces of a stable molecule diffuse towards each other, bond, and desorb from a surface. Additionally, we observed carbon bonding on a modest scale on a timescale of 40 ps. Additional surface diffusion of both C and H atoms may then lead to the formation of even larger species. All of these mechanisms show that mineral surfaces are chemically, catalytically, and dissipatively active, with intricate interactions that are not simply explained.

Finally, in chapter 5, we examined dissipation in bare iron nanoparticle collisions in terms of a new model which estimates per-mode power from inter-surface interactions and atomic velocities only. If no significant deformations of the surfaces occur, this model accounts well for the growth and population into normal modes. It was compared to a direct calculation of mode kinetic energies and was found to follow the same trends in terms of frequency preference prior to and during a collision.

There have of course been other molecular-dynamics simulations of nanoparticles in the past. Some are simply concerned with nanoparticle structure itself, while others simulate collisions, but restrict inter-particle interactions to be purely repulsive and/or use simpler Lennard-Jones pair potentials, or crystalline nanoparticles in contrast to our amorphous nanoparticles. Two specific articles we wish to compare our results to in particular are Nietiadi et al., 2017,[108] and Nietiadi et al., 2019.[125] In these works, analysis of crystalline nanoparticle collisions simulated with a Lennard-Jones pair potential elucidates the role of defect generation in dissipation in both bounc-

ing and sticking behavior. Interestingly, they find that sticking behavior can change qualitatively depending on the relative orientation of which specific facets come into contact. This orientational dependence has important relevance for our work. Our embedded-atom MD simulations always exhibited sticking, but our surfaces are not faceted but instead amorphous, and Nietiadi et al. have found that two [100] type surfaces will always stick during a collision, while a [100] surface colliding with a [110] will exhibit bouncing in a certain range of velocities.[125] In our collisions, our amorphous surfaces are approximately locally flat, and do not exhibit any sharp edges or corners. Thus our observation of constant sticking is in fact consistent with their findings.

The studies contained within this work, as well as previous coauthored work,[41] all demonstrate a strong dependence of surface chemistry on dissipation. In particular, metal surfaces with large surface energy and many dangling bonds exhibit particularly strong dissipation and adhesion, which generally supports the idea that defects and unpassivated sites should have very different dissipative properties than passivated minerals on the earth.

Turning to other dissipation mechanisms, summed up quite well by Brilliantov in 2007,[100] we first address elastic strain energy. We showed in chapter 3 that elastic-type contributions to adhesion energies are not present for any velocities or nanoparticle sizes simulated. Here Brilliantov provides a description of the visco-elastic mechanism for dissipating collision energy. In his derivation, for this mechanism to apply, the timescale of the collision must be much longer than the timescale of dissipative mechanisms - yet in all of our collisions that has not applied. We provided an estimate of when this may apply in the conclusions of chapter 3, by extrapolating from time constants extrapolated to represent precisely these quantities— the timescale of the collision vs. the timescale of dissipative mechanisms— and showed that at the nanoscale this is not assured. Additionally, even when simulating the effects of increased mass behind a nanoparticle, and thus simulating a nanoasperity on a much larger particle, even more plastic deformation was observed. Therefore this visco-elastic contribution is not very relevant for our collisions, and may not be for much

larger sizes. Additionally, the assumption is made that prior to actual contact, no interaction forces at all apply. We have shown that this is certainly not the case - in fact interaction forces create an attractive potential which enhances adhesion.

In this work, many references have been made to friction. The first observations of what came to be called Amontons' law, where frictional force in the translating direction is linearly related to the force pushing down upon that object, were actually made by Leonardo Da Vinci.[126] However Da Vinci did not publish his work, and thus Amontons was rightly credited with the first public statement of the linear relationship between frictional force in the direction of translation and a normal force pushing the translating object down towards the surface upon which it is sliding.[127] One key consequence of this law is the independence of friction with respect to contact area; the friction coefficient only depends upon the ratio of two forces. After Tabor's key idea that sliding motion that does not induce wear must be dissipated by atomic vibrations,[128] which had actually been mentioned earlier as a possible mechanism by Tomlinson decades earlier,[129] various models were proposed to model this vibrational dissipation.

There are many models which represent surface atoms as point masses connected by springs to an underlying substrate. As there is usually considerable surface roughness on the nanoscale of two sliding objects, the specific field of nanotribology is quite active. Here, a simple model of nanoscale friction is the Prandtl-Tomlinson model,[130] wherein a point mass (or AFM tip) is dragged across a nanometer-scale periodic surface potential. In this model friction is characterized in terms of a frictional parameter $\eta \propto \frac{V_0}{k}$, balancing a potential energy V_0 and a spring constant k which determines the behavior of sliding friction and balances potential energy against stored spring energy from a nanoasperity adhering to the potential surface temporarily. If the potential energy contribution is larger than the energy that can be stored in the spring, then stick-slip behavior will be observed. Otherwise, smooth sliding friction will occur.

To the author's knowledge, at this time no specific attempt has been made to model dissipation in a mode-by-mode fashion, and to extend this model to both the collisional and frictional regime. Moving on towards generalized dissipation, we have been unable to find any dissipation models which account, mode-by-mode, for power or energies in normal modes. There are, of course, models with friction and dissipation in them, and this often amounts to a linear dependence of dissipation on velocity via a catch-all Langevin-type term. In fact, in nanotribology, Braun et al. reveal that the vast majority of nanotribology studies only apply Langevin damping to degrees of freedom perpendicular to the sliding direction, and that the specific value of the damping parameter is not particularly important.[131] Clearly, this is an oversimplification. We have shown that at mineral surfaces, chemistry and dissipation are not homogeneous, easily generalized phenomena.

One important point that must be made about the power approximation method is that it only depends on interaction forces and velocities. This is a key feature of our derivation - it allows the application of this model to various conditions. For instance, though here we used molecular-dynamics to simulate atomic dynamics in a classical manner, one could just as easily use density functional theory (DFT) to calculate interaction forces. If the atoms on one surface are given a thermal distribution of velocities, one could study the coupling across the surface with the math derived in chapter 5, subsection 5. Various adsorbates and other surface features could be added and via relatively simple DFT calculations, a widespread survey could be done of the effect of adsorbates upon dissipation in general. Additionally, these calculations will subject atoms to only harmonic conditions, and therefore the anharmonic effects described in chapter 5 will be obviated. Densities of state will be relatively stable and can thus be sampled instead of calculated directly via the diagonalization method.

This is a specific goal of the research group in which the author works, and this book is the first step towards that goal. Here, I have shown that this model describes dissipation in a microscopic manner, and that inter-surface interactions are the key to describing dissipation in general, whether

it be in a tribological or collisional context.

APPENDIX A: COPYRIGHT NOTICES

Both chapters which contain previously published work were published in journals owned by the Elsevier corporation. Elsevier explicitly gives permission for use of published journal articles (PJAs) in dissertations for authors:

> "Authors can include their articles in full or in part in a thesis or dissertation for non-commercial purposes."

and

> "Theses and dissertations which contain embedded PJAs as part of the formal submission can be posted publicly by the awarding institution with DOI links back to the formal publications on ScienceDirect."

LIST OF REFERENCES

[1] P. L. Walker. Carbon: An old but new material revisited. *Carbon*, 28(2):261–279, 1990.

[2] Robert M. Hazen and Dimitri A. Sverjensky. Mineral surfaces, geochemical complexities, and the origins of life. *Cold Spring Harbor Perspectives in Biology*, 2(5), 2010.

[3] A. Negron-Mendoza, G. Albarran, and S. Ramos-Bernal. *Clays as Natural Catalyst in Prebiotic Processes*. Springer Netherlands, Dordrecht, 1996.

[4] Arno de Klerk. *FischerTropsch Process*. American Cancer Society, 2013.

[5] Reza M. Malek Abbaslou, Ahmad Tavassoli, Jafar Soltan, and Ajay K. Dalai. Iron catalysts supported on carbon nanotubes for Fischer-Tropsch synthesis: Effect of catalytic site position. *Applied Catalysis A: General*, 367(12):47–52, 2009.

[6] Edward Anders, Ryoichi Hayatsu, and Martin H. Studier. Catalytic reactions in the solar nebula: Implications for interstellar molecules and organic compounds in meteorites. *Origins of life*, 5(1):57–67, 1974.

[7] AGGM Tielens. The molecular universe. *Reviews of Modern Physics*, 85(3):1021, 2013.

[8] David S Meier and Jean L Turner. Spatially resolved chemistry in nearby galaxies. i. the center of ic 342. *The Astrophysical Journal*, 618(1):259, 2005.

[9] T Kudo, A Kouchi, M Arakawa, and H Nakano. The role of sticky interstellar organic material in the formation of asteroids. *Meteoritics & Planetary Science*, 37(12):1975–1983, 2002.

[10] Michael A DiSanti and Michael J Mumma. Reservoirs for comets: Compositional differences based on infrared observations. *Space Science Reviews*, 138(1-4):127–145, 2008.

[11] Jacques Crovisier, Nicolas Biver, Dominique Bockelée-Morvan, Jérémie Boissier, Pierre Colom, and Dariusz C Lis. The chemical diversity of comets: synergies between space exploration and ground-based radio observations. *Earth, Moon, and Planets*, 105(2-4):267–272, 2009.

[12] Zita Martins, Oliver Botta, Marilyn L. Fogel, Mark A. Sephton, Daniel P. Glavin, Jonathan S. Watson, Jason P. Dworkin, Alan W. Schwartz, and Pascale Ehrenfreund. Extraterrestrial nucleobases in the murchison meteorite. *Earth and Planetary Science Letters*, 270(12):130–136, 2008.

[13] Michael P. Callahan, Karen E. Smith, H. James Cleaves, Josef Ruzicka, Jennifer C. Stern, Daniel P. Glavin, Christopher H. House, and Jason P. Dworkin. Carbonaceous meteorites contain a wide range of extraterrestrial nucleobases. *Proceedings of the National Academy of Sciences*, 108(34):13995–13998, 2011.

[14] MC De Sanctis, E Ammannito, HY McSween, A Raponi, S Marchi, F Capaccioni, MT Capria, FG Carrozzo, M Ciarniello, S Fonte, et al. Localized aliphatic organic material on the surface of ceres. *Science*, 355(6326):719–722, 2017.

[15] Patrick N Peplowski, Rachel L Klima, David J Lawrence, Carolyn M Ernst, Brett W Denevi, Elizabeth A Frank, John O Goldsten, Scott L Murchie, Larry R Nittler, and Sean C Solomon. Remote sensing evidence for an ancient carbon-bearing crust on mercury. *Nature Geoscience*, 9(4):273, 2016.

[16] Amanda R. Hendrix, Faith Vilas, and Jian-Yang Li. The uv signature of carbon in the solar system. *Meteoritics & Planetary Science*, 51(1):105–115.

[17] Mehmet Yesiltas and Yoko Kebukawa. Associations of organic matter with minerals in tagish lake meteorite via high spatial resolution synchrotron-based ftir microspectroscopy. *Meteoritics & Planetary Science*, 51(3):584–595.

[18] Robert J. Trumpler. Absorption of light in the galactic system. *Publications of the Astronomical Society of the Pacific*, 42:214, aug 1930.

[19] J. B. Pollack, D. Hollenbach, S. Beckwith, D. P. Simonelli, T. Roush, and W. Fong. Composition and radiative properties of grains in molecular clouds and accretion disks. *The Astrophysical Journal*, 421:615–639, February 1994.

[20] Willy Benz. Low velocity collisions and the growth of planetesimals. *Space Science Reviews*, 92(1):279–294, 2000.

[21] Guillermo Stenborg, Johnathan R. Stauffer, and Russell A. Howard. Evidence for a circumsolar dust ring near mercury's orbit. *The Astrophysical Journal*, 868(1):74, nov 2018.

[22] David Nesvorný, Peter Jenniskens, Harold F. Levison, William F. Bottke, David Vokrouhlický, and Matthieu Gounelle. COMETARY ORIGIN OF THE ZODIACAL CLOUD AND CARBONACEOUS MICROMETEORITES. IMPLICATIONS FOR HOT DEBRIS DISKS. *The Astrophysical Journal*, 713(2):816–836, mar 2010.

[23] Daniel J Scheeres, Christine M Hartzell, Paul Sánchez, and Micheal Swift. Scaling forces to asteroid surfaces: The role of cohesion. *Icarus*, 210(2):968–984, 2010.

[24] Paul Sánchez and Daniel J Scheeres. The strength of regolith and rubble pile asteroids. *Meteoritics & Planetary Science*, 49(5):788–811, 2014.

[25] Jürgen Blum and Gerhard Wurm. The growth mechanisms of macroscopic bodies in protoplanetary disks. *Annual Review of Astronomy and Astrophysics*, 46(1):21–56, 2008.

[26] Koji Wada, Hidekazu Tanaka, Toru Suyama, Hiroshi Kimura, and Tetsuo Yamamoto. COLLISIONAL GROWTH CONDITIONS FOR DUST AGGREGATES. *The Astrophysical Journal*, 702(2):1490–1501, aug 2009.

[27] Paszun, D. and Dominik, C. Numerical determination of the material properties of porous dust cakes. *A&A*, 484(3):859–868, 2008.

[28] Andras Zsom, CW Ormel, C Güttler, J Blum, and CP Dullemond. The outcome of protoplanetary dust growth: pebbles, boulders, or planetesimals?-ii. introducing the bouncing barrier. *Astronomy & Astrophysics*, 513:A57, 2010.

[29] S Krijt, C Dominik, and A G G M Tielens. Rolling friction of adhesive microspheres. *Journal of Physics D: Applied Physics*, 47(17):175302, apr 2014.

[30] Jacob N Israelachvili. *Intermolecular and surface forces*. Academic press, 2011.

[31] George R. Carruthers. Atomic and molecular hydrogen in interstellar space. *Space Science Reviews*, 10(4):459–482, 1970.

[32] Le Bourlot, J., Le Petit, F., Pinto, C., Roueff, E., and Roy, F. Surface chemistry in the interstellar medium - i. h2 formation by langmuir-hinshelwood and eley-rideal mechanisms. *A&A*, 541:A76, 2012.

[33] Chapter 8 catalysis on the surfaces of bare dust grains, 2016.

[34] Koji Wada, Hidekazu Tanaka, Toru Suyama, Hiroshi Kimura, and Tetsuo Yamamoto. Numerical simulation of dust aggregate collisions. i. compression and disruption of two-dimensional aggregates. *The Astrophysical Journal*, 661(1):320, 2007.

[35] Güttler, C., Blum, J., Zsom, A., Ormel, C. W., and Dullemond, C. P. The outcome of protoplanetary dust growth: pebbles, boulders, or planetesimals? - i. mapping the zoo of laboratory collision experiments. *A&A*, 513:A56, 2010.

[36] Stefan Kothe, Jürgen Blum, René Weidling, and Carsten Güttler. Free collisions in a microgravity many-particle experiment. iii. the collision behavior of sub-millimeter-sized dust aggregates. *Icarus*, 225(1):75 – 85, 2013.

[37] K. L. Johnson, K. Kendall, and A. D. Roberts. Surface energy and the contact of elastic solids. *Proceedings of the Royal Society of London A: Mathematical, Physical and Engineering Sciences*, 324(1558):301–313, 1971.

[38] Anthony J. Barthel, Ala' Al-Azizi, Nicholas D. Surdyka, and Seong H. Kim. Effects of gas or vapor adsorption on adhesion, friction, and wear of solid interfaces. *Langmuir*, 30(11):2977–2992, mar 2014.

[39] Jacqueline Krim. Friction and energy dissipation mechanisms in adsorbed molecules and molecularly thin films. *Advances in Physics*, 61(3):155–323, 2012.

[40] Esteban Broitman. The nature of the frictional force at the macro-, micro-, and nano-scales. *Friction*, 2(1):40–46, Mar 2014.

[41] Abrar H Quadery, Baochi D Doan, William C Tucker, Adrienne R Dove, and Patrick K Schelling. Role of surface chemistry in grain adhesion and dissipation during collisions of silica nanograins. *The Astrophysical Journal*, 844(2):105, 2017.

[42] Gerhard Wurm, Georgi Paraskov, and Oliver Krauss. Growth of planetesimals by impacts at $\sim$25 m/s. *Icarus*, 178(1):253–263, nov 2005.

[43] Akbar D. Whizin, Jürgen Blum, and Joshua E. Colwell. The physics of protoplanetesimal dust agglomerates. viii. microgravity collisions between porous sio_2 aggregates and loosely-bound agglomerates. *ApJ*, 2017. In press.

[44] C. Dominik and A. G. G. M. Tielens. The physics of dust coagulation and the structure of dust aggregates in space. *ApJ*, 480(2):647–673, may 1997.

[45] Thomas P. Senftle, Sungwook Hong, Md Mahbubul Islam, Sudhir B. Kylasa, Yuanxia Zheng, Yun Kyung Shin, Chad Junkermeier, Roman Engel-Herbert, Michael J. Janik, Hasan Metin

Aktulga, Toon Verstraelen, Ananth Grama, and Adri C. T. van Duin. The reaxff reactive force-field: development, applications and future directions. *Npj Computational Materials*, 2:15011 EP –, Mar 2016. Review Article.

[46] Anant D. Kulkarni, Donald G. Truhlar, Sriram Goverapet Srinivasan, Adri C. T. van Duin, Paul Norman, and Thomas E. Schwartzentruber. Oxygen interactions with silica surfaces: Coupled cluster and density functional investigation and the development of a new ReaxFF potential. *J. Phys. Chem. C*, 117(1):258–269, jan 2013.

[47] Adri C. T. van Duin, Alejandro Strachan, Shannon Stewman, Qingsong Zhang, Xin Xu, and William A. Goddard. $ReaxFF_{SiO_2}$ reactive force field for silicon and silicon oxide systems. *J. Phys. Chem. A*, 107(19):3803–3811, may 2003.

[48] Joseph C. Fogarty, Hasan Metin Aktulga, Ananth Y. Grama, Adri C. T. van Duin, and Sagar A. Pandit. A reactive molecular dynamics simulation of the silica-water interface. *J. Chem. Phys.*, 132(17):174704, may 2010.

[49] Hiroshi Kimura, Koji Wada, Hiroki Senshu, and Hiroshi Kobayashi. Cohesion of amorphous silica spheres: Toward a better understanding of the coagulation growth of silicate dust aggregates. *ApJ*, 812(1):67, oct 2015.

[50] Abrar H. Quadery, Shaun Pacheco, Alan Au, Natalie Rizzacasa, Joshua Nichols, Timothy Le, Cameron Glasscock, and Patrick K. Schelling. Atomic-scale simulation of space weathering in olivine and orthopyroxene. *JGR: Planets*, 120(4):643–661, apr 2015.

[51] T. Noguchi, T. Nakamura, M. Kimura, M. E. Zolensky, M. Tanaka, T. Hashimoto, M. Konno, A. Nakato, T. Ogami, A. Fujimura, M. Abe, T. Yada, T. Mukai, M. Ueno, T. Okada, K. Shirai, Y. Ishibashi, and R. Okazaki. Incipient space weathering observed on the surface of Itokawa dust particles. *Science*, 333(6046):1121–1125, 2011.

[52] Michael J. Gaffey. Space weathering and the interpretation of asteroid reflectance spectra. *Icarus*, 209(2):564 – 574, 2010.

[53] William C. Tucker, Abrar H. Quadery, Alfons Schulte, Richard G. Blair, William E. Kaden, Patrick K. Schelling, and Daniel T. Britt. Strong catalytic activity of iron nanoparticles on the surfaces of reduced olivine. *Icarus*, 299:502–512, 2018.

[54] Kun Wang, Frédéric Moynier, Frank A. Podosek, and Julien Foriel. An iron isotope perspective on the origin of the nanophase metallic iron in lunar regolith. *Earth and Planetary Science Letters*, 337338:17 – 24, 2012.

[55] H.M. Kaluna, H.A. Ishii, J.P. Bradley, J.J. Gillis-Davis, and P.G. Lucey. Simulated space weathering of Fe- and Mg-rich aqueously altered minerals using pulsed laser irradiation. *Icarus*, pages –, 2016.

[56] Maho Yamada, Sho Sasaki, Hiroko Nagahara, Akira Fujiwara, Sunao Hasegawa, Hajime Yano, Takahiro Hiroi, Hideo Ohashi, and Hisashi Otake. Simulation of space weathering of planet-forming materials: Nanosecond pulse laser irradiation and proton implantation on olivine and pyroxene samples. *Earth, Planets and Space*, 51(11):1255–1265, 1999.

[57] P. Vernazza, R. P. Binzel, A. Rossi, M. Fulchignoni, and M. Birlan. Solar wind as the origin of rapid reddening of asteroid surfaces. *Nature*, 458(7241):993–995, 2009.

[58] Edward Anders. Organic matter in meteorites and comets: Possible origins. *Space Science Reviews*, 56(1):157–166, 1991.

[59] Erika L. Gibb, Michael A. DiSanti, Karen Magee-Sauer, Neil Dello Russo, Boncho P. Bonev, and Michael J. Mumma. The organic composition of C/2001 A2 (LINEAR): II. Search for heterogeneity within a comet nucleus. *Icarus*, 188(1):224 – 232, 2007.

[60] F. Capaccioni, A. Coradini, G. Filacchione, S. Erard, G. Arnold, P. Drossart, M. C. De Sanctis, D. Bockelee-Morvan, M. T. Capria, F. Tosi, C. Leyrat, B. Schmitt, E. Quirico, P. Cerroni, V. Mennella, A. Raponi, M. Ciarniello, T. McCord, L. Moroz, E. Palomba, E. Ammannito, M. A. Barucci, G. Bellucci, J. Benkhoff, J. P. Bibring, A. Blanco, M. Blecka, R. Carlson, U. Carsenty, L. Colangeli, M. Combes, M. Combi, J. Crovisier, T. Encrenaz, C. Federico, U. Fink, S. Fonti, W. H. Ip, P. Irwin, R. Jaumann, E. Kuehrt, Y. Langevin, G. Magni, S. Mottola, V. Orofino, P. Palumbo, G. Piccioni, U. Schade, F. Taylor, D. Tiphene, G. P. Tozzi, P. Beck, N. Biver, L. Bonal, J.-Ph. Combe, D. Despan, E. Flamini, S. Fornasier, A. Frigeri, D. Grassi, M. Gudipati, A. Longobardo, K. Markus, F. Merlin, R. Orosei, G. Rinaldi, K. Stephan, M. Cartacci, A. Cicchetti, S. Giuppi, Y. Hello, F. Henry, S. Jacquinod, R. Noschese, G. Peter, R. Politi, J. M. Reess, and A. Semery. The organic-rich surface of comet 67P/Churyumov Gerasimenko as seen by VIRTIS/Rosetta. *Science*, 347(6220), 2015.

[61] Fred Goesmann, Helmut Rosenbauer, Jan Hendrik Bredehöft, Michel Cabane, Pascale Ehrenfreund, Thomas Gautier, Chaitanya Giri, Harald Krüger, Léna Le Roy, Alexandra J. MacDermott, Susan McKenna-Lawlor, Uwe J. Meierhenrich, Guillermo M. Muñoz Caro, Francois Raulin, Reinhard Roll, Andrew Steele, Harald Steininger, Robert Sternberg, Cyril Szopa, Wolfram Thiemann, and Stephan Ulamec. Organic compounds on comet 67P/Churyumov-Gerasimenko revealed by COSAC mass spectrometry. *Science*, 349(6247), 2015.

[62] Nicolas Fray, Anaïs Bardyn, Hervé Cottin, Kathrin Altwegg, Donia Baklouti, Christelle Briois, Luigi Colangeli, Cécile Engrand, Henning Fischer, Albrecht Glasmachers, Eberhard Grün, Gerhard Haerendel, Hartmut Henkel, Herwig Höfner, Klaus Hornung, Elmar K. Jessberger, Andreas Koch, Harald Krüger, Yves Langevin, Harry Lehto, Kirsi Lehto, Léna Le Roy, Sihane Merouane, Paola Modica, François-Régis Orthous-Daunay, John Paquette, François Raulin, Jouni Rynö, Rita Schulz, Johan Silén, Sandra Siljeström, Wolfgang Steiger, Oliver Stenzel, Thomas Stephan, Laurent Thirkell, Roger Thomas, Klaus Torkar, Kurt Varmuza, Karl-Peter

Wanczek, Boris Zaprudin, Jochen Kissel, and Martin Hilchenbach. High-molecular-weight organic matter in the particles of comet 67P/Churyumov-Gerasimenko. *Nature*, advance online publication, 2016.

[63] Jeffrey J. Gillis-Davis, Paul G. Lucey, John P. Bradley, Hope A. Ishii, Heather M. Kaluna, Anumpam Misra, and Harold C. Connolly Jr. Incremental laser space weathering of Allende reveals non-lunar like space weathering effects. *Icarus*, pages –, 2017.

[64] Robert M. Hazen and Dimitri A. Sverjensky. Mineral Surfaces, Geochemical Complexities, and the Origins of Life. *COLD SPRING HARBOR PERSPECTIVES IN BIOLOGY*, 2(5), MAY 2010.

[65] Munga C. Bahome, Linda L. Jewell, Diane Hildebrandt, David Glasser, and Neil J. Coville. Fischer-Tropsch synthesis over iron catalysts supported on carbon nanotubes. *Applied Catalysis A: General*, 287(1):60–67, 2005.

[66] Laszlo Guczi, G. Stefler, O. Geszti, Zs Koppany, Z. Konya, E Molnar, M. Urban, and I. Kiricsi. CO hydrogenation over cobalt and iron catalysts supported over multiwall carbon nanotubes: Effect of preparation. *Journal of Catalysis*, 244(1):24–32, 2006.

[67] Sara Faiz Hanna Tasfy, Noor Asmawati Mohd Zabidi, and Duvvuri Subbarao. Performance Characterization of Supported Iron Nanocatalysts for Fischer-Tropsch Synthesis. *Journal of Materials Science and Engineering. A*, 1(1A):9, 2011.

[68] Sergio Rapagnà, Mirella Virginie, Katia Gallucci, Claire Courson, Manuela Di Marcello, Alain Kiennemann, and Pier Ugo Foscolo. Fe/olivine catalyst for biomass steam gasification: Preparation, characterization and testing at real process conditions. *Catalysis Today*, 176(1):163–168, 2011.

[69] Scott A. Sandford, Jérôme Aléon, Conel M. O'D. Alexander, Tohru Araki, Sasa Bajt, Giuseppe A. Baratta, Janet Borg, John P. Bradley, Donald E. Brownlee, John R. Brucato, Mark J. Burchell, Henner Busemann, Anna Butterworth, Simon J. Clemett, George Cody, Luigi Colangeli, George Cooper, Louis D'Hendecourt, Zahia Djouadi, Jason P. Dworkin, Gianluca Ferrini, Holger Fleckenstein, George J. Flynn, Ian A. Franchi, Marc Fries, Mary K. Gilles, Daniel P. Glavin, Matthieu Gounelle, Faustine Grossemy, Chris Jacobsen, Lindsay P. Keller, A. L. David Kilcoyne, Jan Leitner, Graciela Matrajt, Anders Meibom, Vito Mennella, Smail Mostefaoui, Larry R. Nittler, Maria E. Palumbo, Dimitri A. Papanastassiou, François Robert, Alessandra Rotundi, Christopher J. Snead, Maegan K. Spencer, Frank J. Stadermann, Andrew Steele, Thomas Stephan, Peter Tsou, Tolek Tyliszczak, Andrew J. Westphal, Sue Wirick, Brigitte Wopenka, Hikaru Yabuta, Richard N. Zare, and Michael E. Zolensky. Organics Captured from Comet 81P/Wild 2 by the Stardust Spacecraft. *Science*, 314(5806):1720–1724, 2006.

[70] J. M. Sunshine, M. F. A'Hearn, O. Groussin, J.-Y. Li, M. J. S. Belton, W. A. Delamere, J. Kissel, K. P. Klaasen, L. A. McFadden, K. J. Meech, H. J. Melosh, P. H. Schultz, P. C. Thomas, J. Veverka, D. K. Yeomans, I. C. Busko, M. Desnoyer, T. L. Farnham, L. M. Feaga, D. L. Hampton, D. J. Lindler, C. M. Lisse, and D. D. Wellnitz. Exposed Water Ice Deposits on the Surface of Comet 9P/Tempel 1. *Science*, 311(5766):1453–1455, 2006.

[71] J. Fournelle. An Investigation of "San Carlos Olivine": Comparing USNM-distributed Material with Commercially Available Material. *Microscopy and Microanalysis*, 17:842–843, 07 2011. Copyright - Copyright l' Microscopy Society of America 2011; Last updated - 2015-08-15.

[72] Tomas Kohout, Jan Cuda, Jan Filip, Daniel Britt, Todd Bradley, Jiri TuCek, Roman Skala, Gunther Kletetschka, Josef Kaslik, Ondrej Malina, KarolIna Siskova, and Radek Zboril. Space weathering simulations through controlled growth of iron nanoparticles on olivine. *Icarus*, 237:75–83, 2014.

[73] K Barcova, M Mashlan, R Zboril, and P Martinec. Mössbauer study of transformation mechanism of fe cations in olivine after thermal treatments in air. *Journal of radioanalytical and nuclear chemistry*, 255(3):529–533, 2003.

[74] Rudy Michel, Mohamed Ramzi Ammar, Jacques Poirier, and Patrick Simon. Phase transformation characterization of olivine subjected to high temperature in air. *Ceramics International*, 39(5):5287–5294, 2013.

[75] RG Burns. Crystal field spectra and evidence of cation ordering in olivine minerals. *American Mineralogist*, 55(9-10):1608, 1970.

[76] Bruce Hapke. Space weathering from Mercury to the asteroid belt. *Journal of Geophysical Research: Planets*, 106(E5):10039–10073, 2001.

[77] E Ramanaidou, M Wells, I Lau, and C Laukamp. Characterization of iron ore by visible and infrared reflectance and, raman spectroscopies. pages 191–228, 2015.

[78] Richard P Binzel, Dmitrij F Lupishko, Mario Di Martino, Richard J Whiteley, and Gerhard J Hahn. Physical properties of near-earth objects. *Asteroids III*, 255:271, 2002.

[79] Hao Zhang, Yazhou Yang, Weidong Jin, Chujian Liu, and Weibiao Hsu. Effects of Spectralon absorption on reflectance spectra of typical planetary surface analog materials. *Opt. Express*, 22(18):21280–21291, Sep 2014.

[80] M Descostes, F Mercier, N Thromat, C Beaucaire, and M Gautier-Soyer. Use of XPS in the determination of chemical environment and oxidation state of iron and sulfur samples: constitution of a data basis in binding energies for fe and s reference compounds and applications to the evidence of surface species of an oxidized pyrite in a carbonate medium. *Applied Surface Science*, 165(4):288 – 302, 2000.

[81] Davoisne, C., Leroux, H., Frere, M., Gimblot, J., Gengembre, L., Djouadi, Z., Ferreiro, V., d'Hendecourt, L., and Jones, A. Chemical and morphological evolution of a silicate surface under low-energy ion irradiation. *A&A*, 482(2):541–548, 2008.

[82] Alexander G Shard. Detection limits in xps for more than 6000 binary systems using al and mg kα x-rays. *Surface and Interface Analysis*, 46(3):175–185, 2014.

[83] A. B. Kolesov and A. C. Geiger. A Raman spectroscopic study of Fe-Mg olivines. *Physics and Chemistry of Minerals*, 31(3):142–154, 2004.

[84] Walerian Arabczyk and Jacek Zamlynny. Study of the ammonia decomposition over iron catalysts. *Catalysis Letters*, 60(3):167–171.

[85] G. Ertl and M. Huber. Mechanism and kinetics of ammonia decomposition on iron. *Journal of Catalysis*, 61(2):537–539, 1980.

[86] W. Arabczyk and U. Narkiewicz. A new method for in situ determination of number of active sites in iron catalysts for ammonia synthesis and decomposition. *Applied Surface Science*, 196(14):423–428, 2002.

[87] Xuezhi Duan, Gang Qian, Xinggui Zhou, Zhijun Sui, De Chen, and Weikang Yuan. Tuning the size and shape of Fe nanoparticles on carbon nanofibers for catalytic ammonia decomposition. *Applied Catalysis B: Environmental*, 101(34):189–196, 2011.

[88] D. A. Cooper and E. B. Ljungstroem. Decomposition of ammonia over quartz sand at 840-960°C. *Energy & Fuels*, 2(5):716–719, 1988.

[89] A. C. Ferrari and J. Robertson. Resonant Raman spectroscopy of disordered, amorphous, and diamondlike carbon. *Phys. Rev. B*, 64:075414, Jul 2001.

[90] Mildred S. Dresselhaus, Ado Jorio, Mario Hofmann, Gene Dresselhaus, and Riichiro Saito. Perspectives on carbon nanotubes and graphene Raman spectroscopy. *Nano Letters*, 10(3):751–758, 2010. PMID: 20085345.

[91] C. Casiraghi, A. C. Ferrari, and J. Robertson. Raman spectroscopy of hydrogenated amorphous carbons. *Phys. Rev. B*, 72:085401, Aug 2005.

[92] Tao Ling, Lin Xie, Jing Zhu, Huimin Yu, Hengqiang Ye, Rong Yu, Zhiying Cheng, Li Liu, Li Liu, Guangwen Yang, Zhida Cheng, Yujia Wang, and Xiuliang Ma. Icosahedral face-centered cubic Fe nanoparticles: Facile synthesis and characterization with aberration-corrected TEM. *Nano Letters*, 9(4):1572–1576, 2009.

[93] Robert Hill. *Physical metallurgy principles*. PWS-Kent Pub, Boston, 1992.

[94] Xiaofeng Feng, See Wee Chee, Renu Sharma, Kai Liu, Xu Xie, Qunqing Li, Shoushan Fan, and Kaili Jiang. In situ TEM observation of the gasification and growth of carbon nanotubes using iron catalysts. *Nano Research*, 4(8):767–779, 2011.

[95] Ryoichi Hayatsu and Edward Anders. *Organic compounds in meteorites and their origins*. Springer Berlin Heidelberg, Berlin, Heidelberg, 1981.

[96] Hans Schulz, Klaus Beck, and Egon Erich. Mechanism of the Fischer Tropsch process. 36:457 – 471, 1988.

[97] Jordi Llorca and Ignasi Casanova. Formation of carbides and hydrocarbons in chondritic interplanetary dust particles: A laboratory study. *Meteoritics & Planetary Science*, 33(2):243–251, 1998.

[98] William C Tucker, Adrienne R Dove, and Patrick K Schelling. Dissipation and plastic deformation in collisions between metallic nanoparticles. *Computational Materials Science*, 161:215–222, 2019.

[99] S Krijt, C Güttler, D Heißelmann, C Dominik, and AGGM Tielens. Energy dissipation in head-on collisions of spheres. *Journal of Physics D: Applied Physics*, 46(43):435303, 2013.

[100] Nikolai V. Brilliantov, Nicole Albers, Frank Spahn, and Thorsten Pöschel. Collision dynamics of granular particles with adhesion. *Phys. Rev. E*, 76:051302, Nov 2007.

[101] Chuan yu Wu, Long yuan Li, and Colin Thornton. Rebound behaviour of spheres for plastic impacts. *International Journal of Impact Engineering*, 28(9):929 – 946, 2003.

[102] Sinisa Dj. Mesarovic and K.L. Johnson. Adhesive contact of elasticplastic spheres. *Journal of the Mechanics and Physics of Solids*, 48(10):2009 – 2033, 2000.

[103] Colin Thornton and Zemin Ning. A theoretical model for the stick/bounce behaviour of adhesive, elastic-plastic spheres. *Powder Technology*, 99(2):154 – 162, 1998.

[104] Arati Chokshi, AGGM Tielens, and D Hollenbach. Dust coagulation. *The Astrophysical Journal*, 407:806–819, 1993.

[105] Jürgen Blum. Experiments on sticking, restructuring, and fragmentation of preplanetary dust aggregates. *Icarus*, 143(1):138–146, jan 2000.

[106] Jürgen Blum and Michael Münch. Experimental investigations on aggregate-aggregate collisions in the early solar nebula. *Icarus*, 106(1):151–167, nov 1993.

[107] Torsten Poppe, Jürgen Blum, and Thomas Henning. Analogous experiments on the stickiness of micron-sized preplanetary dust. *Astrophys. J.*, 533(1):454–471, apr 2000.

[108] Maureen L Nietiadi, Philipp Umstätter, Tiffany Tjong, Yudi Rosandi, Emmanuel N Millán, Eduardo M Bringa, and Herbert M Urbassek. The bouncing threshold in silica nanograin collisions. *Physical Chemistry Chemical Physics*, 19(25):16555–16562, 2017.

[109] José Manuel Valverde Millán. *Fluidization of fine powders: cohesive versus dynamical aggregation*, volume 18. Springer Science & Business Media, 2012.

[110] Roberto Moreno-Atanasio, Simon J. Antony, and Richard A. Williams. Influence of interparticle interactions on the kinetics of self-assembly and mechanical strength of nanoparticulate aggregates. *Particuology*, 7(2):106 – 113, 2009. Manufacture and Structure of Functional Nanoparticles.

[111] Yu Guo and Jennifer Sinclair Curtis. Discrete element method simulations for complex granular flows. *Annual Review of Fluid Mechanics*, 47(1):21–46, 2015.

[112] Wei-xian Zhang. Nanoscale iron particles for environmental remediation: An overview. *Journal of Nanoparticle Research*, 5(3):323–332, Aug 2003.

[113] Steve Plimpton. Fast parallel algorithms for short-range molecular dynamics. *Journal of computational physics*, 117(1):1–19, 1995.

[114] MI Mendelev, S Han, DJ Srolovitz, GJ Ackland, DY Sun, and M Asta. Development of new interatomic potentials appropriate for crystalline and liquid iron. *Philosophical magazine*, 83(35):3977–3994, 2003.

[115] William Humphrey, Andrew Dalke, and Klaus Schulten. VMD – Visual Molecular Dynamics. *Journal of Molecular Graphics*, 14:33–38, 1996.

[116] A. M Howatson, P. G. (Peter Gradwell) Lund, and J. D. (Joseph Derwent) Todd. *Engineering tables and data*. London ; New York : Chapman and Hall, 2nd ed edition, 1991. Includes index.

[117] Takumi Hawa, Brian Henz, and Michael Zachariah. Computer simulation of nanoparticle aggregate fracture. *MRS Online Proceedings Library Archive*, 1056, 2007.

[118] Bharat Bhushan. *Nanotribology and nanomechanics: an introduction*. Springer, 2017.

[119] Agúndez, M., Cernicharo, J., and Goicoechea, J. R. Formation of simple organic molecules in inner t tauri disks. *A&A*, 483(3):831–837, 2008.

[120] Md Mahbubul Islam, Chenyu Zou, Adri C. T. van Duin, and Sumathy Raman. Interactions of hydrogen with the iron and iron carbide interfaces: a reaxff molecular dynamics study. *Phys. Chem. Chem. Phys.*, 18:761–771, 2016.

[121] Chenyu Zou, Adri C. T. van Duin, and Dan C. Sorescu. Theoretical investigation of hydrogen adsorption and dissociation on iron and iron carbide surfaces using the reaxff reactive force field method. *Topics in Catalysis*, 55(5):391–401, Jun 2012.

[122] S. A. Pandit A. Y. Grama H. M. Aktulga, J. C. Fogarty. Parallel reactive molecular dynamics: Numerical methods and algorithmic techniques. *Parallel Computing*, 38:245–259, 2012.

[123] Judith A Harrison and Donald W Brenner. Simulated tribochemistry: An atomic-scale view of the wear of diamond. *Journal of the American Chemical Society;(United States)*, 116(23), 1994.

[124] RALPH T. YANG and CHOR WONG. The role of surface diffusion in the langmuir-hinshelwood mechanism. *Chemical Engineering Communications*, 11(4-5):317–325, 1981.

[125] Maureen L Nietiadi, Emmanuel N Millán, Eduardo M Bringa, and Herbert M Urbassek. Bouncing window for colliding nanoparticles: Role of dislocation generation. *Physical Review E*, 99(3):032904, 2019.

[126] Ian M. Hutchings. Leonardo da vincis studies of friction. *Wear*, 360-361:51 – 66, 2016.

[127] Jianping Gao, W. D. Luedtke, D. Gourdon, M. Ruths, J. N. Israelachvili, and Uzi Landman. Frictional forces and amontons' law: from the molecular to the macroscopic scale. *The Journal of Physical Chemistry B*, 108(11):3410–3425, 2004.

[128] David Tabor. *Friction as a Dissipative Process*. Springer Netherlands, Dordrecht, 1992.

[129] G.A. Tomlinson B.Sc. Cvi. a molecular theory of friction. *The London, Edinburgh, and Dublin Philosophical Magazine and Journal of Science*, 7(46):905–939, 1929.

[130] V.L. Popov and J.A.T. Gray. Prandtl-tomlinson model: History and applications in friction, plasticity, and nanotechnologies. *ZAMM - Journal of Applied Mathematics and Mechanics / Zeitschrift für Angewandte Mathematik und Mechanik*, 92(9):683–708, 2012.

[131] O.M. Braun and A.G. Naumovets. Nanotribology: Microscopic mechanisms of friction. *Surface Science Reports*, 60(6):79 – 158, 2006.